7-30-2012 12:00 AM

Augmented Image-Guidance for Transcatheter Aortic Valve Implantation

Pencilla Lang
The University of Western Ontario

Supervisor
Dr. Terry Peters
The University of Western Ontario

Graduate Program in Biomedical Engineering
A thesis submitted in partial fulfillment of the requirements for the degree in Doctor of Philosophy

AUGMENTED IMAGE-GUIDANCE FOR TRANSCATHETER AORTIC VALVE IMPLANTATION

(Spine title: Augmented Image-Guidance for TAVI)

(Thesis format: Integrated Article)

by

Pencilla Lang

Faculty of Engineering
Department of Biomedical Engineering

Submitted in partial fulfillment
of the requirements for the degree of
Doctor of Philosophy

School of Graduate and Postdoctoral Studies
The University of Western Ontario
London, Ontario, Canada

July 2012

THE UNIVERSITY OF WESTERN ONTARIO
School of Graduate and Postdoctoral Studies

CERTIFICATE OF EXAMINATION

Chief Advisor	**Examining Board**
Dr. Terry Peters	Dr. Maria Drangova
	Dr. Aaron Ward
	Dr. Allan Skanes
	Dr. Graham Wright

The thesis by

Pencilla Lang

entitled

AUGMENTED IMAGE-GUIDANCE FOR TRANSCATHETER AORTIC VALVE IMPLANTATION

(Spine title: Augmented Image-Guidance for TAVI)

(Thesis format: Integrated Article)

is accepted in partial fulfillment of the
requirements for the degree of
Doctor of Philosophy

Date _____ _____

Chair of Examining Board

Abstract

The introduction of transcatheter aortic valve implantation (TAVI), an innovative stent-based technique for delivery of a bioprosthetic valve, has resulted in a paradigm shift in treatment options for elderly patients with aortic stenosis. While there have been major advancements in valve design and access routes, TAVI still relies largely on single-plane fluoroscopy for intraoperative navigation and guidance, which provides only gross imaging of anatomical structures. Inadequate imaging leading to suboptimal valve positioning contributes to many of the early complications experienced by TAVI patients, including valve embolism, coronary ostia obstruction, paravalvular leak, heart block, and secondary nephrotoxicity from contrast use.

A potential method of providing improved image-guidance for TAVI is to combine the information derived from intra-operative fluoroscopy and TEE with pre-operative CT data. This would allow the 3D anatomy of the aortic root to be visualized along with real-time information about valve and prosthesis motion. The combined information can be visualized as a 'merged' image where the different imaging modalities are overlaid upon each other, or as an 'augmented' image, where the location of key target features identified on one image are displayed on a different imaging modality.

This research develops image registration techniques to bring fluoroscopy, TEE, and CT models into a common coordinate frame with an image processing workflow that is compatible with the TAVI procedure. The techniques are designed to be fast enough to allow for real-time image fusion and visualization during the procedure, with an intra-procedural set-up requiring only a few minutes. TEE to fluoroscopy registration was achieved using a single-perspective TEE probe pose estimation technique. The alignment of CT and TEE images was achieved using custom-designed algorithms to extract aortic root contours from XPlane TEE images, and matching the shape of these contours to a CT-derived surface model. Registration accuracy was assessed on porcine and human images by identifying targets (such as guidewires or coronary ostia) on the different imaging modalities and measuring the correspondence

of these targets after registration.

The merged images demonstrated good visual alignment of aortic root structures, and quantitative assessment measured an accuracy of less than 1.5mm error for TEE-fluoroscopy registration and less than 6mm error for CT-TEE registration. These results suggest that the image processing techniques presented have potential for development into a clinical tool to guide TAVI. Such a tool could potentially reduce TAVI complications, reducing morbidity and mortality and allowing for a safer procedure.

Keywords: image-guided cardiac surgery; transcatheter aortic valve implantation; aortic valve; minimally invasive surgery; multimodality image fusion; registration; segmentation; medical imaging

Co-Authorship

Chapter 1 and Chapter 2 are extended and modified from the editorial:

- Lang P, Peters TM, Kiaii B, Chu MWA. The critical role of imaging navigation and guidance in transcatheter aortic valve implantation. J Thorac Cardiovasc Surg. 2012;143(6):1241-3.

All authors participated in manuscript preparation.

Chapter 3 and Chapter 4 are extended and modified from the papers:

- Lang P, Seslija P, Chu MWA, Bainbridge D, Guiraudon GM, Jones DL, et al. US - Fluoroscopy registration for transcatheter aortic valve implantation. Biomedical Engineering, IEEE Transactions on. 2012;59(5):1444-53.
- Lang P, Seslija P, Habets DF, Chu MWA, Holdsworth DW, Peters TM. Three-Dimensional Ultrasound Probe Pose Estimation from Single-Perspective X-rays for Image-Guided Interventions. In: Medical Imaging and Augmented Reality. vol. 6326; 2010. p. 344 - 352.
- Lang P, Seslija P, Bainbridge D, Guiraudon GM, Jones DL, Chu MW, et al. Accuracy assessment of fluoroscopy-transesophageal echocardiography registration. vol. 7964. SPIE; 2011. p. 79641Y.
- Lang P, Peters TM, Bainbridge D, Chu M. Real-Time Echocardiographic Augmented Fluoroscopic Imaging To Improve Transcatheter Aortic Valve Implantation Accuracy. In preparation for submission.

Petar Seslija and Damiaan Habets both assisted with software implementation. Petar Seslija, Gerard Guiraudon, Daniel Bainbridge and Douglas Jones assisted with the experimental process and data acquisition, and provided valuable guidance throughout. I was responsible for the remainder of the experimental design, registration code, image acquisition and processing, and manuscript preparation, all of which was supervised by Michael Chu and Terry Peters.

Chapter 5 is extended and modified from the following papers:

- Lang P, Chu MW, Bainbridge D, Guiraudon G, Jones DL, Peters TM. Surface-based CT-TEE Registration of the Aortic Root. Submitted.
- Lang P, Chu MW, Bainbridge D, Chen ECS, Peters, TM. CT - US Registration for Guidance of Transcatheter Aortic Valve Implantation. AE-CAI 2011, Augmented Environments for Computer Assisted Interventions, LNCS 7264, *in press*.
- Lang P, Chen ECS, Guiraudon GM, Jones DL, Bainbridge D, Chu MW, et al. Feature-based US to CT registration of the aortic root. In Wong KH and Holmes DR III, editors, Medical Imaging 2011: Visualization, Image-Guided Procedures and Modeling, vol. 7964 of SPIE 2011, p. 79641G. Lake Buena Vista, FL, USA, 2011.

Elvis Chen, Gerard Guiraudon, Daniel Bainbridge, Michael Chu and Douglas Jones assisted with the experimental process and data acquisition, and provided valuable guidance throughout. I was responsible for the remainder of the system and experimental design, registration code, image acquisition and processing, and manuscript preparation, all of which was supervised by Terry Peters.

Chapter 6 is extended and modified from the following papers:

- Lang P, Rajchl M, McLeod AJ, Chu MW, Peters TM. Feature identification for image-guided transcatheter aortic valve implantation. vol. 8316. SPIE; 2012. p. 83162X.
- Lang P, Rajchl M, McCleod AJ, Chu MWA, Peters TM. Automatic Contour Selection for CT-TEE Registration. In preparation for submission.

Martin Rajchl and A. Jonathan McLeod provided valuable assistance with code design. Michael Chu provided assistance with data acquisition and valuable guidance

throughout. I was responsible for the remainder of the code implementation, system and experimental design, image acquisition and processing and manuscript preparation, all of which was supervised by Terry Peters.

Dedicated to my grandfather, who always believed in the value of education.

Acknowledgments

This work would not have been possible without the efforts of numerous people, and I am always amazed at how the contributions of so many people have helped to make this journey possible for me.

I would like to start by acknowledging my supervisor Dr. Terry Peters, who sparked my interest in image-guided interventions when I spent a summer in his lab as a high school student many, many years ago. Throughout the years he has provided me with countless opportunities to see and participate in new and interesting things, and has been a constant source of guidance and support. His lab is truly an amazing place to spend time in, with unparalleled access to resources, equipment and collaborations.

I would also like to thank my advisory committee. Dr. Michael Chu has been a fantastic mentor, welcoming me into his OR, teaching me with incredible patience, providing insight into clinical medicine and lots of encouragement. Dr. David Holdsworth and Dr. Jim Johnson provided valuable advice and guidance along the way.

Special recognition goes out to Dr. Guiraudon, Dr. Doug Jones, Dr. McCarty, Dr. Kiaii and Dr. Bainbridge for sharing their expertise, providing advice and assistance with experimental work. It has truly been a privilege to work with and learn from such a talented and creative team.

I am particularly indebted to Petar Seslija for his assistance with the TEE probe tracking studies. He spent many late nights at the lab and at University Hospital with me calibrating devices, collecting data and writing code.

The cardiac group in the lab - Martin Rajchl, Feng Li and Maria Currie - have been the source of many insightful discussions. I have been very lucky to have been part of such a tight-knit group. Thanks go to J. Baxter and Jonathan McLeod for their help with my code. For every idea I implemented, they came up with two ideas to make it run faster and more efficiently.

Chris Wedlake, John Moore and Dr. Elvis Chen have been instrumental in troubleshooting all my problems (of which there were many), and providing assistance in everything from machining prototypes to debugging code on the fly during an exper-

iment.

Kim Booth, Ana Pimental, Diana Timmermans and Vicki Vanstrien were invaluable in ensuring that my MD/PhD program ran smoothly and navigating the complicated paperwork of my unique situation.

To the Peters lab group and all the friends I have made at Robarts and UWO: thank you for making this experience such a memorable one. It has been a unique pleasure to spend my days around people who demonstrate such unbridled enthusiasm for science and engineering, and who are always willing to engage in both insightful and entertaining discussions.

Finally, I would like to thank my parents for their unwavering support. They have always believed in and supported me, and were there for all the stresses and joys of graduate student life.

This work was supported financially by the Canadian Institute of Health Research (CIHR), the Canadian Foundation for Innovation, the Ontario Research Fund and Western University.

Contents

List of Tables

List of Figures

List of Abbreviations

2D	Two-Dimensional
3D	Three-Dimensional
AR	Aortic Regurgitation
AS	Aortic Stenosis
CT	Computed Tomography
CTA	Computed Tomography Angiography
DLT	Direct Linear Transform
FOV	Field of View
ICP	Iterative Closest Point
LoG	Laplacian of a Gaussian
LVOT	Left Ventricular Outflow Tract
MRI	Magnetic Resonance Imaging
NCC	Non-Coronary Cusp
OR	Operating Room
TAVI	Transcatheter Aortic Valve Implantation
TEE	Transesophageal Echocardiography
TRE	Target Registration Error
TTE	Transthoracic Echocardiography
US	Ultrasound

Chapter 1

Introduction

Cardiac disease remains the largest cause of death worldwide, and aortic valve disease affects 3% of the general population, making it the most common acquired heart valve disease in developed countries [1]. An aging population and a lack of effective drug therapies are leading to a greater societal burden from this condition. In the US alone, more than 50 000 surgical aortic valve replacements are performed every year [2]. An increase in the number of high risk surgical patients with multiple co-morbidities and a reluctance of patients to undergo open heart surgery have been driving the development of transcatheter techniques. Trancatheter aortic valve implantation (TAVI) is a percutaneous technique that has seen substantial growth in the last decade [3]. However, a significant number of complications associated with TAVI procedures remain, many of which can be attributed to sub-optimal image-guidance of the procedure.

1.1 Aortic Valve Anatomy

The aortic valve lies between the left ventricle and the ascending aorta, ensuring the one way motion of blood from the heart to the systemic circulation. The aortic root is defined as the area extending from the basal attachment of the aortic valve leaflets within the ventricle to their attachments at the sinutubular junction, as shown in Fig 1.1 [4].

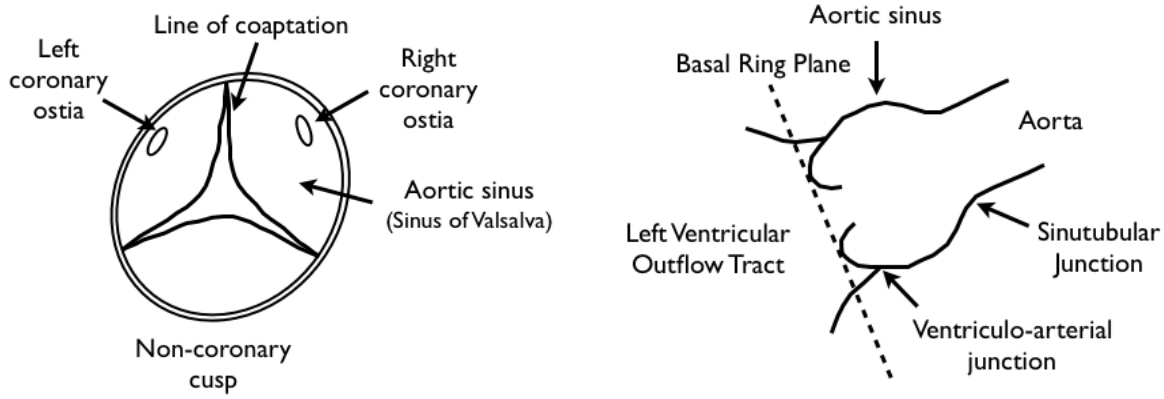

(a) (b)

Fig. 1.1: (a) Cross-sectional anatomy of the aortic valve. (b) Longitudinal anatomy of the aortic valve.

The aortic sinus (also known as the sinus of Valsalva) is an anatomic dilation of the ascending aortic which occurs just above the aortic valve. There are three aortic sinus cusps (Figure 1.1a):

- Left coronary cusp (where the left coronary artery leaves the aortic root at the left coronary ostia here)
- Right coronary cusp (where the right coronary artery leaves the aortic root at the right coronary ostia here)
- Non-coronary cusp

There are several important anatomical planes in the aortic root. The basal ring is formed by joining the basal attachment points of the leaflets within the left ventricular outflow tract, while the sinutubular junction is demarcated by a ridge and the top attachments of the aortic valve leaflets, and forms the outlet of the aortic root into the ascending aorta (Figure 1.1b).

1.2 Aortic Valve Disease and Treatment Options

Two diseases typically affect the aortic valve:

1. Aortic stenosis (AS): Abnormal narrowing of the valve, obstructing blood flow.
2. Aortic regurgitation (AR): Leaking of the aortic valve, allowing reverse flow.

1.2.1 Aortic Stenosis

The main cause of aortic stenosis is age-related degenerative calcification (more than 1/3 of cases). Calcium deposits causing thickening of the leaflets obstruct the valve from opening properly. Other common causes include a congenital bicuspid aortic valve (predisposing patients to the deposition of calcium on the valve leaflets) and rheumatic valve disease (causing fusion of the commissures between the leaflets with a small central orifice).

Aortic stenosis increases in incidence with age, and in individuals older than 75, the prevalence of moderate to severe aortic stenosis is between 3-9 %, making it the most common acquired heart valve disease in the western world [5].

The three classic symptoms associated with AS that typically occur with exertion include: heart failure, syncope or dizziness, and angina (chest pain).

Patients with aortic stenosis can remain asymptomatic for prolonged periods of time, however once symptoms develop, prompt surgical intervention is required, as mortality increases dramatically. Mean survival without valve replacement is two to three years, with a high risk of sudden death [2]. Currently, mechanical or bioprosthetic valve replacement is the only established treatment of symptomatic disease.

1.2.2 Aortic Regurgitation

Aortic regurgitation is caused by disease of the valve leaflets (usually rheumatic heart disease) or enlargement of the aortic root (aortic root dilation and congenital bicuspid valve). Symptoms include a sense of a pounding heart, chest pain, palpitations, and heart failure symptoms. Although AR is common, with an estimated prevalence of up to 30%, only 5-10% of patients with AR have severe disease, resulting in an overall prevalence of severe AR of less than 1% in the general population. Chronic AR follows a gradual course with a long asymptomatic period. Once there are symptoms, the patient may deteriorate quickly. Current guidelines recommend

surgical intervention before symptoms develop based on echocardiographic (cardiac ultrasound) parameters. Symptomatic patients undergo either valve replacement or repair.

1.3 Transcatheter Aortic Valve Implantation

Valve replacement or repair drastically improves the mortality of patients with symptomatic aortic stenosis or regurgitation. Despite these marked improvements, large numbers of patients are denied surgery due to the procedure being deemed too risky. These patients are managed conservatively with medical therapy, but have an extremely poor prognosis [6, 7]. Conventional surgery requires sternotomy, large incisions, and cardiopulmonary bypass, all of which can be traumatic to an elderly or frail patient with co-morbidities.

TAVI is a minimally invasive approach to deliver a bioprosthetic valve to the beating heart via a catheter. Xenogenic pericardial cusps are mounted within an expandable stent (Figure 1.2). Once deployed, this stent relies upon radial traction forces to seat the prosthesis within the native aortic annulus. This procedure was first reported in human patients by Walther et al in 2008 [8].

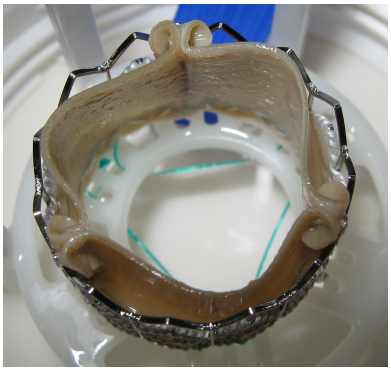

Fig. 1.2: Edwards SAPIEN Transcatheter aortic valve - xenogenic cusps mounted on an expandable stent.

Guidewires and sheaths are placed through a vascular access site to reach the level of the aortic valve. Balloon valvuloplasty is performed to relieve the stenosis of

the native aortic valve. The prosthesis is then guided up to the level of the aortic valve and implanted under rapid ventricular pacing (to temporarily decrease cardiac output) [9, 3]. Currently, the most common access sites are the femoral artery or the left ventricular apex (via a left anterolateral mini-thoracotomy) [3], although trans-subclavian, trans-axillary, and trans-aortic (ascending aorta) access points have also been demonstrated [10, 11, 12].

Since 2008, more than 20 000 TAVI procedures have been performed with good outcomes [13]. Recently, the randomized Placement of AoRTic TraNscathetER Valve (PARTNER) trial has demonstrated significantly better survival in TAVI treatment compared to medical therapy in non-surgical patients, and similar survival between TAVI and surgical replacement in high-risk patients [14, 15]. Use of the TAVI procedure is expected to increase rapidly in the next decade as cardiac centres worldwide become proficient in this technique.

Currently, there are two commercially available TAVI stent designs. The SAPIEN ^{TM}(Edwards Lifesciences, Irvine, CA, USA) valve has received FDA approval in the United States, and both the SAPIEN valve and the CoreValve ^{TM}(Medtronic Inc, Minneapolis, MN, USA) have recieved European conformity approval (CE mark). The SAPIEN valve is balloon-expanded, while the CoreValve uses a self-expanding nitinol design. Many 2nd, 3rd and 4th generation valves are currently under development and undergoing clinical trials, including the Symetis Acurate^{TM}valve (Symetis, Lausanne, Switzerland), the Medtronic Engager ^{TM}valve (Medtronic Inc., Minneapolis, MN, USA), the St. Jude PORTICO ^{TM}valve (St. Paul, MN, USA), the Sadra Lotus^{TM}valve (Sadra Medical Inc., Los Gatos, CA, USA) and the DirectFlow^{TM}valve (Direct Flow Medical, Inc, Santa Rosa, CA, USA).

1.4 Current TAVI Imaging Process

Imaging is used to plan the procedure pre-operatively, to guide positioning of the valve intra-operatively during deployment, and to assess results after the procedure. Several imaging modalities may be used including CT Angiography (CTA), fluoroscopy imaging (non-contrast fluoroscopy, coronary angiography, aortography), and

cardiac ultrasound imaging including both transesophageal echocardiography (TEE) and transthoracic echocardiography (TTE).

1.4.1 Pre-operative Imaging

Pre-operatively, images are used for several purposes [16, 17, 18], including:

1. Assessment of patient suitability for TAVI:
   (a) Assessment of aortic stenosis severity (in patients with low severity, medical management may be preferred) — *Doppler TEE*
   (b) Assessment of aortic valve anatomy and morphology (in most cases bicuspid valves are contraindicated) —*TEE*
   (c) Identification of quantity and location of aortic valve calcifications (these are related to the likelihood of para-valvular regurgitation after deployment of a TAVI valve)—*CT, TEE*
   (d) Spatial relationship with coronary ostia (low coronary ostia have a higher risk of being occluded) —*CT*
   (e) Assessment of left ventricle performance and hemodynamic stability (the presence of a thrombus in the ventricle, low ejection fraction and poor hemodynamic stability are contraindications to the procedure) —*TEE*
2. Procedure planning:
   (a) Selection of fluoroscopy planes and angles for use intra-operatively—*CT*
   (b) Selection of access points (peripheral artery and thoracic aorta anatomy, morphology, and calcification assessment)—*CT, coronary angiography, MRI*
   (c) Aortic valve size selection—*CT, TEE*

There is some discrepancy in the anatomical measurements that are taken from TEE and CT, and these differences can significantly affect outcome, particularly in aortic root sizing [19, 20].

1.4.2 Intra-operative Imaging

The majority of centres use a combination of fluoroscopy and TEE imaging intra-operatively. The stent can be visualized in both of these modalities. A study by Bagur *et al.* [21] demonstrated similar results when using fluoroscopy and echocardiography as the primary intra-operative image guidance modality for TAVI. However, the majority of centres primarily use fluoroscopy to guide stent positioning, as these images are more intuitive and require a smaller learning curve to interpret.

Intra-operatively, image guidance is required in the following tasks [18]:

1. Crossing of the aortic valve with a guidewire, and placement of the balloon at the aortic valve annulus.
2. Balloon aortic valvuloplasty under rapid ventricular pacing and visualization of valvuloplasty results.
3. Positioning and deployment of the transcatheter prosthesis:
    - Edwards Valve: Aortic rim of the prosthesis should be placed close to the tips of the native aortic valve, and the ventricular rim needs to be positioned 5mm below the aortic valvular annular plane.
    - CoreValve: The ventricular rim should be placed 5-10mm below the aortic valve annular plane.

1.4.2.1 Fluoroscopy imaging

Fluoroscopy imaging provides good visualization of the guidewires and positioning of the prosthesis, and remains the primary image guidance used in the majority of centres. The aortic valve plane and the coronary ostia can be identified using a contrast bolus. In addition, calcium deposits on the native aortic valve may serve as anatomical landmarks. An example fluoroscopy image is shown in Figure 1.3.

1.4.2.2 TEE Imaging

During TEE procedural guidance, a mixture of 2D and 3D images are used, and selection of the TEE view employed is operator dependent. Typical 2D views used

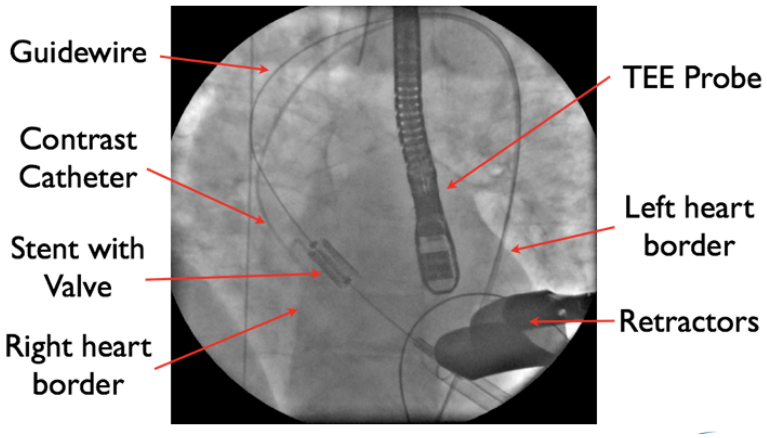

Fig. 1.3: Representative example of a fluoroscopy image used in TAVI.

during stent guidance include mid-esophageal aortic valve short axis (at the level of the leaflets) and long axis views, or both views visualized simultaneously using XPlane mode (the proprietary term used by Phillips to describe the simultaneous acquisition of a crossed pair of 2D images), as shown in Figure 1.4a [22, 23]. The long axis view is used to look for co-axial alignment of the left ventricular outflow tract (LVOT) and the prosthesis, and the short axis view to determine prosthesis centering. TEE is also used to monitor for potential antegrade or retrograde slippage of both the balloon and the prosthesis during inflation/expansion. The Live3D mode of the Philips iE33 scanner is used to visualize valve motion in real time, to assess anatomic results of balloon dilatation, to assess the geometry of the LVOT and to determine trajectory if having difficulties getting the catheters or wires in plane with a long axis 2D view [24]. Example TEE views in TAVI are shown in Figure 1.4b and c. 3D TEE images can also be acquired in 'full-volume' format, which consists of several gated volumes stitched together to produce an image with a larger FOV. Full-volume acquisitions typically are not used for intra-operative TAVI guidance due to the delay introduced by the stitching process.

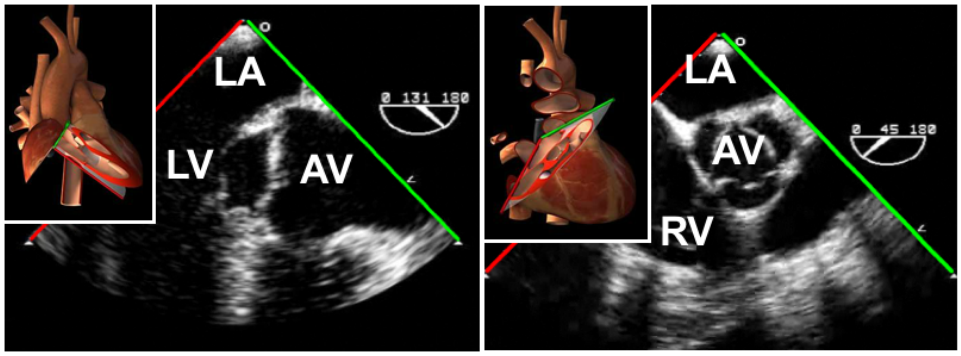

(a)

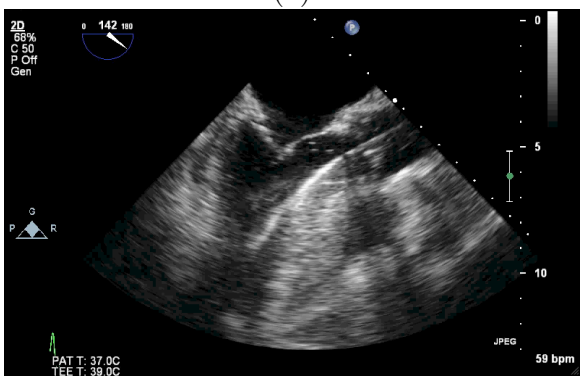

(b)

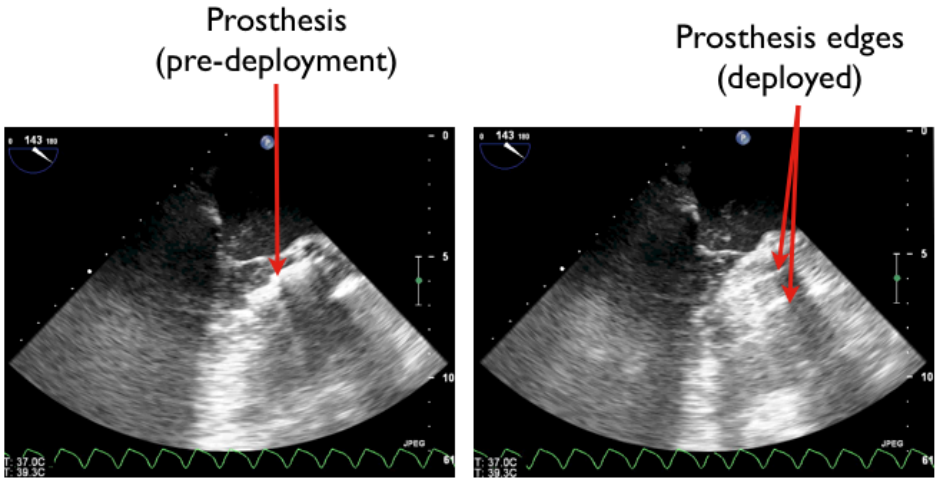

(c)

Fig. 1.4: (a) Representative mid-esophageal aortic valve views. The long axis view (left) and short axis view (right) are roughly orthogonal to each other, and allow visualization of the left atrium (LA), left ventricle (LV), right ventricle (RV) and aortic valve (AV). (b) Guidewire crossing the aortic root in a long axis TEE view. (c) TEE imaging of prosthesis deployment within the aortic root.

Baseline TEE is used to review anatomy of the aortic root, documenting the presence of mitral regurgitation (MR), wall motion abnormalities, baseline pericardial fluid (to detect procedure-induced cardiac tamponade), and left ventricular systolic function [25].

Intraoperatively, TEE is also used to assess early functioning of the bioprosthesis (confirming reduction in transaortic pressure gradients), identifying complications including perivalvular leak, hemodynamic instability, mitral valve dysfunction and vascular injury [22].

Calcification of the aortic valve may cause acoustic shadowing in the TEE images, limiting the utility of the 2D and 3D views. In these situations the calcium may serve as landmarks on fluoroscopic imaging. If there is limited aortic valve calcification, fluoroscopic imaging is sub-optimal and TEE images are more useful [25].

1.4.3 Post-operative Imaging

TEE is used to assess aortic prosthesis function immediately after deployment of the valve, and transthoracic echocardiography is used for long-term follow-up of prosthesis functioning. CT is often used to assess prosthesis positioning [16, 18].

1.5 TAVI Complications and Imaging Needs

Despite the success and growth of TAVI thus far, there remain significant complications including death, stroke, valve malposition, embolism, coronary obstruction, heart block requiring permanent pacemaker, paravalvular leak and secondary nephrotoxicity from contrast use [26]. The PARTNER Trials demonstrated a 30 day mortality of 3.4% - 5% for TAVI patients [15, 14]. The majority of these complications may be related to inadequate image guidance and suboptimal valve positioning, as single plane fluoroscopy provides only gross imaging of the aortic valve rendering the surgeon is blind to surrounding structures. Poor alignment of the valve with respect to the aortic annulus may result in valve malposition once deployed, or embolism of the device. Similarly, positioning the valve too deeply may cause atrio-ventricular block

and the need for a permanent pacemaker. Coronary obstruction may be caused by positioning the valve directly in front of the coronary ostia, or in such a manner that the displaced native valve occludes the coronary ostia. Some cases of paravalvular leak may also be related to poor positioning of the stent with respect to calcium on the native leaflets, which prevents the stent from deploying fully [27]. Finally, use of multiple contrast fluoroscopy images can increase the risk of secondary nephrotoxicity [28, 29].

The TAVI procedure would benefit from an image guidance platform that allows simultaneous visualization of the 3D anatomy of the aortic root and real time motion of the valve leaflets and the stent prosthesis. Such a platform would allow the physician to intuitively understand the spatial location of important anatomical structures for each specific patient and position the prosthesis accordingly. As outlined below, several image-guidance platforms have developed concurrently with this thesis.

1.5.1 DynaCT

Kempfert *et al.* [30] used the Dyna-CT system, an intra-operative cone-beam CT overlaid onto a fluoroscopy image, to provide anatomical context. The DynaCT system constructs a segmented aortic root from rotational angiography, and automatically detects landmarks, such as the coronary ostia. The segmented image is superimposed onto the real-time fluoroscopy image, to be employed as a guidance tool during transapical aortic valve implantation, and to select an optimal C-arm angulation for fluoroscopy. Recent results from Kempfert *et al.* in 50 patients demonstrate a positional accuracy of the coronary ostia, as displayed on the flouorscopy image, of 4.8mm [31]. Although this technique represents an improvement, the CT model remains static and does not allow for real-time intraoperative guidance.

1.5.2 Intraoperative MRI

Horvath *et al.* and Kahlert *et al.* have utilized intra-operative magnetic resonance imaging (MRI) to guide placement of the stent, resulting in successful implantation in porcine subjects [32, 33]. However, such intra-operative 3D imaging is not widely

available, and is very expensive. The base costs of intraoperative MRI can exceed $5.3 million with significant additional operating and maintenance costs [34]. In addition, many TAVI valves and surgical tools required for the procedure are not MRI compatible, and this form of imaging may limit the device options available [35].

1.5.3 TEE-Fluoroscopy Overlay

Gao *et al* [36] use 2D-3D image registration to determine pose of the TEE probe in 3D space. During the registration process, the algorithm compares projections through the 3D model (called *digitally reconstructed radiographs (DRRs)*) with multiple X-ray images. At each iteration an image comparison metric is used to calculate the similarity between the X-rays and the DRRs, and the algorithm continues until the similarity metric is maximized. Once the pose of the TEE probe in 3D space is known, the TEE image can be re-projected onto the fluoroscopy image. The use of biplane and single plane images for tracking is compared, and demonstrate significantly reduced accuracy with single plane tracking. This registration method uses the intrinsic geometry of the TEE probe, and does not require additional specialized equipment to provide tracking. However, accuracy remains limited, with TEE probe registration errors of up to 4mm, and a less than 80% success rate (defined as a registration error of less than 2.5mm) for monoplane tracking at a depth of 5cm. Furthermore, 2D-to-3D registration required approximately 5s to determine pose, which precludes real-time implementation.

1.6 Thesis Objectives

The objective of this work is to design an augmented image guidance system for intra-operative positioning of a TAVI valve. The image guidance system should:

1. Assist physicians in positioning the bioprosthetic valve across the native valve and aortic annulus more accurately by providing real-time visualization of aortic root anatomy concurrently with the stented valve.

2. Be easily accessible to the majority of centres where TAVI procedures are performed:
    - Low cost to implement and maintain
    - Integratable into existing operating rooms without significant modifications to the environment.
3. Be easily integrated into the existing clinical workflow of the procedure, and minimize the time required to complete the entire procedure.

1.7 Thesis Outline

The design objectives for an intra-operative TAVI image guidance system are accomplished by developing an automated method to register existing clinical images (CT, TEE and fluoroscopy) into a common coordinate frame. The registered images allow concurrent visualization of aortic root geometry and real-time motion of the valved stent. Chapter 2 introduces the overall system design and components, and describes the rationale behind the registration methodology. Chapters 3 and 4 describe the development and evaluation of a method to register intra-operative TEE and single-plane fluoroscopy images. Chapters 5 and 6 describe the development and evaluation of a method to register a pre-operative CT-derived model of the aortic root to intra-operative TEE images.

1.7.1 Overall System Framework

Chapter 2 introduces the vision for a clinical end product TAVI guidance system, and the resulting engineering design constraints, and describes the rationale for selecting the image registration approaches used in the system. A single-perspective TEE probe pose estimation technique is used to register the intra-operative TEE and fluoroscopy images, and a CT derived model is registered to the intra-operative TEE images using iterative closest point (ICP) registration. The TEE image acts as an intermediate image allowing all three images to be brought into a common coordinate system.

1.7.2 Single-perspective TEE Probe Pose Estimation

Chapter 3 introduces the idea of using the single-perspective clinical fluoroscopy images to perform pose estimation and tracking of the TEE probe intra-operatively. The localization precision and relative tracking accuracy of fidicual based and image intensity based pose estimation techniques are explored, and the feasibility of using each of these methods in our TAVI guidance system is evaluated.

1.7.3 TEE - Fluoroscopy Registration

Chapter 4 introduces the algorithms used to register intra-operative TEE and fluoroscopy images. The fidicual based TEE pose estimation technique selected in Chapter 3 is used to determine the location of the TEE probe in 3D space. This tracking is combined with an US calibration method (provides the location of image points with respect to the physical TEE probe head) to determine the location of image points in 3D space. Methods for automatic algorithm initialization and tracking failure recovery are described. Registration performance (accuracy and robustness) is evaluated on phantom, *ex vivo* porcine, and *in vivo* porcine images.

1.7.4 CT - TEE Registration

Chapter 5 describes an automatically initialized iterative closest point (ICP) algorithm registering pre-operative CT to intra-operative TEE images. Registration accuracy is evaluated on *ex vivo* porcine images, and clinical patient data. The left and right coronary ostia are used as targets, and the registration accuracy achieved using different TEE surface extraction methods are compared.

1.7.5 Automated TEE Contour Selection

A real-time ICP registration requires a real-time selection of points or features that are used in the registration. Chapter 6 describes algorithms to select TEE surface contours from the short-axis and long-axis mid-esophageal aortic root views.

The performance of these algorithms is evaluated on clinical images, and the registration error achieved using automatically-selected and manually-selected contours are compared.

1.7.6 Conclusions and Future Work

Chapter 7 provides a discussion of visualization options and difficulties for an augmented image-guidance environment based upon the system proposed in this thesis. Image processing and clinical workflows incorporating the use of the augmented image data are presented. Finally, future steps towards implementation of a prototype suitable for use in clinical trials are outlined.

References

[1] Singh IM, Shishehbor MH, Christofferson RD, Tuzcu EM, Kapadia SR. Percutaneous treatment of aortic valve stenosis. Cleveland Clinic Journal of Medicine. 2008;75(11):805–812.

[2] Bonow RO, Carabello BA, Catterjee K, et al. Focused update incorporated into the ACC/AHA 2006 guidelines for the management of patients with valvular heart disease: a report of the American College of Cardiology/American Heart Association Task force on Practice Guidelines (writing Committee to Revise the 1998 Guidelines for the Management of Patients with Valvular Heart Disease): endorsed by the Society of Cardiovasular Anesthesiologists, Society for Cardiovasular Angiography and Interventions, and Society of Thoracic Surgeons. Circulation. 2008;118:e523.

[3] Chu MWA, Borger MA, Mohr FW, Walther T. Transcatheter heart-valve replacement: Update. CMAJ. 2010;182(8):791–795.

[4] Piazza N, de Jaegere P, Schultz C, Becker AE, Serruys PW, Anderson RH. Anatomy of the aortic valvar complex and its implications for transcatheter implantation of the aortic valve. Circulation Cardiovascular interventions. 2008;1(1):74–81.

[5] Lindroos M, Kupari M, Heikkila J, Tilvis R. Prevalence of aortic valve abnormalities in the elderly: An echocardiographic study of a random population sample. Journal of the American College of Cardiology. 1993;21(5):1220–1225.

[6] Iung B, Baron G, Butchartc EG, Delahayed F, Gohlke-Barwolfe C, Levangf OW, et al. A prospective survey of patients with valvular heart disease in Europe: The Euro Heart Survey on valvular heart disease. European Heart Journal. 2003;24(13):1231–1243.

[7] Varadarajan P, Kapoor N, Bansal RC, Pai RG. Clinical Profile and Natural

History of 453 Nonsurgically Managed Patients With Severe Aortic Stenosis. Annals of Thoracic Surgery. 2006;82(6):2111–2115.

[8] Walther T, Falk V, Kempfert J, Borger MA, Fassl J, Chu MWA, et al. Transapical minimally invasive aortic valve implantation; the initial 50 patients. European Journal of Cardio-thoracic Surgery. 2008;33(6):983–988.

[9] Walther T, Dewey T, Borger MA, Kempfert J, Linke A, Becht R, et al. Transapical aortic valve implantation: step by step. Ann Thorac Surg. 2009;87(1):276–83.

[10] Modine T, Obadia JF, Choukroun E, Rioufoul G, Sudre A, Laborde JC, et al. Transcutaneous aortic valve implantation using the axillary/subclavian access: Feasibility and early clinical outcomes. Journal of Thoracic and Cardiovascular Surgery. 2011;141(2):487–491.

[11] Gerckens U, Latsios G, Grube E. Transcatheter aortic valve implantation: Clinical experience with the self-expanding medtronic corevalve prosthesis implantation through a trans-subclavian approach. Vascular Disease Management. 2010;7(1):E10–E14.

[12] Latsios G, Gerckens U, Grube E. Transaortic transcatheter aortic valve implantation: A novel approach for the truly "no-access option" patients. Catheterization and Cardiovascular Interventions. 2010;75(7):1129–1136.

[13] Piazza N, van Mieghem N, Tzikas A, Lange R, de Jaegere P, Serruys PW. Interpreting the current data on transcatheter aortic valve implantation: a difficult task. European Heart Journal Supplements. 2010;12(Supplement E):E41–E45.

[14] Leon MB, Smith CR, Mac MJ, Miller C, Mose JW, Svensson LG, et al. Transcatheter versus surgical aortic-valve replacement in high-risk patients. New England Journal of Medicine. 2011;364(23):2187–1298.

[15] Smith CR, Leon MB, Mac MJ, Miller C, Mose JW, Svensson LG, et al. Transcatheter aortic-valve implantation for aortic stenosis in patients who cannot

undergo surgery. New England Journal of Medicine. 2010 Oct;363(17):1597–1607.

[16] Delgado V, Ng AC, Shanks M, Van Der Kley F, Schuijf JD, Van De Veire NR, et al. Transcatheter aortic valve implantation: Role of multimodality cardiac imaging. Expert Review of Cardiovascular Therapy. 2010;8(1):113–123.

[17] Gessat M, Fraunfelder T, Altwegg L, Grnenfelder J, Falk V. Transcatheter aortic valve implantation: Role of imaging. Aswan Heart Centre Science & Practice Series. 2011;3.

[18] de Veire NRLV. Imaging to guide transcatheter aortic valve implantations. Journal of Echocardiography. 2010;8:1–6.

[19] Messika-Zeitoun D, Serfaty JM, Brochet E, Ducrocq G, Lepage L, Detaint D, et al. Multimodal Assessment of the Aortic Annulus Diameter. Journal of the American College of Cardiology. 2010 January;55(3):186–184.

[20] Kurra V, R S, Kapadia, Tuzcu EM, Halliburton SS, Svensson L, et al. Pre-Procedural Imaging of Aortic Root Orientation and Dimensions: Comparison Between X-Ray Angiographic Planar Imaging and 3-Dimensional Multidetector Row Computed Tomography. JACC: Cardiovascular Interventions. 2010;3(1):105–113.

[21] Bagur R, Rodes-Cabau J, Doyle D, De Larochelliere R, Villeneuve J, Lemieux J, et al. Usefulness of TEE as the primary imaging technique to guide transcatheter transapical aortic valve implantation. JACC: Cardiovascular Imaging. 2011;4(2):115–124.

[22] Chin D. Echocardiography for transcatheter aortic valve implantations. European Journal of Echocardiography. 2009;10(1):i21–i29.

[23] Filgueiras-Rama D, Lopez T, Moreno-Gomez R, Calvo-Orbe L, Dobarro D, Moreno-Yanguela M, et al. 3D transesophageal echocardiographic guidance

and monitoring of percutaneous aortic valve replacement. Echocardiography. 2010;27(1):84–86.

[24] Goncalves A, Marcos-Alberca P, Zamorano JL. Echocardiography: guidance during valve implantation. EuroIntervention : journal of EuroPCR in collaboration with the Working Group on Interventional Cardiology of the European Society of Cardiology. 2010;6 Suppl G:G14–19.

[25] Jayasuriya C, Moss RR, Munt B. Transcatheter aortic valve implantation in aortic stenosis: The role of echocardiography. Journal of the American Society of Echocardiography. 2011;24(1):15–27.

[26] Masson JB, Kovac J, Schuler G, Ye J, Cheung A, Kapadia S, et al. Transcatheter Aortic Valve Implantation: Review of the Nature, Management, and Avoidance of Procedural Complications. JACC: Cardiovascular Interventions. 2009;2(9):811 – 820.

[27] Bombien R, Humme T, Schunke M, Lutter G. Percutaneous aortic valve replacement: computed tomography scan after valved stent implantation in human cadaver hearts. European Journal of Cardio-thoracic Surgery. 2009;36:592–594.

[28] Van Linden A, Kempfert J, Rastan AJ, Holzhey D, Blumenstein J, Schuler G, et al. Risk of acute kidney injury after minimally invasive transapical aortic valve implantation in 270 patients. European Journal of Cardio-thoracic Surgery. 2011;39(6):835–843.

[29] Strauch JT, Scherner MP, Haldenwang PL, Pfister R, Kuhn EW, Madershahian N, et al. Minimally Invasive Transapical Aortic Valve Implantation and the Risk of Acute Kidney Injury. The Annals of Thoracic Surgery. 2010;89:465 – 470.

[30] Kempfert J, Falk V, Schuler G, Linke A, Merk D, Mohr FW, et al. Dyna-CT During Minimally Invasive Off-Pump Transapical Aortic Valve Implantation. The Annals of Thoracic Surgery. 2009;88(6):2041.

[31] Kempfert J, Rastan AJ, Noettling A, Blumenstein J, Linke A, Schule FW r G Mohr, et al. Perioperative DynaCT for Improved Imaging During Transapical Aortic Valve Implantation [AHA Meeting Abstract]. Circulation. 2010 Nov;122(21S).

[32] Horvath KA, Mazilu D, Guttman M, Zetts A, Hunt T, Li M. Midterm results of transapical aortic valve replacement via real-time magnetic resonance imaging guidance. Journal of Thoracic and Cardiovascular Surgery. 2010;139(2):424–430.

[33] Kahlert P, Parohl N, Albert J, Schafer L, Reinhardt R, Kaiser GM, et al. Real-time magnetic resonance imaging-guided transarterial aortic valve implantation: In vivo evaluation in swine. Journal of the American College of Cardiology. 2012;59(2):192–193.

[34] Association AH. Adopting Technological Innovation in Hospitals: Who Pays and Who Benefits?; 2006.

[35] Kahlert P, Eggebrecht H, Plicht B, Kraff O, McDougall I, Decker B, et al. Towards real-time cardiovascular magnetic resonance-guided transarterial aortic valve implantation: In vitro evaluation and modification of existing devices. Journal of Cardiovascular Magnetic Resonance. 2010;12(1).

[36] Gao G, Penney G, Ma Y, Gogin N, Cathier P, Arujuna A, et al. Registration of 3D trans-esophageal echocardiography to X-ray fluoroscopy using image-based probe tracking. Medical Image Analysis. 2012;16(1):38–49.

Chapter 2

TAVI Image Guidance System Design

2.1 Design Objectives

Multiple design objectives and constraints were taken into consideration during the design of an image-guidance system for TAVI. The primary objective is to provide context by visualizing the spatial relationships between the prosthesis, tools and patient anatomy to assist the physician in positioning of the prosthesis during deployment. Visualization accuracy should be maximized, visualization should be provided in real-time, and should be robust to varying patient anatomy and pathology.

Important anatomical features include:

- right and left coronary ostia
- aortic valve commissures
- basal root plane
- aortic annulus
- calcium deposits

Accuracy Requirements

There have been no studies evaluating the required accuracy for a TAVI image-

guidance system. However, clinical experience suggests that an image-guidance system with a registration error of less than 1mm would be optimal. However, a registration error of less than 5 mm likely constitutes a clinically useful tool that has the potential to improve patient outcomes. Preliminary studies with the DynaCT system demonstrate a registration error of approximately 5mm [1], and this system is currently undergoing clinical trials.

Secondary objectives for the image-guidance system include the following:

1. To minimize additional costs
2. To minimize additional intra-operative time
3. To be independent of prosthesis design, allowing the same augmented visualization to be used with multiple device designs
4. To minimize fluoroscopy exposure to both the patient and the staff
5. To minimize operator learning curves:
    - The visualization system should make the TAVI procedure more intuitive for physicians to perform and allow them to achieve technical competency more quickly. Currently it is estimated that it takes up to thirty procedures for a physician to become competent at the TAVI procedure [2].
    - The visualization system itself should also be intuitive to understand, and should not require the physician to master a large learning curve before it can be used.

2.2 Selection of Imaging Modalities

The proposed TAVI image guidance system provides augmented imaging by overlaying the currently acquired CT, TEE and fluoroscopy images to provide 3D spatial context. The image guidance system relies on registration of the three modalities into a common coordinate system, allowing any pair of images, or all three images, to be fused. Each of the imaging modalities provide unique advantages: fluoroscopy provides the best visualization of the prosthesis, TEE provides real-time anatomical

visualization, and pre-operative CT provides 3D spatial information. In combination, these three modalities provide all of the information required for effective image-guidance. Since each of these modalities are used in the standard clinical workflow of TAVI patients, workflow disruption and additional imaging costs are minimized by eliminating the need for the introduction of additional imaging technology or imaging protocol changes.

A variety of CT imaging protocols are employed on TAVI patients, with the majority of these using contrast angiography. High resolution acquisitions with a FOV centered around the heart are preferable for image processing. However, pre-operative assessment of the patient may require imaging of the thorax or both the thorax and abdomen. Typically coarser slice thickness is used in these scans to minimize radiation exposure to the patient. In addition, a small percentage of patients may receive a cardiac MRI instead, due to their inability to tolerate contrast, or the presence of co-morbidities requiring MRI for assessment. It is important that the pre-operative model integrated into the image-guidance system can be constructed from any of these images, to reduce the need for additional imaging, which may increase patient radiation and/or contrast exposure and imaging costs. Furthermore, current research is leading to the development of 3D patient-specific models, which may be used for either diagnostic or interventional purposes [3]. These techniques may allow a 3D model of the patient's aortic root to be constructed from a statistical shape analysis performed with a sparse or low-resolution set of points acquired from TEE or CT. The image-guidance system should also allow for the development of such models to be easily incorporated.

Fluoroscopy currently remains the primary modality used to guide stent placement, due to its ability to provide excellent visualization of the prosthesis. However, there are significant concerns with the use of fluoroscopy, including both patient and staff exposure to radiation, and contrast exposure in patients with renal disease [4, 5]. Early studies are demonstrating greater radiation exposure in TAVI procedures compared to traditional percutaneous coronary interventions (PCI) [6, 7] which have already been shown to carry significant risks for physicians [8]. Attempts have been made to perform TAVI without fluoroscopy [9, 10], but the use of TEE alone remains

complicated by the presence of shadowing artifacts. Prosthesis modelling and tracking is a current area of research [11], and may provide the possibility of a 'virtual' stent tool that can be incorporated into the image-guidance system, reducing or removing the need for fluoroscopy altogether. Linte *et al.* [12] demonstrated the use of such virtual tools for epicardial and endocardial procedures. Although the development of such models is beyond the scope of this thesis, it is important for the image-guidance system be designed for future integration of such technology. In particular, it is important that the registration and visualization of other images (TEE and CT) are not dependent on the presence of a contrast fluoroscopy image.

2.3 Registration Methodology

2.3.1 Image Registration

Image registration is the process of determining the mathematical transformations required to align two or more images or models in different coordinate systems to a common frame of reference. These images may be acquired using the same modality at different points in time, or with different imaging modalities. The transformation determined can be constrained to be rigid, affine, or non-rigid. Registration algorithms can be split into two categories: feature-based methods and intensity-based methods.

Feature-based methods

Feature-based methods align extracted homologous points, contours or surfaces. Corresponding point sets may comprise of externally added fiducials, or natural anatomical landmarks. If the point correspondence is known, singular value decomposition (SVD) of a 3 by 3 covariance matrix is used to solve for the registration parameters. If, on the other hand, the correspondence is not known, an iterative algorithm may be used to determine an optimal fit of the two point sets, with the most commonly used of these algorithms being the iterative closest point (ICP) approach [13]. In cardiac imaging there are very few spatially accurate anatomical landmarks, and pathological

conditions frequently hide them [14]. While registration performed with a small number of landmarks is highly susceptible to errors introduced by the feature extraction process, these registration methods tend to be computationally inexpensive, making them particularly amenable to real-time applications. Linte *et al.* [15], Cho *et al.* [16] and Ma *et al.* [17] describe examples of feature and contour-based approaches, and are further described in Section 2.3.2.3.

Intensity-based methods

Intensity-based methods which employ optimization to maximize a similarity metric (usually a function of voxel intensity), consist of three main components: a similarity metric, a transformation model and an optimization method. The similarity metric describes how well two images match, and is typically chosen based on image properties. Commonly used metrics include sum of squared differences, normalized cross correlation, and mutual information. The transformation model specifies the type of spatial mapping used (rigid, affine, elastic etc) and an optimization method finds the optimal transformation parameters by maximizing the similarity metric. Commonly used optimization methods include the Nelder-Mead Downhill Simplex Method, Powell's Direction Set Method and gradient descent [14].

Since intensity-based methods are relatively computationally intensive, a recent focus has been on GPU implementation for faster performance [18, 19]. Intensity-based methods generally require an accurate initialization since the optimal transform may correspond to a local rather than global minimum in the similarity measure. Furthermore, the presence of tools in one image but not the other in an interventional setting may pose a challenge for these methods. Intensity-based methods assume a correlation between the intensity distribution of the two images, and they demonstrate fairly good success when registering CT and fluoroscopy images since these images are derived from the same physical process [20]. In comparison, the performance of intensity-based registration of ultrasound and CT images has been less successful since CT intensities depend upon X-ray attenuation while ultrasound intensities depend on acoustic impedance between tissue interfaces. Mutual information [21] is a commonly used image metric for registering images of different modalities, as

it aims to maximize overlap in the available image information without making any direct assumptions about the intensity relationships between the two images [22]. Methods to improve results have included performing the registration on 'simulated' ultrasound images generated from CT [23, 24] or image-derived probability maps of tissue type [25], and pre-processing images to highlight boundaries [26].

Both feature- and intensity-based methods have been used extensively in registering cardiac images. Choice of registration methodology depends on several factors:

- **Imaging modalities used**: Automated segmentation and feature extraction algorithms are easier to construct for high resolution CT and MRI images than for TEE.
- **Required accuracy for the clinical application**: Feature-based registration with a small number of landmarks or contours may demonstrate lower registration accuracy than the more computationally intensive intensity-based methods. However it has been demonstrated that many clinical tasks, such as tool navigation and port placement selection, may only require accuracies on the order of 5 - 10 millimetres [27]. Although no formal experimental studies have been conducted on the accuracy required for guidance of TAVI procedures, it is clinically estimated that an error of 1-2mm may be acceptable as this corresponds to approximately 10 - 20% of the gap between the basal plane and the coronary sinuses.
- **Required speed**: Despite large gains in speed with the introduction of GPU processing, intensity-based methods remain too slow for real-time update and display [22].
- **Rigidity assumption**: Currently the majority of cardiac image registration algorithms use a rigid-body assumption. This generally requires the use of cardiac gating to circumvent problems with cardiac deformation during systole and diastole. However, a rigid body assumption without cardiac gating is more appropriate for certain anatomical structures than others. While the left ventricular apex may deform significantly during systole, a highly calcified and

stenotic aortic root may experience minimal deformation [28].

2.3.2 Prior work on cardiac image registration

Many previous attempts have been made to register multi-modality cardiac images using a wide range of registration techniques [14, 29]. In this section a brief review of image registration of cardiac CT, TEE and fluoroscopy images is provided, with a focus on the applicability of these approaches to real-time guidance of TAVI.

2.3.2.1 CT-Fluoroscopy Registration

The majority of algorithms registering CT-derived models to fluoroscopy images have been developed to guide catheter-based electrophysiology ablation procedures. Registration of cardiac models to non-contrast fluoroscopy images is particularly challenging due to the poor contrast of soft tissue structures in x-ray. Methods that have been explored include simple manual registration [30, 31, 32], external surface markers on the skin of the patient [33], landmark registration using tracked catheters inside the superior vena cava, pulmonary veins and coronary sinuses [31, 34], the spine [31] and artery or vein bifurcations [32]. More recently, methods that rely on intra-operative CT systems that are intrinsically registered to fluoroscopy have been used to register pre-operative models to fluoroscopy by first registering to the intra-operative 3D images [35, 36]. These techniques are not suitable for the development of a TAVI guidance system, as they do not account for respiratory or cardiac motion, and require significant user interaction to perform the registration.

Liao *et al.* [37] and Liu *et. al* [38] propose a 3D-2D registration approach to registering a CT model of the aortic root to contrast-enhanced fluoroscopy images. They present an algorithm for automatic contrast detection and aortic root extraction from the fluoroscopy images, but have not yet implemented and evaluated a registration process using these images. In this approach, aortic root extraction relies heavily on the presence of contrast in the aortic root, which may increase the risk of acute kidney injury and allows only for intermittent updates to the registration during the procedure.

2.3.2.2 TEE-Fluoroscopy Registration

Jain *et al.* [39] previously used magnetic tracking of the TEE probe to register static TEE and fluoroscopy images of a needle tip with a mean accuracy of 2.04 ± 0.59mm. The magnetic tracking system consists of a field generator, a central control unit and field sensors (solenoids). The field generator produces a controlled pulsed magnetic field, and the field sensors react to produce a signal that is dependent on their position and orientation within the field. While this technology has shown promise in the creation of virtual and augmented environments to guide minimally invasive cardiac interventions [40], several limitations to this technology remain, complicating it's use in a TAVI procedure:

1. Limited field of view (FOV) - the tracked tool must be within the FOV of the magnetic field generator. Outside this FOV tracking accuracy degrades rapidly [41].
2. A magnetic field sensor must be attached to the tracked TEE probe, either externally or internally embedded within the plastic TEE probe casing. The close proximity of metallic objects within the TEE probe may reduce tracking accuracy [42].
3. The field generator must be placed sufficiently close to the thoracic cavity of the patient to allow the tools to remain within the FOV within all times. Placement at the head or side of the OR table can be inconvenient and interfere with OR workflow. Recent advances in magnetic field generator design by NDI (Waterloo, Canada) have allowed the field generator to be placed under the OR table. Furthermore, a 'window' design allows these field generators to be used with C-arm fluoroscopy (a regular field generator placed beneath the patient would obscure the fluoroscopy image). However, the size of the 'window' remains limited, particularly for fluoroscopy of the thoracic cavity, and the fluoroscopy image may remain occluded in heavy patients or at particular C-arm acquisition angles [43].
4. The presence of large amounts of metal in the C-arm reduces tracking accuracy [43].

Gao *et al.* present a method to track the 3D pose of the TEE probe and provide image fusion, as described in Section 1.5.3.

2.3.2.3 CT-TEE Registration

The literature reports several attempts to register 3D models derived from CT and/or MRI to various forms of cardiac ultrasound images, including 2D and 3D TEE images and intracardiac echocardiography (ICE), as described in the following sections.

Feature-based registration

Marquering *et al.* [44] use a anatomical landmark based registration with manual correction to register CT angiography images with ICE images, while Linte *et al.* [15] employed contour-based registration to align a pre-operative model derived from CT to intra-operative TEE images to guide the navigation of surgical tools. Cho *et al.* [16] used modified ICP registration with robust estimation to register CT to 2D TEE images using anatomical landmarks, and Duan *et al.* [45] also performed landmark-based registration to overlay segmented structures from 4D TEE onto CT images. The landmarks used in all studies were manually selected, and were a subset of the mitral annulus, atrial annulus, coronary ostia, and left ventricular apex. All three studies demonstrated a registration accuracy on the order of 3 - 5 mm. Landmark selection in cardiac images is particularly challenging due to the lack of definitive anatomical boundaries (for example the annuli consist of a histopathological transition not visible on imaging). Furthermore, large landmarks (such as the coronary ostia) are reduced to single points. A small FOV in the TEE images frequently allows only one or two of these landmarks to be visible in any given image acquisition. When TEE images of the aortic root are acquired, even fewer of these anatomical landmarks are visible.

Intensity-based registration

Intensity-based methods face the challenges posed by a low signal-to-noise ratio in ultrasound images, the presence of ultrasound imaging artefacts, and inherent differences in patterns of image intensity between CT and ultrasound due to the different physical processes used to create the images. One approach has been to pre-process one or both modalities to remove noise and make the nature of image features more

similar between the modalities [46, 23]. King *et. al* [47] extend this approach by incorporating *a priori* knowledge about tissue properties and the ultrasound beamforming process, while Sun *et al.* [48] and Wein *et al.* [24] have also used image-based registration to fuse CT images with ICE images. In these studies, mean registration errors ranged from 2-5mm, which is similar to those achieved using feature-based methods.

Computational speed is frequently a concern with intensity-based approaches intended for real-time applications. In practice this issue has been addressed through the use of GPU processing [24, 22]or by subsampling [18].

2.3.3 Proposed registration method

A two-step registration method is used:

1. TEE-Fluoroscopy registration
2. CT-TEE registration

This method uses the TEE image as an intermediate step to register all three images into a common coordinate frame (Figure 2.1).

Since both fluoroscopy and CT are registered to the same TEE image, the CT model is intrinsically registered to the fluoroscopy image. This method provides several advantages over registering each individual pair of images together independently. CT to fluoroscopy registration relies heavily on the presence of anatomical features in the fluoroscopy image. However, in cardiac fluoroscopy images, very few soft tissue structures are visible without the use of a contrast bolus, which this approach attempts to minimize for TAVI, to prevent acute kidney injury [49]. Relying on contrast-enhanced fluoroscopy images leads to limited and interrupted visualization of the registered images. TEE images can be acquired throughout the procedure, with no risk from ionizing radiation and no additional monetary or efficiency costs. Furthermore, with the addition of improved tool tracking and visualization, the use of fluoroscopy can be eliminated altogether, without affecting the registration of the remaining modalities. A potential limitation of this approach is the compounding

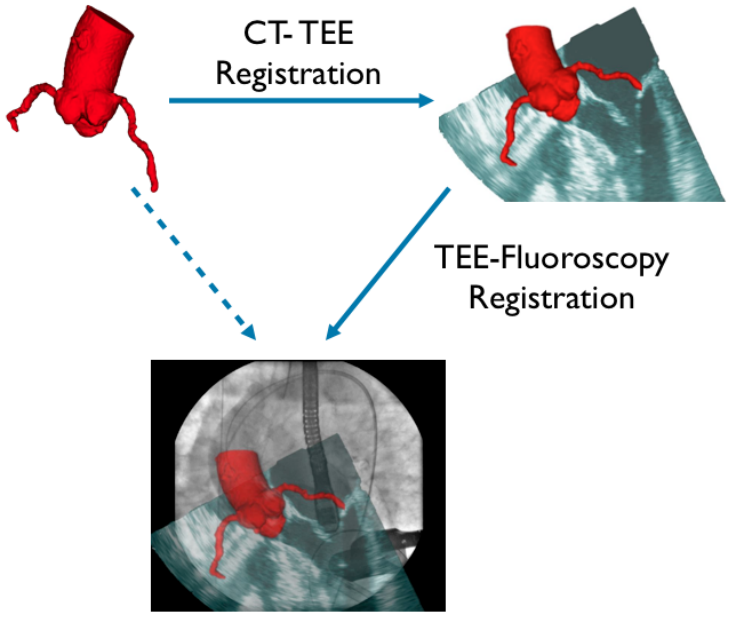

Fig. 2.1: Registration methodology with CT-fluoroscopy registration using the TEE image as an intermediate step.

of errors during registration of the CT and fluoroscopy image, since an intermediate step is used. Alternatively, bony structures of the thoracic cavity may be used to aid in direct CT-fluoroscopy registration, however these structures are not rigidly fixed with respect to the heart and do not reflect cardiac motion, limiting accuracy.

A 2D-to-3D TEE probe pose estimation technique is used to register the TEE and fluoroscopy images. The TEE probe is always visible in the fluoroscopy image, and large attenuation differences between the TEE probe and cardiac tissue allow for good feature extraction. The feasibility of both fiducial-based and image-based approaches are explored in Chapter 3, and the fiducial-based approach is selected for its accuracy, robustness and fast processing speed. A contour-based approach (further described in Chapters 6 and 5) is selected to register the TEE and CT images, using an ICP algorithm. This approach was selected for its fast processing speed (to allow real-time registration), and for its robustness to initialization position (allowing an easy automatic initialization algorithm to be used).

References

[1] Kempfert J, Rastan AJ, Noettling A, Blumenstein J, Linke A, Schule FW r G Mohr, et al. Perioperative DynaCT for Improved Imaging During Transapical Aortic Valve Implantation [AHA Meeting Abstract]. Circulation. 2010 Nov;122(21S).

[2] Alli OO, Booker JD, Lennon RJ, Greason KL, Rihal CS, Holmes Jr DR. Transcatheter aortic valve implantation: Assessing the learning curve. JACC: Cardiovascular Interventions. 2012;5(1):72–79.

[3] Ionasec RI, Voigt I, Georgescu B, Wang Y, Houle H, Vega-Higuera F, et al. Patient-specific modeling and quantification of the aortic and mitral valves from 4-D cardiac CT and TEE. IEEE Transactions on Medical Imaging. 2010;29(9):1636–1651.

[4] Van Linden A, Kempfert J, Rastan AJ, Holzhey D, Blumenstein J, Schuler G, et al. Risk of acute kidney injury after minimally invasive transapical aortic valve implantation in 270 patients. European Journal of Cardio-thoracic Surgery. 2011;39(6):835–843.

[5] Strauch JT, Scherner MP, Haldenwang PL, Pfister R, Kuhn EW, Madershahian N, et al. Minimally Invasive Transapical Aortic Valve Implantation and the Risk of Acute Kidney Injury. The Annals of Thoracic Surgery. 2010;89:465 – 470.

[6] Signorotto P, del Vecchio A, Montorfano M, Maisano F, Giagnorio M, Bellanca R, et al. Dosimetric data and radiation risk analysis for new procedures in interventional cardiology. Radiation Protection Dosimetry. 2010;142(2-4):201–208.

[7] Conradi L, Seiffert M, Franzen O, Baldus S, Schirmer J, Meinertz T, et al. First experience with transcatheter aortic valve implantation and concomitant percutaneous coronary intervention. Clinical Research in Cardiology. 2011;100(4):311–316.

[8] Kim KP, Miller DL. Minimising radiation exposure to physicians performing fluoroscopically guided cardiac catheterisation procedures: A review. Radiation Protection Dosimetry. 2009;133(4):227–233.

[9] Ferrari E, Sulzer C, Marcucci C, Rizzo E, Tozzi P, von Segesser LK. Transapical Aortic Valve Implantation Without Angiography: Proof of Concept. Annals of Thoracic Surgery. 2010;89(6):1925–1932.

[10] Bagur R, Rodes-Cabau J, Doyle D, De Larochelliere R, Villeneuve J, Lemieux J, et al. Usefulness of TEE as the primary imaging technique to guide transcatheter transapical aortic valve implantation. JACC: Cardiovascular Imaging. 2011;4(2):115–124.

[11] Schoenhagen P, Hill A, Kelley T, Popovic Z, Halliburton SS. In vivo imaging and computational analysis of the aortic root. Application in clinical research and design of transcatheter aortic valve systems. Journal of Cardiovascular Translational Research. 2011;4(4):459–469.

[12] Linte CA, Moore J, Wedlake C, Peters TM. Evaluation of model-enhanced ultrasound-assisted interventional guidance in a cardiac phantom. IEEE Transactions on Biomedical Engineering. 2010;57(9):2209–2218.

[13] Besl PJ, McKay ND. A Method for Registration of 3-D Shapes. IEEE Transactions on Pattern Analysis and Machine Intelligence. 1992;14(2):239–256.

[14] Makela T, Clarysse P, Sipila O, Pauna N, Pham QC, Katila T, et al. A review of cardiac image registration methods. IEEE Transactions on Medical Imaging. 2002;21(9):1011–1021.

[15] Linte CA, Moore J, Wedlake C, Bainbridge D, Guiraudon GM, Jones DL, et al. Inside the beating heart: An in vivo feasibility study on fusing pre- and intraoperative imaging for minimally invasive therapy. International Journal of Computer Assisted Radiology and Surgery. 2009;4(2):113–123.

[16] Cho DS, Linte C, Chen ECS, Bainbridge D, Wedlake C, Moore J, et al. Predicting target vessel location on robot-assisted coronary artery bypass graft using CT to ultrasound registration. Medical Physics. 2012;39(3):1579–1587.

[17] Ma YL, Penney GP, Rinaldi CA, Cooklin M, Razavi R, Rhode KS. Echocardiography to magnetic resonance image registration for use in image-guided cardiac catheterization procedures. Physics in Medicine and Biology. 2009;54(16):5039–5055.

[18] Huang X, Ren J, Guiraudon G, Boughner D, Peters TM. Rapid dynamic image registration of the beating heart for diagnosis and surgical navigation. IEEE Transactions on Medical Imaging. 2009;28(11):1802–1814.

[19] Li B, Young AA, Cowan BR. GPU accelerated non-rigid registration for the evaluation of cardiac function. Lecture Notes in Computer Science. 2008;5242 LNCS(PART 2):880–887.

[20] Markelj P, Tomazevic D, Likar B, Pernus F. A review of 3D/2D registration methods for image-guided interventions. Medical Image Analysis. 2012;p. 642–661.

[21] Pluim JPW, Maintz JBA, Viergever MA. Mutual-information-based registration of medical images: A survey. IEEE Transactions on Medical Imaging. 2003;22(8):986–1004.

[22] Li F, Lang P, Rajchl M, Chen ECS, Guiraudon G, Peters TM. Towards real-time 3D US-CT registration on the beating heart for guidance of minimally invasive cardiac interventions. vol. 8316. SPIE; 2012. p. 831615.

[23] Wein W, Brunke S, Khamene A, Callstrom MR, Navab N. Automatic CT-ultrasound registration for diagnostic imaging and image-guided intervention. Medical Image Analysis. 2008;12(5):577–585.

[24] Wein W, Camus E, John M, Diallo M, Duong C, Al-Ahmad A, et al. Towards guidance of electrophysiological procedures with real-time 3D intracar-

diac echocardiography fusion to C-arm CT. Lecture Notes in Computer Science. 2009;5761 LNCS(PART 1):9–16.

[25] Penney GP, Blackall JM, Hamady MS, Sabharwal T, Adam A, Hawkes DJ. Registration of freehand 3D ultrasound and magnetic resonance liver images. Medical Image Analysis. 2004;8(1):81–91.

[26] Leroy A, Mozer P, Payan Y, Troccaz J. Rigid registration of freehand 3D ultrasound and CT-scan kidney images. vol. 3216; 2004. p. 837–844.

[27] Linte C, Lang P, Rettmann M, Cho D, Holmes D, Robb R, et al. Accuracy considerations in image-guided cardiac interventions: experience and lessons learned. International Journal of Computer Assisted Radiology and Surgery. 2012;7:13–25.

[28] Cheng A, Dagum P, Miller DC. Aortic root dynamics and surgery: from craft to science. Philosophical Transactions of the Royal Society B: Biological Sciences. 2007;362(1484):1407–1419.

[29] van der Hoeven BL, Schalij MJ, Delgado V. Multimodality imaging in interventional cardiology. Nature Reviews Cardiology. 2012;.

[30] Auricchio A, Sorgente A, Soubelet E, Regoli F, Spinucci G, Vaillant R, et al. Accuracy and usefulness of fusion imaging between three-dimensional coronary sinus and coronary veins computed tomographic images with projection images obtained using fluoroscopy. Europace. 2009;11(11):1483–1490.

[31] Knecht S, Skali H, O'Neill MD, Wright M, Matsuo S, Chaudhry GM, et al. Computed tomography-fluoroscopy overlay evaluation during catheter ablation of left atrial arrhythmia. Europace. 2008;10(8):931–938.

[32] Ector J, De Buck S, Huybrechts W, Nuyens D, Dymarkowski S, Bogaert J, et al. Biplane three-dimensional augmented fluoroscopy as single navigation tool for ablation of atrial fibrillation: Accuracy and clinical value. Heart Rhythm. 2008;5(7):957–964.

[33] Rhode K, Ma Y, Chandrasena A, King A, Gao G, Chinchapatnam P, et al. Evaluation of the use of multimodality skin markers for the registration of pre-procedure cardiac MR images and intra-procedure x-ray fluoroscopy images for image guided cardiac electrophysiology procedures. vol. 6918. SPIE; 2008. p. 69181R.

[34] Sra J, Krum D, Malloy A, Vass M, Belanger B, Soubelet E, et al. Registration of three-dimensional left atrial computed tomographic images with projection images obtained using fluoroscopy. Circulation. 2005;112(24):3763–3768.

[35] Li JH, Haim M, Movassaghi B, Mendel JB, Chaudhry GM, Haffajee CI, et al. Segmentation and registration of three-dimensional rotational angiogram on live fluoroscopy to guide atrial fibrillation ablation: A new online imaging tool. Heart Rhythm. 2009;6(2):231–237.

[36] Krishnaswamy A, Tuzcu EM, Kapadia SR. Three-dimensional computed tomography in the cardiac catheterization laboratory. Catheterization and Cardiovascular Interventions. 2011;77(6):860–865.

[37] Liao R, You W, Yan M, John M. Automatic detection of contrast injection on fluoroscopy and angiography for image guided trans-catheter aortic valve implantations (TAVI). vol. 7964. SPIE; 2011. p. 79640Z.

[38] Liu Y, Liao R, Lv X. Extended contrast detection on fluoroscopy and angiography for image-guided trans-catheter aortic valve implantations (TAVI). vol. 8316. SPIE; 2012. p. 831618.

[39] Jain A, Gutierrez L, Stanton D. 3D TEE Registration with X-Ray Fluoroscopy for Interventional Cardiac Applications. In: FIMH. vol. 5528; 2009. p. 321–329.

[40] Linte CA, White J, Eagleson R, Guiraudon GM, Peters TM. Virtual and augmented medical imaging environments: Enabling technology for minimally invasive cardiac interventional guidance. IEEE Reviews in Biomedical Engineering. 2010;3:25–47.

[41] Hummel J, Figl M, Birkfellner W, Bax MR, Shahidi R, Maurer Jr CR, et al. Evaluation of a new electromagnetic tracking system using a standardized assessment protocol. Physics in Medicine and Biology. 2006;51(10):N205–N210.

[42] Moore JT, Wiles AD, Wedlake C, Bainbridge D, Kiaii B, Trejos AL, et al. Integration of trans-esophageal echocardiography with magnetic tracking technology for cardiac interventions. In: Medical Imaging 2010: Visualization, Image-Guided Procedures, and Modeling, Proceedings of the SPIE.. vol. 7625; 2010. p. 76252Y–76252Y–10.

[43] Bo LE, Leira HO, Tangen GA, Hofstad EF, Amundsen T, Lang T. Accuracy of electromagnetic tracking with a prototype field generator in an interventional or setting. Medical Physics. 2012;39(1):399–406.

[44] Marquering HA, Dijkstra J, Besnehard QJA, Duthe JPM, Schuijf JD, Bax JJ, et al. Coronary CT angiography - IVUS image fusion for quantitative plaque and stenosis analyses. vol. 6918; 2008. .

[45] Duan Q, Shechter G, Gutierrez LF, Stanton D, Zagorchev L, Laine AF, et al. Augmenting CT cardiac roadmaps with segmented streaming ultrasound. vol. 6509; 2007. .

[46] Zhang W, Noble JA, Brady JM. Spatio-temporal registration of real time 3D ultrasound to cardiovascular MR sequences. Lecture Notes in Computer Science. 2007;4791 LNCS(PART 1):343–350.

[47] King AP, Rhode KS, Ma Y, Yao C, Jansen C, Razavi R, et al. Registering preprocedure volumetric images with intraprocedure 3-D ultrasound using an ultrasound imaging model. IEEE Transactions on Medical Imaging. 2010;29(3):924–937.

[48] Sun Y, Kadoury S, Li Y, John M, Resnick J, Plambeck G, et al. Image guidance of intracardiac ultrasound with fusion of pre-operative images. Lecture Notes in Computer Science. 2007;4791 LNCS(PART 1):60–67.

[49] Masson JB, Kovac J, Schuler G, Ye J, Cheung A, Kapadia S, et al. Transcatheter Aortic Valve Implantation: Review of the Nature, Management, and Avoidance of Procedural Complications. JACC: Cardiovascular Interventions. 2009;2(9):811 – 820.

Chapter 3

Single Perspective Pose Estimation

In this chapter, 2D-3D registration of a 3D model to a fluoroscopy image is used for pose estimation of a TEE probe, as an alternative to the use of magnetic tracking techniques that require significant probe modification to incorporate sensors. The feasibility of TEE probe tracking based on two single-perspective pose estimation techniques (fiducial-based and image intensity-based pose estimation) is assessed using several studies:

1. The theoretical maximum tracking precision that can be achieved using intensity-based pose estimation is calculated using a simulation study.
2. The relative tracking accuracy of both the fiducial based and image intensity based pose estimation techniques is evaluated empirically.
3. The effect of the number of tracking fiducials on TEE probe localization precision using fiducial-based pose estimation is evaluated.

3.1 3D-to-2D Registration Pose Estimation

3.1.1 Fiducial-Based Pose Estimation

In fiducial-based pose estimation technique, external tracking fiducials are rigidly fixed to the TEE probe, with the 3D pose (i.e. position and orientation) of the tracking fiducials being determined using Projection-Procrustes registration [1]. Projection-

Procrustes registration uses Procrustes registration to solve projection equations derived from the perspective geometry of a single-plane radiography system [2], as shown in Figure 3.1.

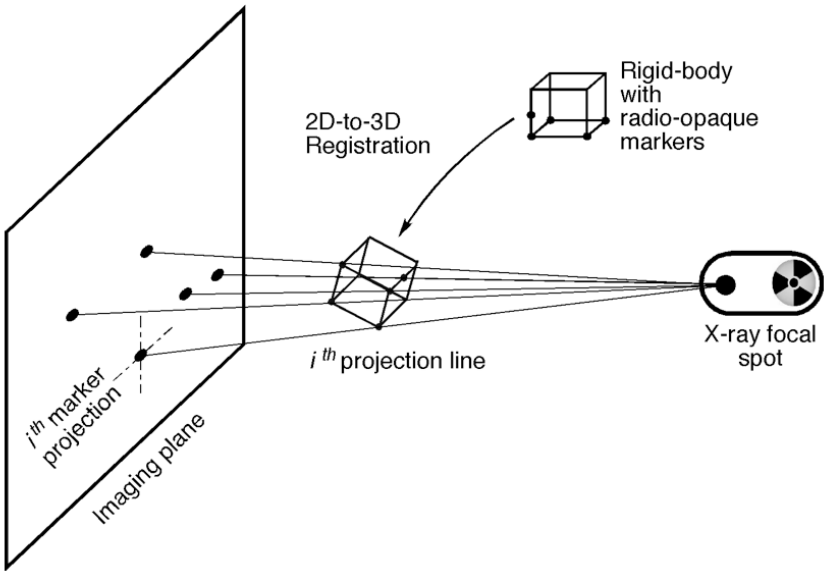

Fig. 3.1: Fiducial-based 3D-2D registration, where the pose of the rigid body is estimated by matching its theoretical projection to that measured by the radiograph.

The Projection-Procrustes registration process uses three coordinate system:

1. 2D coordinate system *(u,v)*, corresponding to the x-ray imaging plane,
2. 3D world coordinate system *(x,y,z)*,
3. 3D local object coordinate system *(x',y',z')*, corresponding to the TEE probe head. The spatial position of items within this local coordinate system is established using a microCT scan of the probe head and attached fiducials.

2D-to-3D registration is performed as follows:

1. The location of each tracking fiducial is determined within the local TEE probe coordinate system by thresholding and semi-automated point selection $P_i(x_i', y_i,' z_i')$, where i represents each tracking fiducial.
2. The image coordinates (u_i, v_i) of the fiducials appearing on the fluoroscopy image are determined.

3. An optimization is performed to determine the best fit world coordinates $P_i(x_i, y_i, z_i)$ for the given image coordinates.

In this study fiducial detection and correspondence on the fluoroscopy image was initialized manually using an interactive display. Initialization was only required for the first frame of an image sequence, and marker prediction based on linear extrapolation from previous frames was used to reduce the search space in following image frames.

Further details are provided in Appendix A.

3.1.2 Image Intensity-Based Pose Estimation

The intensity-based 2D-to-3D registration technique used in this study was implemented based on the algorithm initially described by Penney *et. al* [3, 4], and uses the same coordinate system as the fiducial-based tracking described in Section 3.1.1 above.

2D-to-3D registration is performed as follows (Figure 3.2):

1. An initial estimate of object pose (translation and rotation in x, y, z directions) is used to initialize the registration process.
    - In this study, the initial estimate of object pose is generated by manual alignment of the 3D model with it's DRR estimate using a custom-designed graphical user interface.
2. A digitally reconstructed radiograph (DRR) is generated, using the initial pose estimate and the known locations of the x-ray source and detector. DRRs are generated by ray casting through the CT volume, and integrating the Hounsfield numbers of the voxels intersecting the rays.
3. A similarity measure is used to compare the acquired fluoroscopy image with the DRR image.
    - In this study, the similarity measure used is the normalized cross correlation [3] between the gradient images of the fluoroscopy and DRR images.

4. A search strategy based on optimization of the object pose is used to select a new pose estimate, and steps 2-4 are repeated until convergence criteria are met (the similarity measure meets a pre-selected threshold, or the algorithm exceeds a selected number of iterations).

    - In this study, the gradient descent optimizer [5] and a multi-resolution registration method with 4 levels is used to reduce the chances of converging to a local maxima. At each level, the 3D model and 2D image are both subsampled, interpolated, and registered at the current level before moving onto the higher resolution level [6].

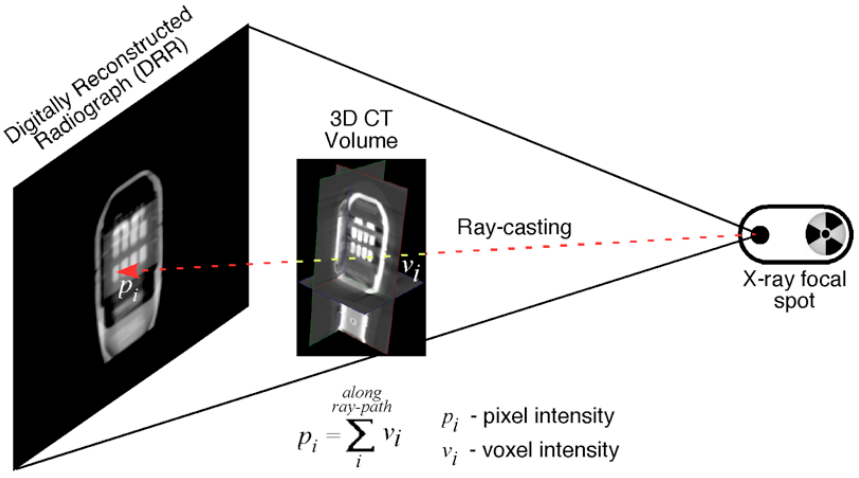

Fig. 3.2: Intensity-based 3D-2D registration

3.1.3 Fluoroscopy Imaging System Characterization

In order to perform 2D-to-3D registration of the TEE Probe model to the world coordinate system (both fiducial-based and intensity-based), several parameters of the fluoroscopy imaging system must be characterized, including:

- The source-to-detector distance (location of the x-ray focus relative to the detector plane),
- The transform mapping the 2D image points into the 3D world coordinate system (Direct Linear Transform (DLT) transform),

- The transformation describing the geometric distortion introduced by the earth's magnetic field and local ferrous objects. Note that this step is only necessary for image-intensifier detecting systems and is not required for flat panel detectors.

The source-to-detector distance and DLT transform can be characterized by acquiring fluoroscopy images of a calibration cage consisting of two parallel radio-translucent plates embedded with radio-opaque markers (control and fiducial plane), as described by Selvik *et al.* [7]. The locations of the markers in the calibration cage are precisely manufactured, and the measured locations on the fluoroscopy image are compared to the physical locations to determine the DLT transform mapping the 3D points to 2D. The calibration cage used in this study is shown in Figure 3.3.

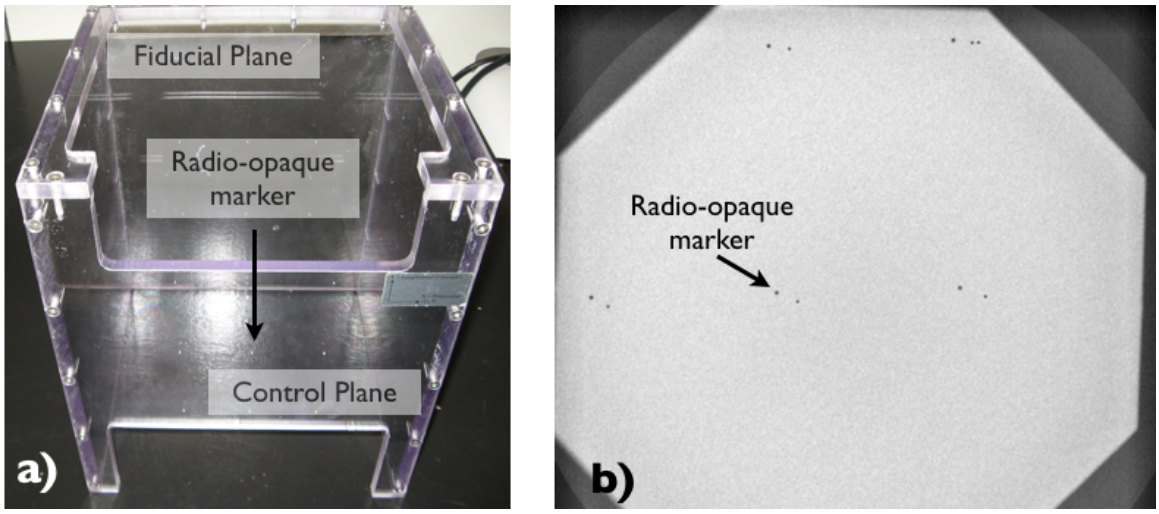

Fig. 3.3: (a) Calibration Cage (b) Fluoroscopy image of the calibration cage

A de-warping grid (Figure 3.4) was employed to correct geometric distortions of fluoroscopy images acquired on image intensifier systems [8], a step that is not required where flat panel detectors are employed.

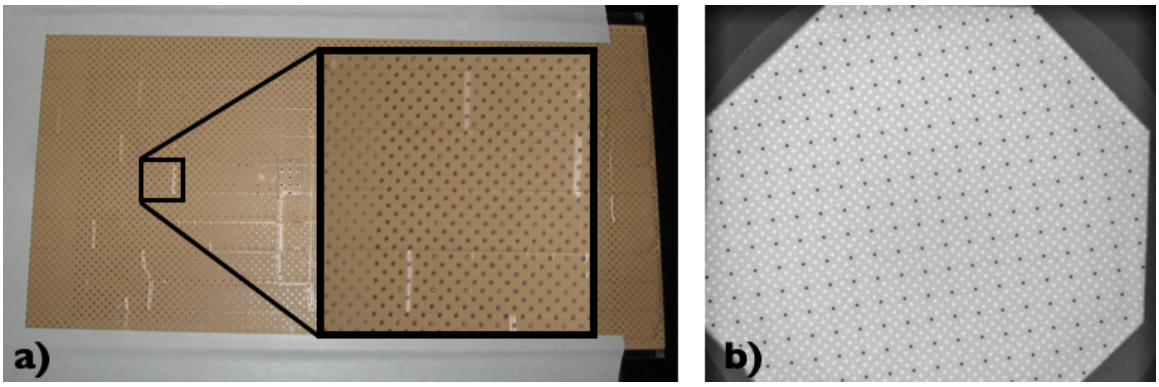

Fig. 3.4: (a) Calibration Grid with embedded radiopaque markers. (b) Fluoroscopy image of the calibration grid.

3.1.4 Equipment and Materials

Imaging Systems

The TEE probe used in this study was a Philips iE33 ultrasound system with an X7-2t 3D TEE probe (Philips Healthcare), and fluoroscopy images were acquired on a floor-mounted C-arm radiography system equipped with an X-ray Image Intensifier (Axiom Artis, Siemens Medical, 66.0kVp and 36mA, 10ms, isotropic resolution of 0.19mm).

Tracking attachment

A custom tracking attachment (Figure 3.5), roughly the same size as the TEE probe, was added to the end of the TEE probe (instead of adjacent to the TEE probe head) to ensure that the radio-opaque fiducials used for fiducial-based tracking did not affect the intensity-based tracking results (the FOV used for the analysis excluded the fiducials). The rigid-body attachment was 15mm x 15mm x 20mm, and contained seven spherical tantalum markers (radius 0.5 mm).

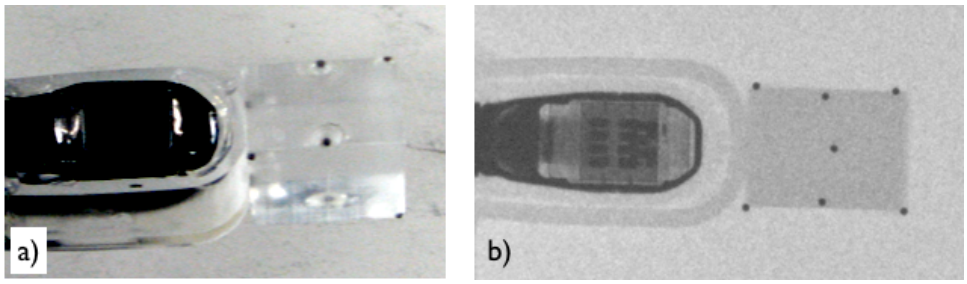

Fig. 3.5: (a) TEE Probe with tracking attachment. (b) Fluoroscopy image of the TEE Probe and tracking attachment.

Model Generation

A 3D model of the TEE probe geometry and attached fiducials is required to perform pose estimation. In this study, the 3D model was generated using a micro-CT scan (eXplore Locus Ultra, GE Healthcare, 0.150mm isotropic voxel spacing, 110kVp, 32mA) of the TEE probe head and attached fiducials.

For fiducial-based registration, the 3D model consists of the locations of each tracking fiducial in the local coordinate system of the TEE probe, as measured on the microCT scan using region growing and centroiding operations available on micro-CT analysis software (MicroView, GEHealthcare). Fiducial locations were manually selected to distribute the fiducials as evenly as possible in 3D space, and are described in Appendix C.

For intensity-based registration, the microCT image of the TEE probe head is used directly as the 3D model, excluding any attached external fiducial markers.

3.2 Experiment 1: Theoretical Limits on Localization Precision Using Intensity-Based Pose Estimation

Performance of the intensity-based pose estimation depends highly on the tracked object's geometry and the noise and resolution in the fluoroscopy images. In this section we estimate the theoretical maximum achievable performance of single-perspective

intensity-based pose estimation using the autocorrelation graph of the TEE probe.

3.2.1 Methods

Autocorrelation graphs are generated by calculating the similarity between the projection image of an object and a reference image as the object is translated or rotated about each axis (Figure 3.6). The autocorrelation profile of an object depends on the geometry of the object; objects that have a steep slope near the peak exhibit better tracking behaviour since small displacements lead to a large drop in the similarity metric, reducing the impact of noise. Furthermore, multiple local maxima near the peak may indicate that the object may be difficult to track without extremely close initialization, as an optimization algorithm is likely to erroneously converge to local peaks. A unit impulse function represents an optimal autocorrelation graph, with a high similarity metric only when the projection image was generated at the same position as the reference image. Due to noise and limited resolution and contrast, an optimization algorithm searching for the correct pose (corresponding to the peak of the autocorrelation graph) will likely converge at a similarity metric of less than one. The distance corresponding to this difference in similarity metric on the autocorrelation graph represents the localization precision (Figure 3.6).

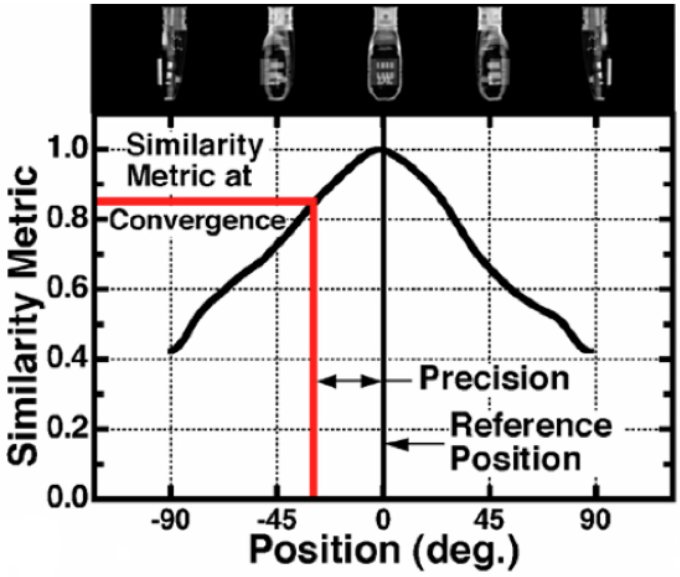

Fig. 3.6: Autocorrelation graph demonstrating the reference position, and the estimation of tracking precision based upon the similarity metric at convergence.

The maximum similarity metric achieved during the registration process depends on the optimization algorithm, step size, image and model resolution, object geometry and presence of noise. The similarity metric at convergence in our OR system can be evaluated by registering the CT volume of the TEE probe to ideal DRR images generated from the same CT (using the same resolution as the fluoroscopy images), eliminating the error introduced by poor contrast and image noise. The similarity metric at convergence of these ideal images was used to determine the tracking precision in each direction (Figure 3.6). The algorithm is initialized fifteen times to a random position within 2mm and 2° of the actual pose to ensure convergence to the proper peak, and the mean of these values was used as the similarity metric value at convergence. The Insight-Toolkit (itk) implementation [9] of the gradient descent optimizer, with a step size of 0.001mm was used.

In this study, the reference position was defined with the TEE probe transducer parallel to the imaging detector, and positioned 300 mm above the imaging detector with a source-to-detector distance of 1000 mm (Figure 3.7). Translations and rotations are relative to the centre of the TEE transducer, and the normalized cross

correlation calculated on the gradient images was used as the similarity metric.

Probe localization precision was measured in each of the 6 degrees of freedom independently, and on both ideal images, and noisy images (Gaussian noise level of 2.5%, representative of clinical images collected on our system). The noise level was selected by measuring the noise in a region of interest (corresponding to free air) taken from a clinical fluoroscopy image.

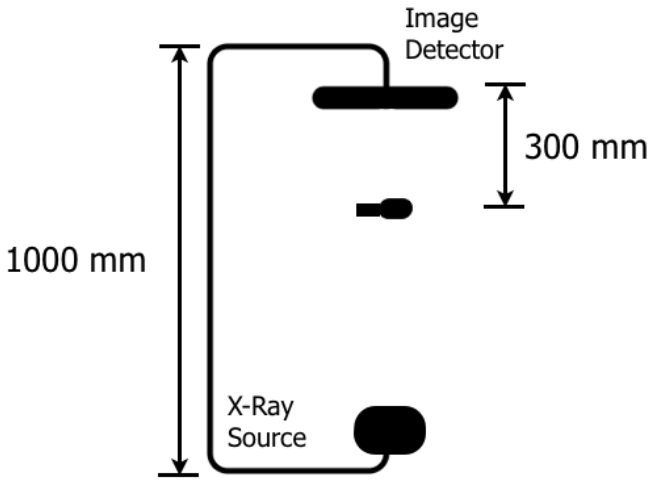

Fig. 3.7: Projection geometry used in generating autocorrelation images.

3.2.2 Results

The coordinate system used is shown in Figure 3.8. The similarity metric at convergence was 0.99 and 0.84 when registering to ideal and noisy DRRs, respectively. TEE probe localization precision results are summarized in Table 3.1. The tracking errors are reported as displacement or rotation error of the probe (mm or °), and as the equivalent displacement error of a point on an US plane imaged with the probe. For this analysis, we have chosen a representative point: offset 7cm vertically and 3cm horizontally from the image midline. This point approximates common locations of relevant anatomy on clinical images.

Autocorrelation graphs for the TEE probe are shown in Figure 3.9. In-plane translations and rotations demonstrated high tracking accuracy, with narrow peaks

for both ideal and noisy cases, and expected tracking accuracies of less than 0.01mm and 0.1°. Out-of-plane translations and rotations performed well in the ideal case, but were significantly affected by the addition of noise (Table 3.1). Ideal and 2.5% noise images resulted in maximum US displacement errors of 0.16mm and 6.45mm respectively, significantly higher than clinically acceptable values. This suggests that single-perspective intensity-based TEE pose estimation can be used to estimate target locations, but is unreliable in applications requiring high accuracy.

Fig. 3.8: (b) Coordinate system used for relative tracking accuracy study, where the x-y plane lies on the sensor surface.

Table 3.1: Theoretical localization precision in each direction. Translations in mm and rotations are given in degrees.

	Ideal	Noisy
X Translation (mm)	0.0025	0.49
Y Translation (mm)	0.0047	0.49
Z Translation (mm)	0.0093	2.04
X Rotation (°)	0.064	2.64
Y Rotation (°)	0.063	2.26
Z Rotation (°)	0.016	0.34
Max. TEE Displacement (mm)	0.16	6.45

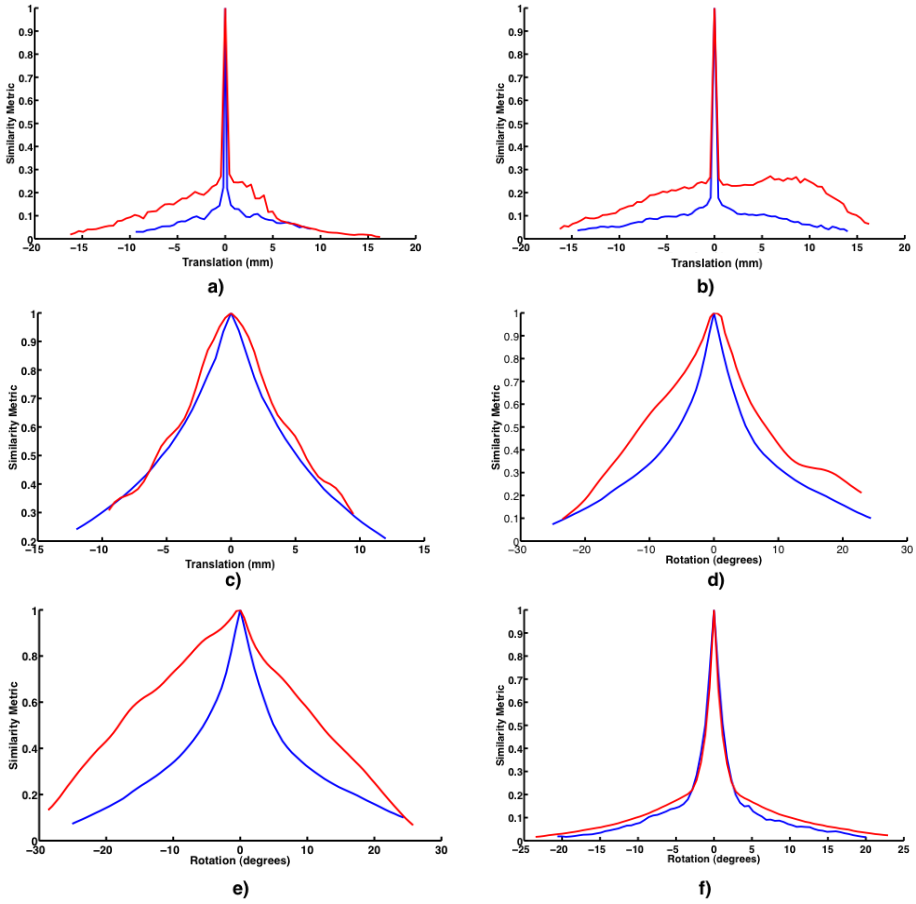

Fig. 3.9: Autocorrelation graphs for the TEE probe with ideal (blue) and noisy (red) image. (a) X Translation. (b) Y Translation. (c) Z Translation. (d) X Rotation. (e) Y Rotation. (f) Z Rotation.

3.3 Experiment 2: Relative Tracking accuracy

Relative tracking accuracy was assessed by applying known translations and rotations to the TEE probe using mechanical translation tables, and comparing to the displacements measured using TEE pose estimation. The performance of fiducial-based and intensity-based techniques are compared.

3.3.1 Methods and Materials

Custom attachment fixtures were used to mount the TEE probe onto a linear translation table with precision ± 0.003mm (J.A. Noll Co, Monroeville, Pennsylvania), or a rotation table with precision ± 5E-4° (Aerotech Inc, Pittsburgh, Pennsylvania), as shown in Figure 3.10. The probe coordinate system used is shown in Figure 3.8, and the face of the TEE transducer is assumed to be parallel to the imaging plane, since the translation tables rest on the OR table.

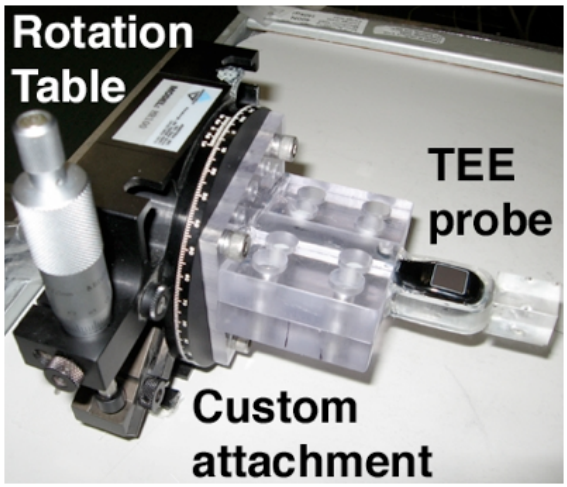

Fig. 3.10: Example of the TEE Probe mounted onto the rotation table.

A fluoroscopy image was acquired both prior and subsequent to each displacement. Each of the 6 degrees of freedom (x, y, z translation and rotation) were assessed independently. Sixteen to twenty-four displacements were applied in each direction, with steps sizes ranging from 0.635mm to 5.08mm and 1 to 10°. The number of samples and increment size were selected to represent a range of displacement increments and cover the maximum range of motion given the physical constraints of the setup; details are provided in Appendix D. The TEE was imaged in a standard operating room setup, at an approximate height of 30 cm from the x-ray detector, a distance representative of TEE probe positions in clinical images.

The same images were used to assess the accuracy of both fiducial-based and intensity-based tracking. The FOV used for the intensity-based pose estimation ex-

cluded the tracking fiducial attachment.

Images were processed offline on a personal computer with a 2.6GHz quad core CPU and 4GB of memory. The point-based algorithm requires manual initialization to establish correspondence between the rigid-body points and their projections within the fluoroscopy image. The intensity-based algorithm is initialized by defining a region of interest (excluding the radio-opaque markers), and manually estimating the initial registration parameters to provide the algorithm with a starting point.

3.3.2 Results

An example of the intensity-based pose estimation result is shown in Figure 3.11, and demonstrates the good visual alignment that can be achieved. Maximum tracking errors associated with the fiducial-based and intensity-based tracking were 0.58mm, 0.32° and 2.29mm, 3.76°, respectively (Table 3.2). Both techniques demonstrated a higher accuracy tracking in-plane movements compared to out-of-plane movements. This decreased accuracy is explained by the limited sensitivity of information available out-of-plane (the geometric magnification). Figure 3.12 illustrates the differences in both accuracy and precision between the fiducial-based and intensity-based techniques in the out-of-plane directions. The fiducial-based technique demonstrated greater accuracy than a 2D TEE probe mounted with an external magnetic sensor as described by Moore *et al* [10]. This experiment described a similar target registration error experiment, however slightly different experimental methods were used. The results of the intensity-based tracking are consistent with simulation results presented in Section 3.2, where intensity-based pose estimation demonstrated limited accuracy. In addition, the fiducial-based technique was more accurate, easier to implement, and was significantly faster.

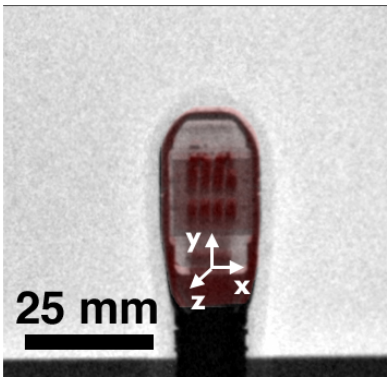

Fig. 3.11: Example registration result using intensity-based registration. The resulting DRR is overlaid in red on top of the original fluoroscopy image. The coordinate system used in this study is shown.

Table 3.2: Tracking error for fiducial-based and intensity-based methods. Translations are given in mm and rotations are given in degrees.

	Fiducial-based			Intensity-based		
	Mean	Stdev	RMS	Mean	Stdev	RMS
X Translation (mm)	0.16	0.17	0.21	0.35	0.39	0.52
Y Translation (mm)	0.18	0.18	0.21	0.16	0.25	0.30
Z Translation (mm)	0.48	0.33	0.58	0.63	2.28	2.29
X Rotation (°)	0.12	0.17	0.32	2.90	1.96	3.47
Y Rotation (°)	0.09	0.08	0.13	2.31	2.04	3.76
Z Rotation (°)	0.12	0.10	0.16	0.87	0.61	1.05

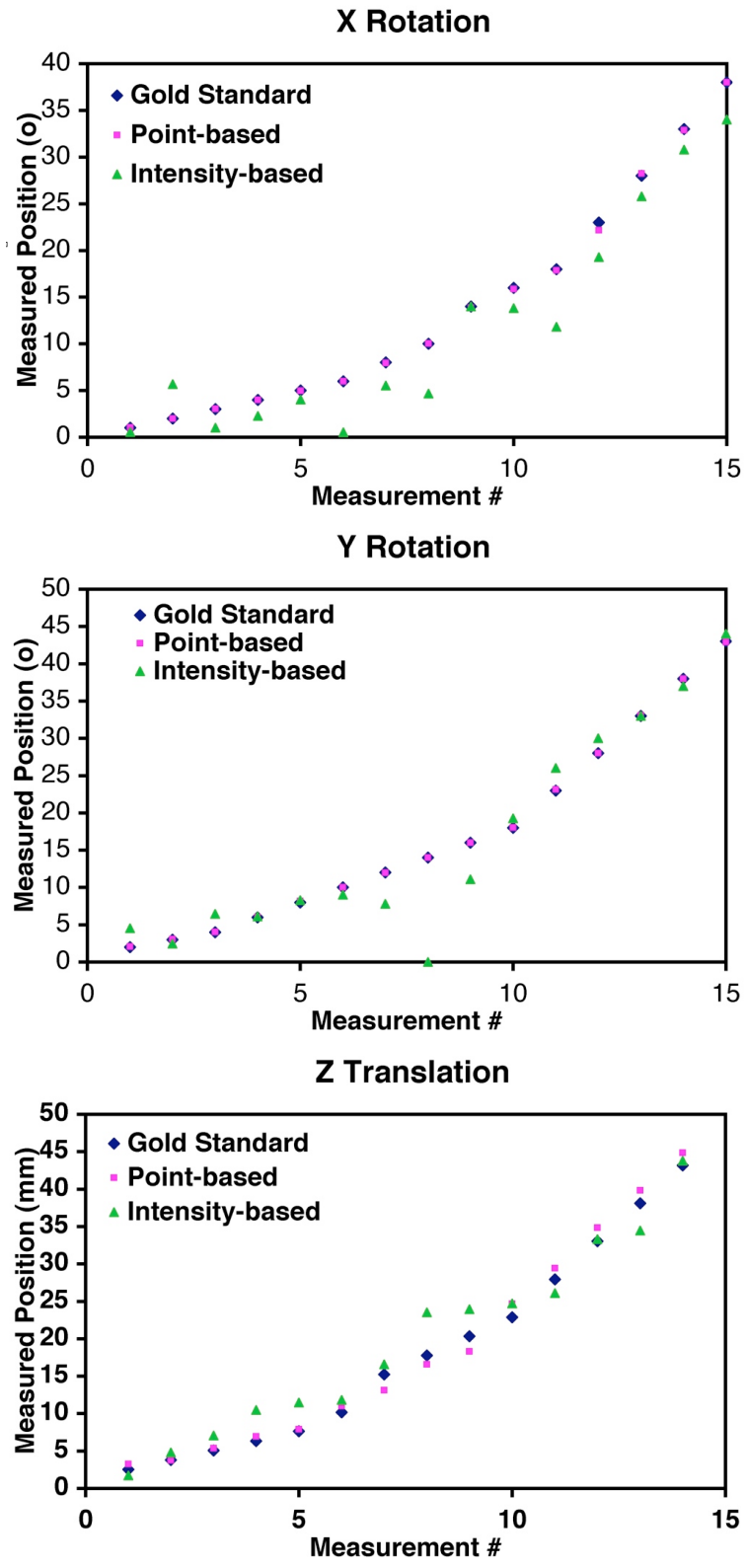

Fig. 3.12: Relative tracking accuracy results for the out-of-plane directions.

3.4 Experiment 3: TEE Probe Localization Precision using Fiducial-based Pose Estimation

During pose estimation of the TEE probe *in vivo*, tracking fiducials are frequently occluded by other surgical tools in the FOV or by the internal features of the TEE probe itself. TEE probe tracking accuracy is affected by the number of tracking fiducials used in the 2D-to-3D registration, whereby a larger number of fiducials reduces the effects of noise on 2D fiducial localization error, but increases the chances that the fiducials occlude each other or are mis-identified. The effect of the number of tracking fiducials used in the 2D-to-3D registration on localization precision was studied by systematically removing fiducials from the registration model used.

3.4.1 Methods

Twenty AP projections were acquired of the TEE probe for each of 8 positions. For each image, pose estimation was performed using 7, 6, 5 or 4 tracking fiducials. The 3D localization precision was reported as the standard deviation of each measurement from its sample mean. Image processing was performed as described in Section 3.3.

3.4.2 Results

TEE probe localization was within $\pm$ 0.01mm for in-plane translations, $\pm$ 0.35mm for out-of-plane translation, and $\pm$ 0.03° for the rotations (Table 3.3). Decreasing the number of tracking fiducials decreases localization precision for out-of-plane translation and for rotations, but had no effect on in-plane translations (Table 3.3 and Figure 3.13). A larger number of tracking fiducials reduced the effect of noise on 2D localization precision, which was propagated into 3D.

Table 3.3: TEE Probe Localization Precision (Standard Deviation). Translations are given in mm, and rotations are given in degrees. N = 160

Number of	Translation (mm)			Rotation (°)		
Fiducials	X	Y	Z	X	Y	Z
4	0.0069	0.0009	0.69	0.051	0.060	0.045
5	0.0058	0.0012	0.55	0.047	0.048	0.039
6	0.0060	0.0011	0.53	0.032	0.036	0.036
7	0.0059	0.0010	0.31	0.030	0.033	0.025

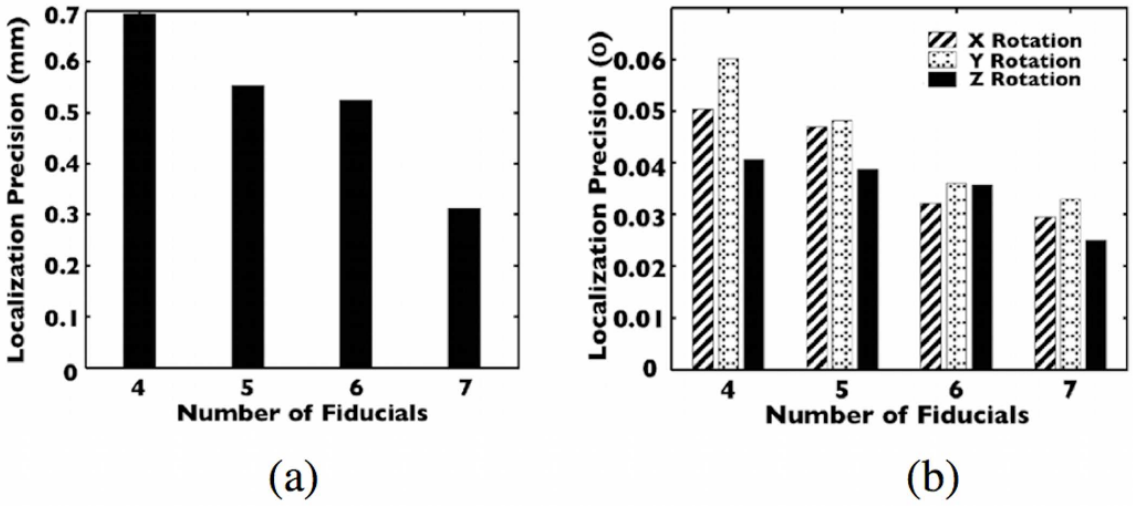

Fig. 3.13: Effect of number of tracking fiducials on TEE localization precision. (a) Translation in the out-of-plane (z) direction. (b)Rotations.

3.5 Discussion

The TEE probe was stationary during the localization and relative tracking accuracy studies presented in this chapter, and results reported represent an upper limit to the potential tracking accuracy that can be achieved given the size of the TEE probe, and the resolution, noise and contrast present in clinical fluoroscopy acquisitions.

Results suggest that fiducial-based TEE pose estimation is more suitable than intensity-based pose estimation for a TAVI image-guidance system. The fiducial-based technique allows for greater pose estimation accuracy and speed, and is less prone to convergence to incorrect solutions. However, an external tracking attachment is required to rigidly affix tracking fiducials to the TEE probe. The external dimensions of this attachment should be minimized to reduce risk of esophageal injury during manipulation of the probe.

The results of the theoretical localization precision study (Section 3.2) and the relative tracking accuracy study (Section 3.3) suggest that intensity-based 2D-3D pose estimation of the TEE probe provides inadequate tracking accuracy for implementation in a TAVI system. Accuracy results of these studies are consistent with those reported by Gao *et al.* [11, 12]. The addition of noise significantly reduces localization precision in the small features present in the TEE probe. The use of bi-plane images can reduce fluoroscopy noise, and Gao *et al.* [12] demonstrate improved results using bi-plane images. However, intra-operative bi-plane fluoroscopy is unavailable in the majority of centres, and the physical constraints of the operating room setup are not conducive to bi-plane imaging. Furthermore, due to the motion of the TEE probe during a procedure, image averaging is not a viable technique for noise reduction since a high temporal resolution is required to prevent image blurring. The impact of noise can potentially be reduced by introducing *a priori* information about the intrinsic probe geometry. Example of such techniques include shape or model-based tracking [13, 14].

Instead of using native TEE probe geometry, a pattern more conducive to intensity-based pose estimation can be introduced into the TEE probe head during the manufacturing process (for example metal etching patterns onto the internal or external surface of the TEE plastic cover). Such geometries would not significantly affect the external dimensions of the TEE probe head, but could provide improved results. Optimization of geometric patterns for pose estimation requires further study, and initial experiments comparing the performance of empirically selected patterns are explored in Appendix B.

The localization precision study (Section 3.4) demonstrates high pose estimation

precision with the fiducial-based technique. Localization precision is better in the in-plane than out-of-plane directions, and the out-of-plane directions demonstrate greater sensitivity to fiducial occlusion. Further work is required to determine the optimal number and placement of fiducials to maximize accuracy while minimizing fiducial overlap and point correspondence failure.

Fiducial-based TEE probe pose estimation demonstrates better accuracy than a magnetically-tracked TEE probe [10], and allows for TEE probe tracking in TAVI applications without the introduction of bulky OR equipment.

3.6 Chapter Summary

In this chapter, several experiments were conducted to assess the performance of intensity-based and fiducial-based single-perspective TEE pose estimation. Intensity-based pose estimation demonstrated insufficient accuracy (rotational errors of up to 3.5°) for a real-time TAVI application. Fiducial-based pose estimation demonstrated better localization precision and accuracy, and this technique is used in Chapter 4 to register TEE and fluoroscopy images.

References

[1] Hoffmann KR, Esthappan J. Determination of three-dimensional positions of known sparse objects from a single projection. Medical Physics. 1997;24(4):555–564.

[2] Schonemann PH. A generalized solution of the orthogonal procrustes problem. Psychometrika. 1966;31(1):1–10.

[3] Penney GP, Weese J, Little JA, Desmedt P, Hill DLG, Hawkes DJ. A comparison of similarity measures for use in 2D - 3D medical image registration. IEEE Transactions on Medical Imaging. 1998;17(4):586–595.

[4] Penney GP, Batchelor PG, Hill DLG, Hawkes DJ, Weese J. Validation of a two- to three-dimensional registration algorithm for aligning preoperative CT images and intraoperative fluoroscopy images. Medical Physics. 2001;28(6):1024–1032.

[5] Press WH, Teukolsky SA, Vetterling WT, Flannery BP. Numerical Recipes in C: The Art of Scientific Computing, 2nd Ed. Cambridge University Press, New York; 1992.

[6] Corvi M, Nicchiotti G. Multiresolution image registration. In: Proceedings of the International Conference on Image Processing. vol. 3; 1995. p. 224 – 227.

[7] Selvik G, Alberius P, Aronson AS. A roentgen stereophotogrammetric system. Construction, calibration and technical accuracy. Acta Radiologica - Series Diagnosis. 1983;24(4):343–352.

[8] Fahrig R, Moreau M, Holdsworth DW. Three-dimensional computed tomographic reconstruction using a C-arm mounted XRII: correction of image intensifier distortion. Med Phys. 1997;24(7):1097–106.

[9] Yoo TS, Ackerman MJ, Lorensen WE, Schroeder W, Chalana V, Aylward S, et al. Engineering and Algorithm Design for an Image Processing API: A Technical Report on ITK - The Insight Toolkit. vol. 85 of Studies in Health Technology

and Informatics (Proceedings of Medicine Meets Virtual Reality). IOS Press, Incorporated; 2002. p. 586–592.

[10] Moore JT, Wiles AD, Wedlake C, Bainbridge D, Kiaii B, Trejos AL, et al. Integration of trans-esophageal echocardiography with magnetic tracking technology for cardiac interventions. In: Medical Imaging 2010: Visualization, Image-Guided Procedures, and Modeling, Proceedings of the SPIE.. vol. 7625; 2010. p. 76252Y–76252Y–10.

[11] Gao G, Penney G, Gogin N, Cathier P, Arujuna A, Wright M, et al. Rapid Image Registration of Three-Dimensional Transesophageal Echocardiography and X-ray Fluoroscopy for the Guidance of Cardiac Interventions. In: Lecture Notes in Computer Science: Information Processing in Computer-Assisted Interventions. vol. 6135; 2010. p. 124–134.

[12] Gao G, Penney G, Ma Y, Gogin N, Cathier P, Arujuna A, et al. Registration of 3D trans-esophageal echocardiography to X-ray fluoroscopy using image-based probe tracking. Medical Image Analysis. 2012;16(1):38–49.

[13] Fregly BJ, Rahman HA, Banks SA. Theoretical accuracy of model-based shape matching for measuring natural knee kinematics with single-plane fluoroscopy. Journal of Biomechanical Engineering. 2005;127(4):692–699.

[14] Tsai TY, Lu TW, Chen CM, Kuo MY, Hsu HC. A volumetric model-based 2D to 3D registration method for measuring kinematics of natural knees with single-plane fluoroscopy. Medical Physics. 2010;37(3):1273–1284.

Chapter 4

TEE-Fluoroscopy Registration

In this chapter, an algorithm for registering TEE and fluoroscopy images using fiducial-based TEE probe pose estimation (Section 3.1.1) is presented. To minimize workflow interruption and intra-operative setup, a method for automatic tracking initialization, point correspondence and fiducial centroid determination is developed, allowing for a fully automated tracking and registration algorithm. An assessment of registration accuracy and system robustness is performed using phantom, *ex vivo* and *in vivo* images of porcine subjects. Finally, the proposed OR workflow and visualization options are presented.

The tracking algorithm software in this chapter was developed in C++, and run on a personal computer equipped with a 2.0GHz processor and 1GB of memory. The software used for algorithm validation and testing was developed in Matlab (Mathworks,Natwick, MA). In the validation studies presented, all image processing was performed offline.

4.1 Registration Method Overview

The mathematical transformations required to re-project a point in the TEE image onto the fluoroscopy image is shown in Figure 4.1 and given by Equation 4.1.

$$P_F = T_{F \leftarrow W} \bullet T_{W \leftarrow Pr} \bullet T_{Pr \leftarrow US} \bullet P_{US} \tag{4.1}$$

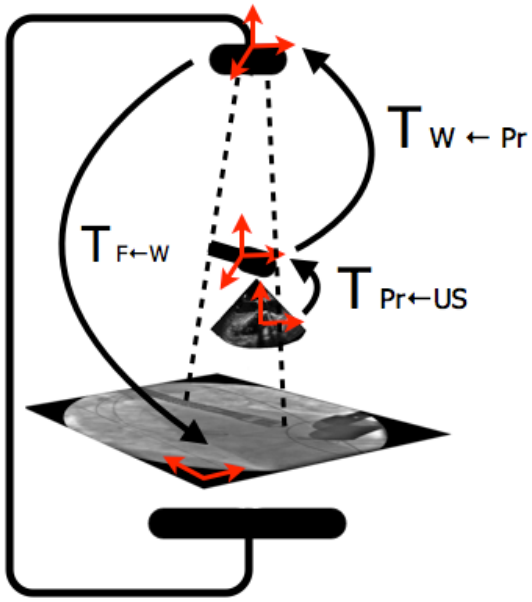

Fig. 4.1: Transformations required to project a point on the US image plane onto the fluoroscopy image plane.

where:

- US and F are the ultrasound and fluoroscopy image coordinate systems (2D)
- Pr and W are the TEE probe local coordinate system and world coordinate systems (3D)
- P_{US} and P_F are image points in US and fluoroscopy

$T_{Pr \leftarrow US}$ relates the ultrasound image to the local coordinate system of the TEE probe, and is given by an US calibration transform. This transform is fixed, and the process used to determine it is described in Section 4.3. $T_{W \leftarrow Pr}$ is the tracking transformation determined by a single perspective pose estimation that describes the position of the TEE probe in 3D space (Section 3.1.1). $T_{F \leftarrow W}$ is the fluoroscopy projection transformation determined by the geometry of the fluoroscopy system (Section 3.1.3) .

A summary of all the registration steps is provided in Figure 4.2 with each component being described in detail in the following sections.

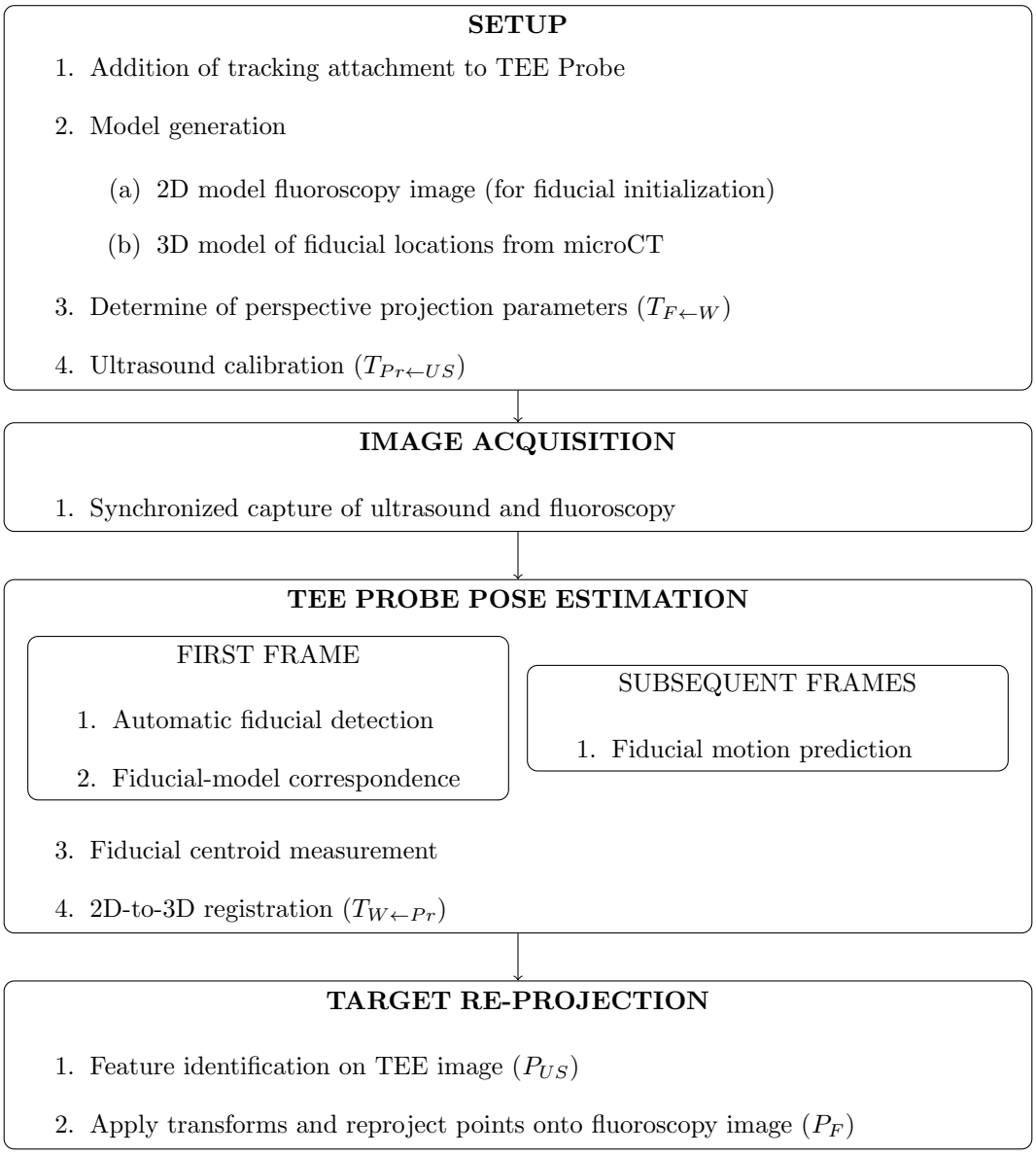

Fig. 4.2: Overview of the registration process.

4.2 TEE Probe Attachment

A tracking attachment (Figure 4.3), was fitted to a standard TEE transducer. For the initial tracking accuracy experiments in Chapter 3, the attachment was manufacturing from plexiglass and attached to the TEE probe head end (Figure 4.3a,b).

To allow for a more realistic study of tracking performance (allowing for fiducial occlusions and more closely mimicking the TEE geometry), a form-fitting casing was manufactured using rapid prototyping (Figure 4.3c,d). This attachment was used for the point target and *ex vivo* accuracy studies. Finally for *in vivo* use, a soft attachment (Figure 4.3e,f) was used to minimize potential esophageal injury during manipulation of the probe. This attachment was manufactured from medical grade silicone (Masterbond, New Jersey, USA), and molded directly on the the TEE probe head for a secure fit. Furthermore, the silicone attachment allows the overall dimensions of the probe head to be minimized. Clinical experience suggests that an attachment of this size can safely be used in the majority of patients.

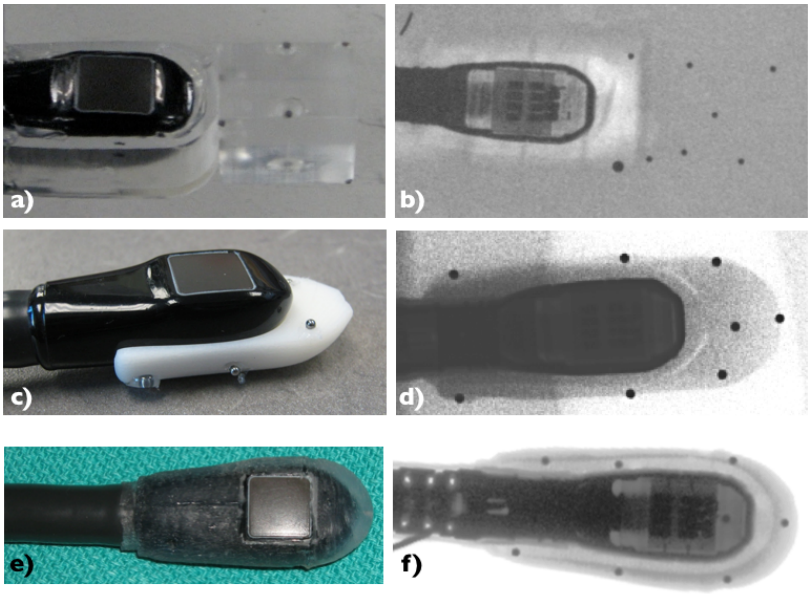

Fig. 4.3: Iterations of the TEE probe attachment. (a-b) 1st generation. (c-d) 2nd generation. (e-f) 3rd generation. Fiducial locations are described in Appendix C.

In this study, a custom 3-part mold (Figure 4.4) was used create the silicone attachment in a two-step process. The silicone is set around the head of the probe, and divots are left for the tantalum fiducials. A second layer of silicone was then used to seal in the fiducials (1mm radius medically inert tantalum beads typically used in orthopedic radiostereometric applications). The silicone is stiff enough to ensure that

there will be no relative motion of the tracking fiducials.

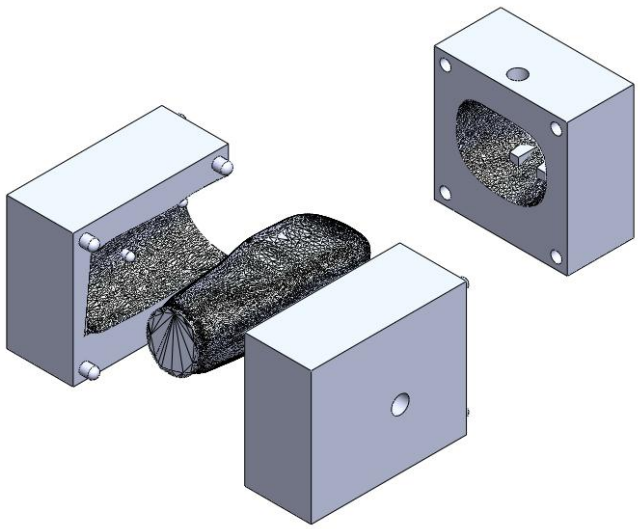

Fig. 4.4: Three part mold used to form silicone cover.

.

4.3 Z-Bar Calibration

Ultrasound calibration is the process of determining the transform relating the ultrasound image coordinate system to that of the TEE transducer head. US calibration is achieved by imaging a spatially tracked object of known geometry with a spatially tracked probe. In this study, a variation of the Z-bar design described by Gobbi *et al.* was used [1] as the registration phantom (Figure 4.5) . Homologous points on the object identified within US images and on the object model were registered together in a Procrustes least-squares sense [2] to determine the calibration

transformation. Eight 1mm tracking fiducials were attached to the Z-bar, allowing its position in world coordinates to be determined by single perspective 2D-to-3D pose estimation. A microCT (GE eXplore Locus Ultra, Milwaukee, WI) scan of the TEE probe and Z-bar (140kVp, 13mAs) were used as object models.

Points were identified in the TEE image using thresholding and an intensity-weighted centroiding algorithm (Figure 4.5). Multiple images of the Z-Bar acquired with the TEE probe in different positions were used to provide a total of 242 points (11 points are acquired in each image. The RMS fiducial registration error of this US calibration was 2.33mm, which is consistent with ultrasound calibration performed with magnetic tracking by other groups [3, 4, 5]. This ultrasound calibration error was the result of localization error in the calibration fiducials (Z-bar strings) due to elevation thickness artifacts, and tracking error of the TEE probe and calibration object during the calibration process. The calibration transform determined in this step was used for all subsequent target registration experiments.

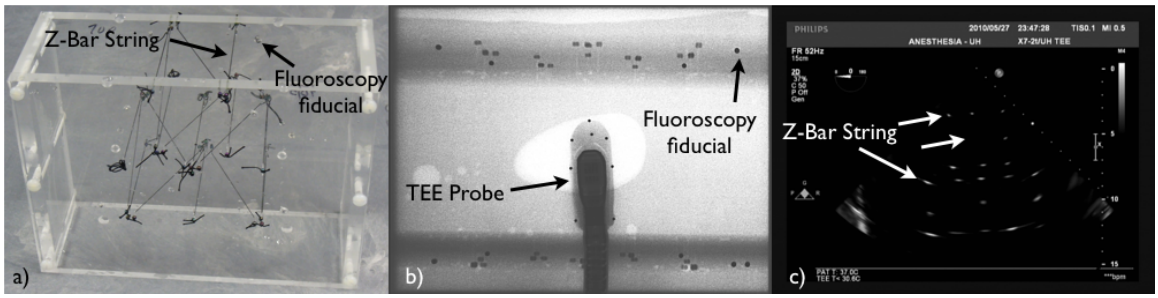

Fig. 4.5: (a) Z-Bar. (b) Fluoroscopy image. 1mm tracking fiducials are used to estimate Z-Bar coordinates in the world coordinate system using 2D-to-3D pose estimation. (c) TEE image. The geometry of Z-Bar fiducial strings on the 2D TEE image is used to determine where the 2D TEE image intersects the Z-Bar object. 2D-to-3D pose estimation is used to estimate the location of the TEE Probe

4.4 Fluoroscopy Tracking Initialization

The tracking algorithm must be initialized with an estimate of fiducial centroid locations on the first 2D fluoroscopy frame. During entry and exit of the TEE probe from the esophagus, the TEE probe transducer face is constrained to be approximately parallel to the detector. A 2D intensity-based registration was used to roughly align a fluoroscopy model image of the TEE probe (Figure 5.2a) to the first frame in each acquired sequence, allowing the initialization process to be fully automatic without user input. A Nelder-Mead Simplex algorithm was used to optimize X and Y translation, image scale and in-plane rotation using the normalized cross correlation as the image registration metric. The image-based registration was initialized using an exhaustive search iterating over 10 possible X and Y positions to grossly align the model with the TEE probe in the input image.

Once registered, the model fiducial locations were projected onto the fluoroscopy image and the following steps are used to identify an approximate fiducial centroid location (Figure 5.2b):

1. A local region of interest (ROI) window was defined around each projected point. The size of the ROI window was 10 times the fiducial diameter at the resultant magnification.

2. For each ROI:

   (a) The algorithm iterated through potential local threshold values (in increments of 0.05). For each possible threshold:

      i. Connected components labelling was used to identify potential fiducial regions.

      ii. Area and eccentricity criteria were used to exclude regions of the incorrect shape and size. In this study, regions were excluded when (Area - Target Area)/Area > 0.75 or eccentricity > 0.8. Lower thresholds result in higher rates of missed fiducials, while higher thresholds increase the chances of misidentified fiducials.

iii. Each remaining region was scored based on a weighted combination of region eccentricity (30%) and deviation from the target area (70%). The area criterion was given a greater weight than eccentricity since it is less sensitive to noise and partial area effect, particularly in cases with smaller fiducials or larger pixel spacing where each fiducial is comprised of a small number of pixels.

(b) The centroid of the highest scoring region was accepted.

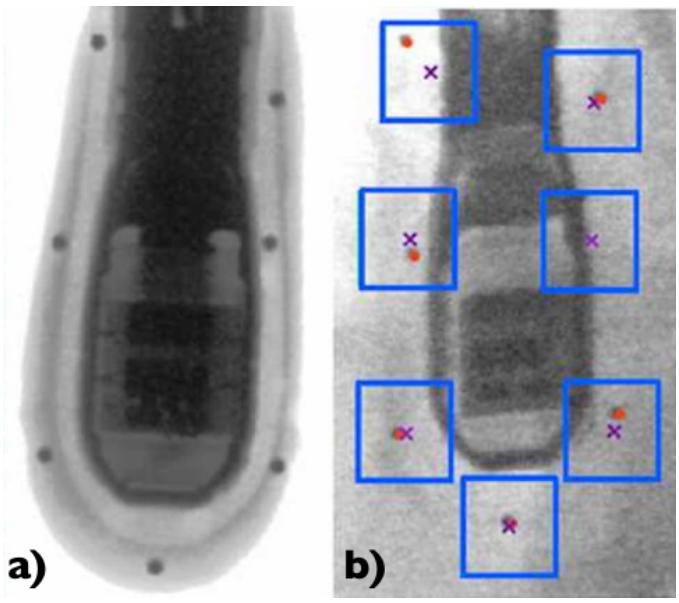

Fig. 4.6: (a) Fluoroscopy model image used for fiducial initialization, fiducial centroids on the model image were identified manually. (b) Example of fiducial initialization. Purple crosses represent the projected fiducial estimate based on 2D model to image registration. Blue boxes represent the local ROI regions for each fiducial defined around the projected fiducial estimates. Red dots represent the final fiducial centroid estimates found by the initialization algorithm. In this example one fiducial is not detected due to occlusion by internal TEE probe geometry.

4.5 Point Correspondence Determination

Determination of the correspondence between the 2D centroids and the 3D model was accomplished using a combined pose estimation and feature-association algorithm as follows:

1. The 3D model was rotated iteratively, and at each position:
   (a) The 3D model was aligned in-plane with the 2D fluoroscopy image using the centre of mass of the initialized fiducials.
   (b) Out of plane position was estimated by matching the estimated magnification of the convex hull of the 2D projected model fiducials to the convex hull of the centroided image fiducials.
   (c) The 2D projected model points corresponding to the 3D pose was calculated.
   (d) The correspondence between the 2D measured centroids and the 2D projected model points was determined using a feature-association algorithm described by Pilu and Maurizio [6]. This algorithm is based on singular value decomposition of a proximity matrix $G_{ij} = e^{-r_{ij}^2}/2\sigma^2$ with r_{ij} being the Euclidian distance between the i^{th} point in the first point set and the j^{th} point in the second point set.
   (e) 3D to 2D registration was attempted using the correspondence determined in step 3b), and the correspondence was either accepted or rejected using the RMS registration error (accept if error was less than double the pixel spacing). An iterative global search was applied until an accepted correspondence was determined in step 3c).

Fiducial Centroid Measurement

Once correspondence was established, a search algorithm was used to determine centroids of the fiducials in all subsequent frames. A predictive algorithm [7] was used to localize fiducial projections in each frame, and the identification and measurement of their centre position was accomplished using the following image operators:

1. A region of interest (ROI) window centered about the predicted fiducial location was defined.

2. The ROI was convolved with a Laplacian of Gaussian (LoG) (Kernel dimension = 9 x 9, $\sigma = 2.0$) to smooth gray scale values and enhance edges.

3. A locally calculated threshold (threshold = min + 0.5*(max-min)) was applied to the ROI window to segment pixels into foreground and background.

4. Connected components labelling [8] and the circular Hough transform [9] were used to eliminate inappropriately sized regions:

   (a) Regions with an area <50% or >150% of the expected area calculated from the fiducial size and approximate magnification were excluded.

   (b) A circular Hough transform was used to search for circles of the expected radius size in pixels ± 1 pixel. The threshold used to binarize the accumulator was 1/2 the circle circumference.

5. Intensity-weighted centroiding [10] was used to measure the centre position of each remaining region, and the region closest to the predicted fiducial location was selected as the fiducial centroid.

4.6 Experiment 1: Accuracy Assessment

The accuracy of the TEE-fluoroscopy registration is evaluated on:

1. Static phantoms
2. An *ex vivo* porcine specimen
3. *In vivo* porcine subjects images

The static phantoms were tracked in 3D space using 2D-3D pose estimation, and allow for an estimate of 3D registration error. The *ex vivo* specimen has similar contrast as that found in the *in vivo* subject images, but allows for the addition of pin targets to be embedded within the aorta, permitting quantification of tracking error

without errors introduced by poor target identification or temporal mis-alignment. *In vivo* porcine images best represent the tracking error that would be experienced intra-operatively with an image-guidance system.

4.6.1 Methods

4.6.1.1 Equipment and Materials

The TEE probe used in this study was a Philips iE33 ultrasound system with an X7-2t 3D TEE probe (Philips Healthcare). MicroCT models of the probe and phantom targets were acquired on a GE eXplore Locus Ultra (Milwaukee, WI), with an isotropic voxel spacing of 0.153mm. Fluoroscopy images for US calibration, tracking accuracy studies and the point target registration study were acquired on a floor-mounted C-arm XRII (Axiom Artis, Siemens Medical, Munich), at 66.0kVp and 36mA, 10ms, isotropic resolution of 0.19mm. The *ex vivo* study was performed on a Medtronic O-arm (Minneapolis, MN, USA), at 65.0kVp and 17mA, isotropic resolution 0.388mm. The *in vivo* images were acquired on a GE OEC 9900 mobile C-arm (Milwaukee, WI, USA) at 96.0kVp and 146mA, 10ms, isotropic resolution 0.21mm. Fluoroscopic acquisition parameters were determined automatically by the manufacturer's imaging control loop.

4.6.1.2 Error assessment

Registration error was assessed by measuring the target registration error (TRE) of pins, catheters or wires. All targets on the ultrasound images were identified semi-automatically using an intensity-weighted centroiding algorithm initialized by a user click. Pin targets on the fluoroscopy images were identified manually. For the *in vivo* study, the guidewire and catheters in the fluoroscopy images were segmented automatically, using an algorithm described in Section 4.6.1.5.

4.6.1.3 Phantom Experiments

Point Target Phantom

The point target phantom consisted of 4 pins mounted on a lego base, shown in Figure 4.7. Sorbothane (Sorbothane, Kent, OH) was used to reduce reverberation artifacts from the plastic and metal in the target. Twelve TEE and fluoroscopy image pairs corresponding to 24 targets were registered together. Radio-opaque markers were added to the frame, allowing the 'ground truth' cross locations to be defined using microCT data, and the fiducial-based pose estimation described in Section 3.1.1.

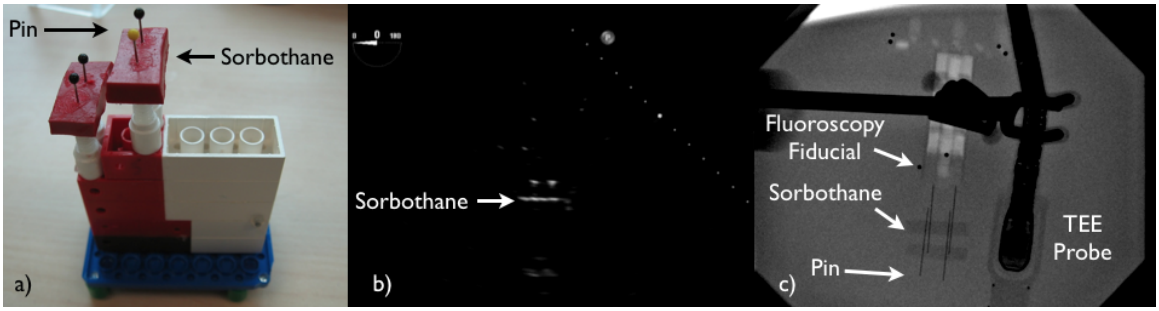

Fig. 4.7: (a) Pin Target Phantom. (b)TEE image of pin target phantom. (c) Fluoroscopy image of pin target phantom.

Table Tennis Ball Phantom

The table-tennis phantom consisted of a table-tennis ball mounted on a frame (Figure 4.8). The ''ground truth' location was determined using the same method as the point target phantom described above. Six cross-sectional US images of the ball were acquired at varying angles and locations used in clinical practice. The centroid of the cross-section was identified using a least squares best fit ellipse to manually identified points and used as the target.

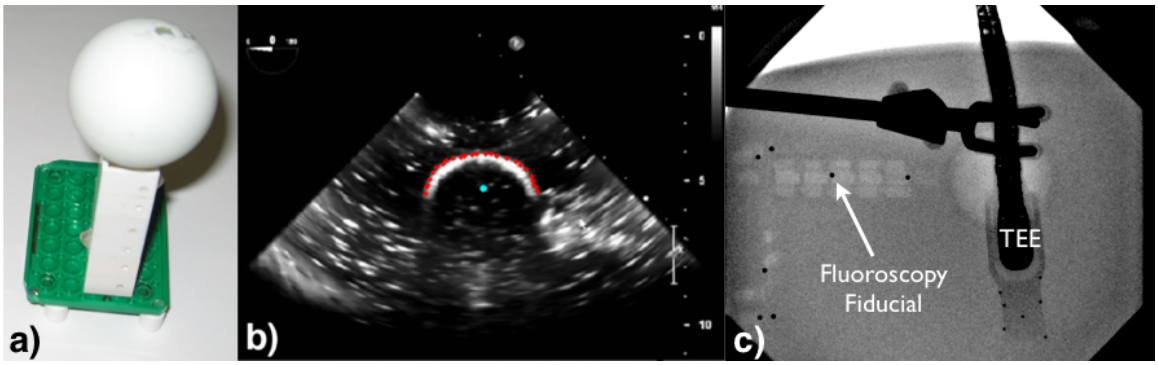

Fig. 4.8: (a) Table Tennis Ball Phantom. (b)TEE image of table tennis target phantom. Red dots denote manually selected border points, and the cyan dot denotes the fitted centroid. (c) Fluoroscopy image of table tennis target phantom.

Heart Phantom

The heart phantom (The Chamberlain Group, Great Barrington, USA) is shown in Figure 4.9, and was used for a visual assessment of registration performance. It is similar in size and anatomy to the human heart, with echogenic properties that are acceptable for TEE imaging. Alignment of the heart borders was used to assess registration performance.

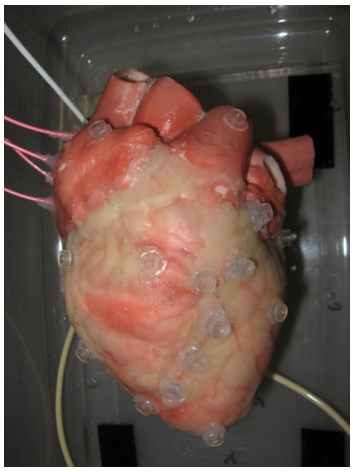

Fig. 4.9: Heart Phantom (Chamberlain Group)

4.6.1.4 Ex Vivo Porcine Heart Experiment

An *ex vivo* porcine heart specimen was prepared by filling the aortic root with a $30mg/ml$ Omnipaque 300 (GE Healthcare, Mississauga, ON) and agar mixture (Figure 4.10). This mixture was liquid during filling, but solidified rapidly, allowing the aortic root to remain relatively rigid during imaging. In addition to providing contrast to delineate the aortic root, the solution mimics the ultrasound properties of blood without significant artifacts, resulting in images similar to those obtained clinically. Five metal pins were embedded as targets, with 2 pins in the right and left coronary ostia, and 3 distributed in 1cm intervals along the aorta. Eight TEE and fluoroscopy image pairs (1 target visible on each image) were acquired and registered.

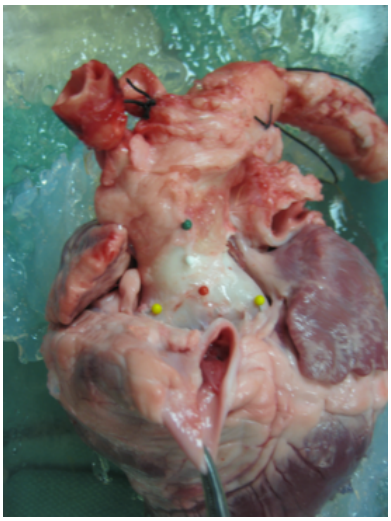

Fig. 4.10: *Ex vivo* porcine heart, with pin targets at the left and right coronary ostia, and along the length of the ascending aorta.

4.6.1.5 In Vivo Porcine Experiment

Five *in vivo* TEE and fluoroscopy image sequences of two porcine subjects approximately two seconds each were acquired and registered together. These sequences were identical to those acquired in a standard TAVI procedure, and include breathing and heart motion in the subjects. A 5 French (1.67mm diameter) catheter or 1mm diameter guidewire with the tip inserted into the ascending aorta were used as imaging

targets. Two hundred images corresponding to 1705 target points were acquired.

Target Identification

For the *in vivo* study, the guidewire and catheters were segmented automatically using the following image operators:

1. Thresholding and Canny edge detection were used to find the outline of the target.
2. Dilation and skeletonization was used to identify the centreline of the structure.
3. Spurious pixels were removed.
4. A B-spline was fitted to the identified points.

Temporal Calibration

Temporal calibration is required to ensure synchronized image capture, and in this study, the onset of motion of the target was used to establish a temporal reference. Temporal calibration is not required during real-time image registration in an image-guidance system, since simultaneous image capture occurs.

4.6.2 Results

The intra-operator variability of the gold standard manual segmentations of the pin targets (phantom and *ex vivo* specimen) had standard deviations of 0.18 mm and 0.05 mm for the ultrasound and fluoroscopy images respectively. The point target and ball phantoms were spatially tracked using 2D-to-3D pose estimation, allowing for a 3D unsigned distance TRE to be evaluated. The *ex vivo* and *in vivo* targets could not be spatially tracked due to a lack of a rigid geometry. The position of the targets identified on the US image were re-projected onto the fluoroscopy image plane, and a 2D unsigned distance reprojection target registration error (rTRE) was evaluated. In the TAVI procedure, the position of the stent is constrained by the position of the guidewire inside the aortic root, limiting the out-of-plane motion. Thus the 2D rTRE error best represents the targeting error encountered by physicians when guiding placement of a stent using ultrasound augmented fluoroscopy images. Magnification

correction was applied to distance measurements made on the fluoroscopy image by assuming that the height of the targets visible on the ultrasound image were approximately equal to the height of the TEE probe centre (calculated with respect to the detector).

4.6.2.1 Phantom Experiments

Point Target Phantom

Point target results are summarized in Table 4.1, and visualized in Figures 4.11, 4.12, and 4.13.

The point target locations measured on TEE demonstrate good alignment with the gold standard locations measured on fluoroscopy (Figure 4.11). The out-of-plane error measured on the point target was significantly higher than the in-plane error (Table 4.1), which is consistent with the tracking results described in Sections 3.3 and 3.4.

Table 4.1: Point Target Accuracy Results

	N	Mean (mm)	Std Dev (mm)	RMS (mm)
3D TRE	24	2.23	0.72	2.33
2D rTRE	24	0.68	0.33	0.75

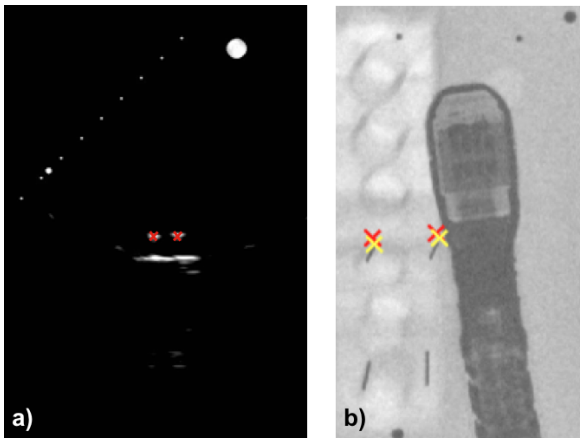

Fig. 4.11: Visualization of point target registration. (a) TEE manually selected pin target points. (b) Fluoroscopy of point target phantom. Manually selected gold standard points are shown in yellow, and corresponding point re-projected from TEE in (a) are shown in red.

The 3D locations of the TEE and phantom locations are reconstructed, and overlays of the surface reconstructed from CT with the TEE and fluoroscopy images are visualized (Figures 4.12 and 4.13), demonstrating good alignment between the model and the images. However, visualization and interpretation of the TEE and fluoroscopy image planes viewed simultaneously is difficult, particularly if the image planes are almost orthogonal to each other. Visualization options are further discussed in Section 4.8.

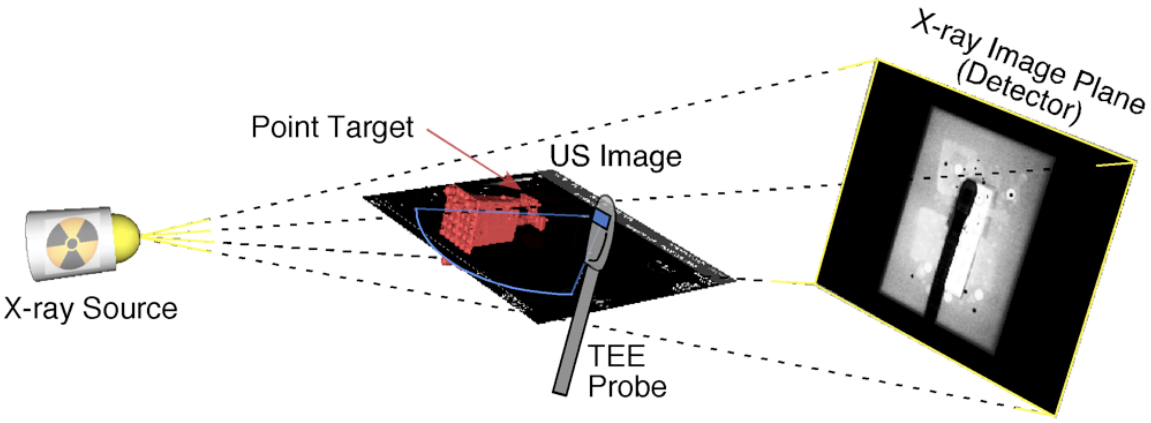

Fig. 4.12: Reconstructed locations of the TEE and fluoroscopy images, tracked phantom and x-ray source corresponding to the overlay images shown in Figure 4.13.

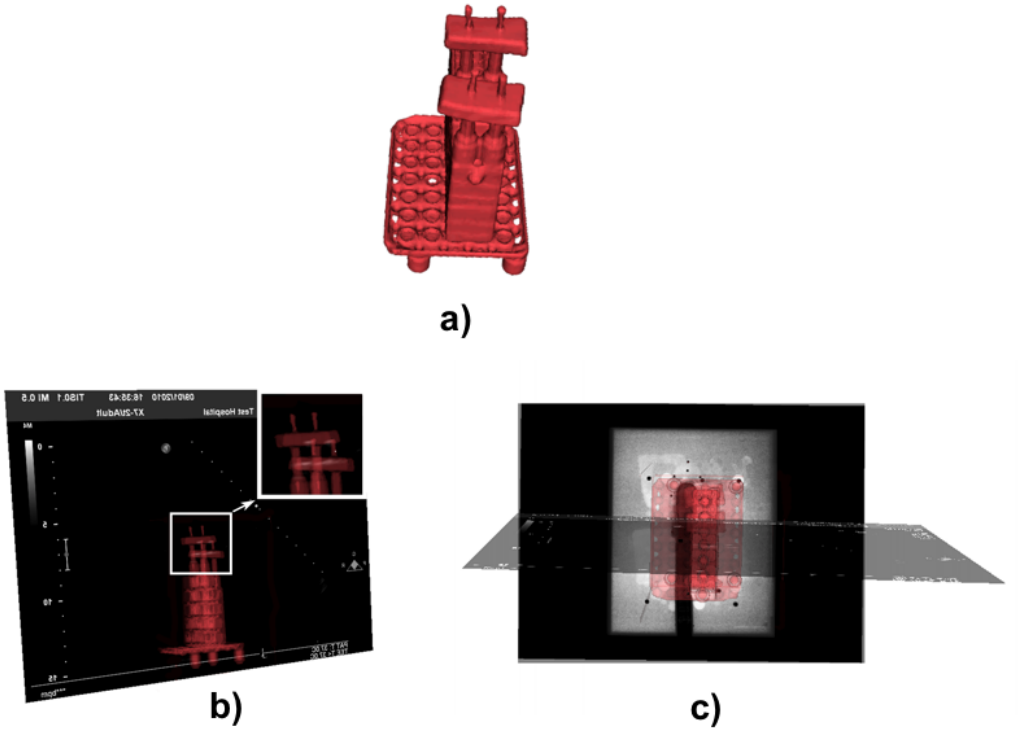

Fig. 4.13: Visualization of point target registration. (a) Point target surface reconstructed from microCT. (b) Overlay of tracked point target surface in (a) and TEE image. (c) Overlay of point target surface, TEE image and fluoroscopy image.

Table Tennis Ball Phantom

The centroid of the cross-section on the TEE images was identified using a least squares best fit ellipse to manually identified points. The centroid of the ball phantom was identified by manually fitting a sphere to the ball surface. The gold standard outline is acquired by selecting a plane through the digitized model where the ultrasound image is deemed to be located, and the centroid of the expected and observed outlines were compared. Results are summarized in Table 4.2 and illustrated in Figure 4.14, and demonstrate slightly higher target registration errors than the point target. This is likely due to errors introduced during the ultrasound centroid selection process, since the ellipsoid-fitting process is sensitive to outliers and speed of sound distortions.

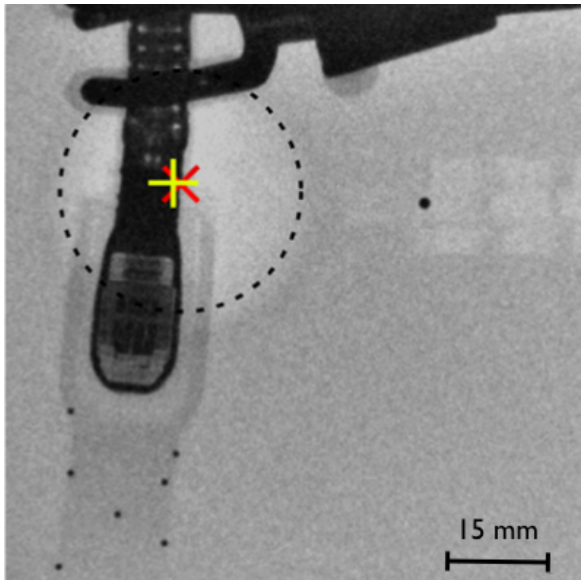

Fig. 4.14: Table Tennis Phantom Result. Yellow - gold standard ball centroid. Red - ball centroid reprojected from TEE.

Table 4.2: Table Tennis Ball Accuracy Results

	N	Mean (mm)	Std Dev (mm)	RMS (mm)
3D TRE	6	3.42	0.62	3.47
2D rTRE	6	2.77	0.98	2.91

Heart Phantom

The registered heart phantom images demonstrated good alignment between the CT-TEE registered model and the fluoroscopy image (Figure 4.15).

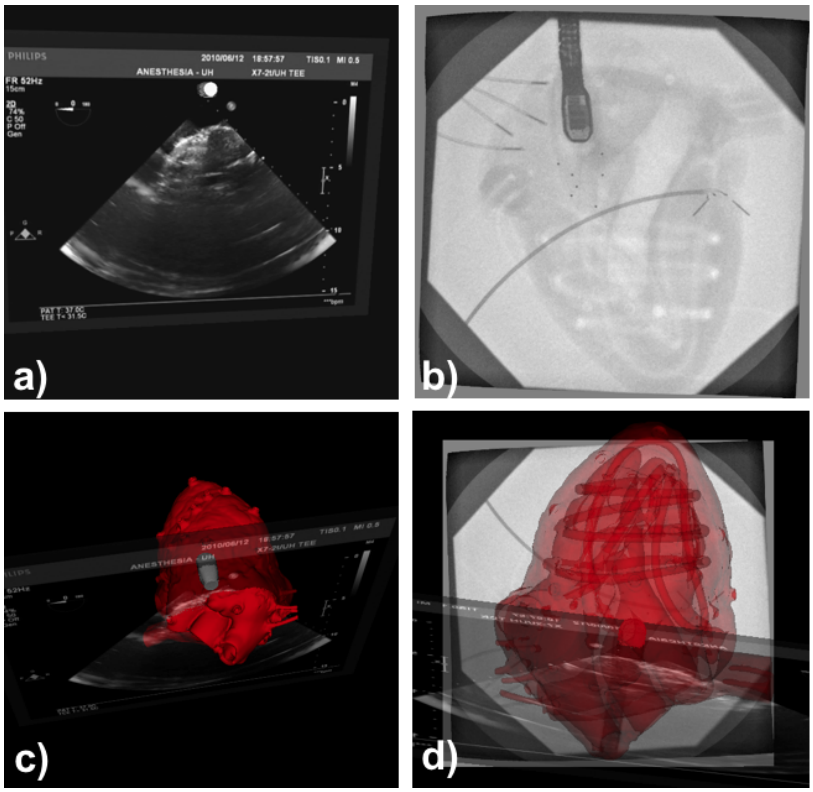

Fig. 4.15: a) TEE Image b) Fluoroscopy Image c) Manual registration of CT to TEE image. d) Registration of TEE and corresponding CT.

4.6.2.2 *Ex vivo* Porcine Images

Ex vivo results are summarized in Table 4.3 and Figure 4.16. Registration accuracy measured on the *ex vivo* specimen was slightly lower than that obtained with the point target phantom. Additional error can be attributed to the difficulty in manual localization of the pin targets in the ultrasound images due to artifacts introduced by the metal pins, and less accurate TEE probe tracking due to lower contrast between the tantalum tracking fiducials and contrast-enhanced cardiac specimen.

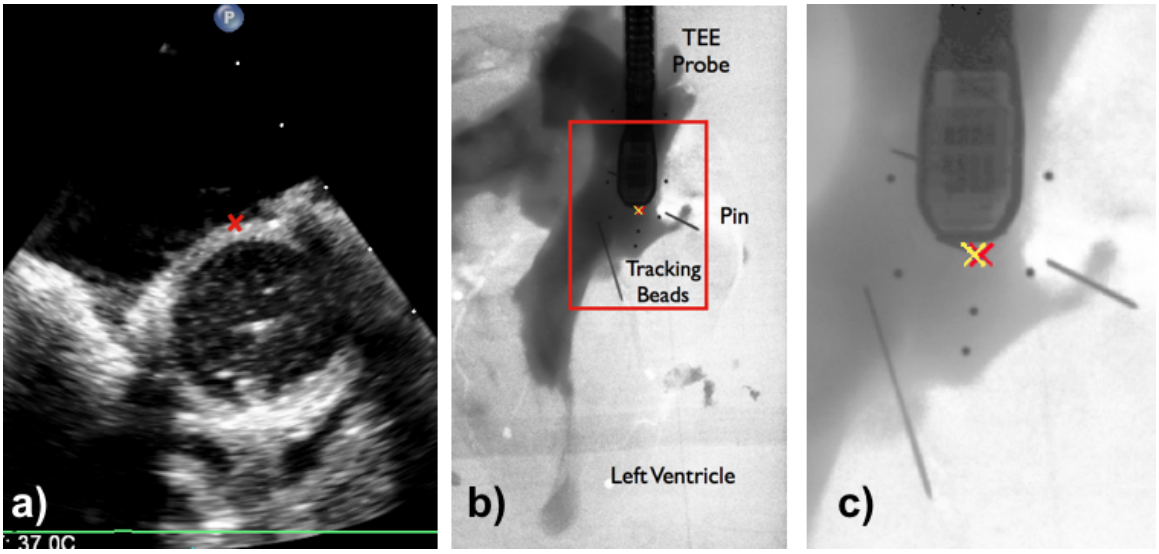

Fig. 4.16: *Ex vivo* accuracy study results. (a) TEE image of the aortic root showing manually segmented pin target. (b) Fluoroscopy image showing pin target, yellow - manual gold standard point, red - reprojected from TEE point in (a). (c) Zoomed-in view of (b).

Table 4.3: *Ex Vivo* 2D reprojection TRE Accuracy Results of the pin targets.

N	Mean (mm)	Std Dev (mm)	RMS (mm)
8	1.20	0.76	1.40

4.6.2.3 *In vivo* Porcine Images

In vivo results are summarized in Table 4.4 and Figure 4.17, and best represent the error likely to be encountered by physicians in a clinical setting. The RMS 2D reprojection error, measured as the shortest distance between each reprojected US point and the fluoroscopy-measured target line, was less than 1.6mm.

Table 4.4: *In Vivo* 2D reprojection TRE Accuracy Results of the guidewire and catheter targets

N	Mean (mm)	Std Dev (mm)	RMS (mm)
1705	1.23	0.91	1.53

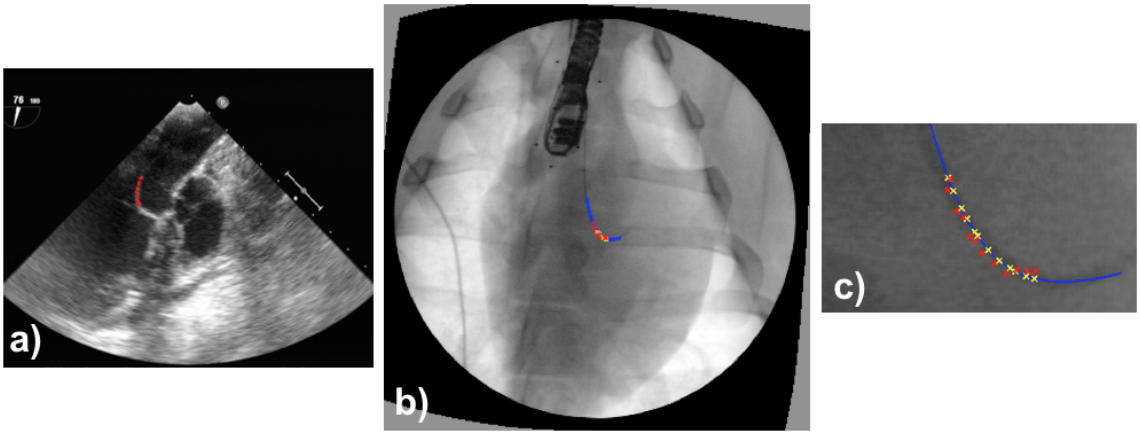

Fig. 4.17: *In vivo* accuracy study results. (a) TEE image of the aortic root showing manually selected points along the target wire. (b) Fluoroscopy image showing target wire (blue) - automatically segmented gold standard wire (red) - reprojected wire points selected from TEE (corresponding to (a)), (yellow) - closest gold standard point corresponding to each TEE point. (c) Zoomed-in view of (b).

4.7 Experiment 2: Tracking Robustness Analysis

Robustness of the tracking algorithm was evaluated on the *in vivo* porcine images used in Section 4.6.1.5, as this best represents the noise, contrast and occlusions present in intraoperative imaging of humans.

4.7.1 Methods

4.7.1.1 Fiducial Initialization and Correspondence Determination

The number and position of fiducials identified by the initialization algorithm was compared to manual initialization, and the ability to successfully determine correspondence between the 2D image and 3D model fiducials was assessed.

4.7.1.2 Fiducial Detection Rate

Poor contrast or overlapping structures in the fluoroscopy image may cause failure to locate fiducial centroids. A reduction in the number of fiducials available for tracking may reduce pose estimation accuracy or result in tracking failure. The number of tracking fiducials successfully measured on each frame was assessed.

4.7.1.3 Tracking Failure

Once successfully initialized, tracking failure may occur if the algorithm fails to successfully project fiducial motion or measure fiducial centroids. Automated tracking 'recovery' was attempted by first examining the registration error associated with each individual marker and discarding the marker with the highest registration error from the registration. If still unsuccessful, the algorithm discarded the failed frame, and attempts to register the following frame. If both of these recovery attempts are unsuccessful, an 'unrecoverable' tracking failure was deemed. The frequency of tracking failures and unrecoverable tracking failures was recorded.

4.7.2 Results

4.7.2.1 Fiducial Initialization

Automatic fiducial detection was used to initialize 8 *in vivo* sequences acquired (5 sequences used for target registration assessment in Section 4.6.1.5, and 3 test sequences in which no target was present in the image). Fiducial locations selected by the initialization algorithm were compared to manual fiducial selection. 73% of the fiducials could be manually initialized (the remainder were occluded by TEE probe structures), and the algorithm was successful in detecting 98% of user identified fiducials. The mean distance between the user selected fiducial points and the automatically selected points was 0.54 mm.

Automatic fiducial correspondence between the 2D image and the 3D model was successfully determined in all sequences using either the automatically detected or manually selected fiducials.

4.7.2.2 Fiducial Detection

Automatic fiducial detection successfully detected 5 or 6 of the tracking fiducials in 97% of the images, but detected all 7 in less than 1% (Table 4.5). The fiducials that were occluded varied depending on the pose of the TEE probe, and were generally obscured by internal probe features rather than external objects. Fiducial occlusion leads to significant decreases in TEE probe localization in the out-of-plane translation and rotational poses.

Table 4.5: *In Vivo* Tracking Fiducial Detection

Number of missed fiducials	0	1	2	3	4
Proportion of images	0.007	0.60	0.37	0.02	0.007

4.7.2.3 Tracking Failure

Once 2D to 3D fiducial correspondence was determined, the unrecoverable tracking failure rate was 0.08%, corresponding to an average of 1 failure that required re-initialization in 3 minutes of fluoroscopy acquisition. Note that typical fluoroscopy acquisitions do not exceed 1 to 2 minutes to minimize radiation doses. The frame tracking failure rate was 16% (pose estimation failed in 202 of 1268 frames), however these failures do not disrupt the registration process since the software performs automatic tracking recovery.

4.8 Visualization Options

Providing intuitive visualization of information taken from registered TEE and fluoroscopy images is a challenging problem. Currently two options exist (Figure 7.1):

1. An **'overlay'** image of the TEE projected onto the fluoroscopy image
2. A fluoroscopy image with the marked positions of anatomical features measured on TEE, which can be denoted a **'feature-enhanced'** view.

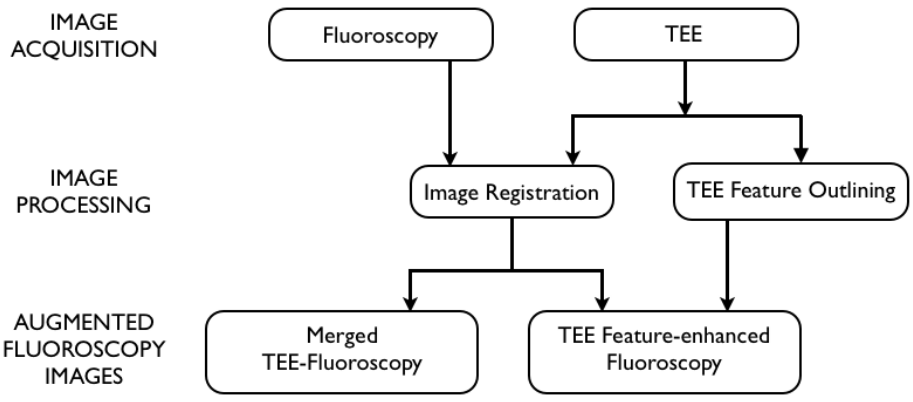

Fig. 4.18: Construction of 'Overlay' and 'Feature-enhanced' images.

The 'overlay' images may be more difficult to visualize clearly when the TEE and fluoroscopy imaging planes are close to being mutually perpendicular (Figure 4.19).

Manipulation of opacity and colour requires further investigation to maximize highlighting of salient features.

In Kempfert *et al.* [11] and Karar *et al.* [12], anatomical information taken from DynaCT is used perioperatively to outline features of interest on the fluoroscopy image. Similarly, in the 'feature-enhanced' view (Figure 4.20), anatomical features such as the virtual basal ring plane and sinutubular junction plane, can be identified perioperatively by US and delineated on the corresponding fluoroscopy image. The selection of these features may be performed manually peri-operatively, or automatically (the development of automated feature selection algorithms are further discussed in Chapter 6). Manual feature extraction does not allow for real-time update, however automatic feature extraction may introduce additional error.

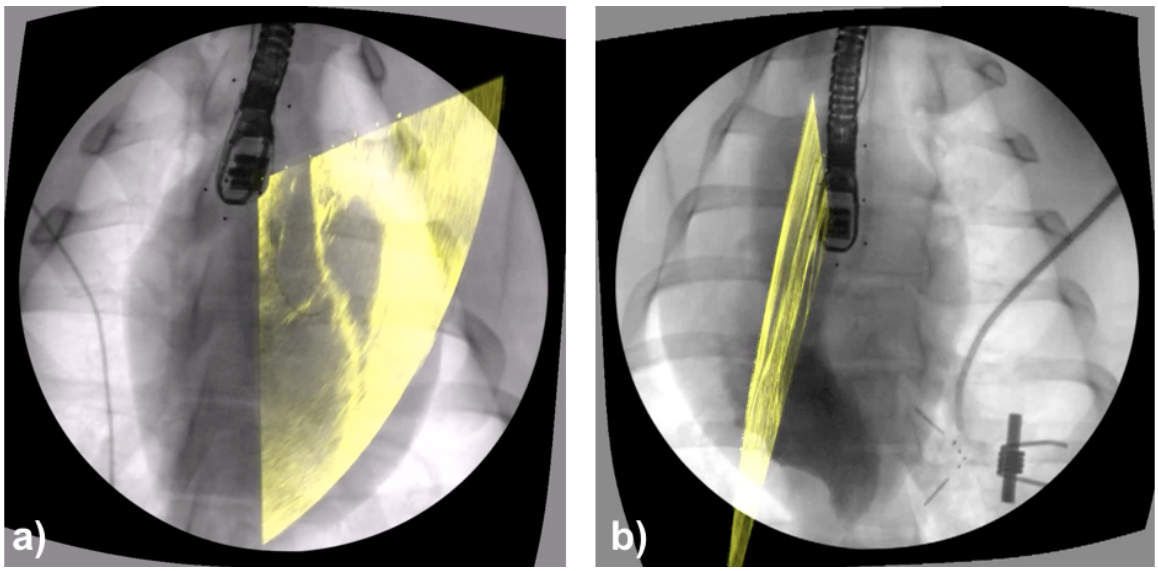

Fig. 4.19: Overlay of TEE and fluoroscopy images where the imaging planes are: (a) approximately 45° apart and (b) approximately perpendicular.

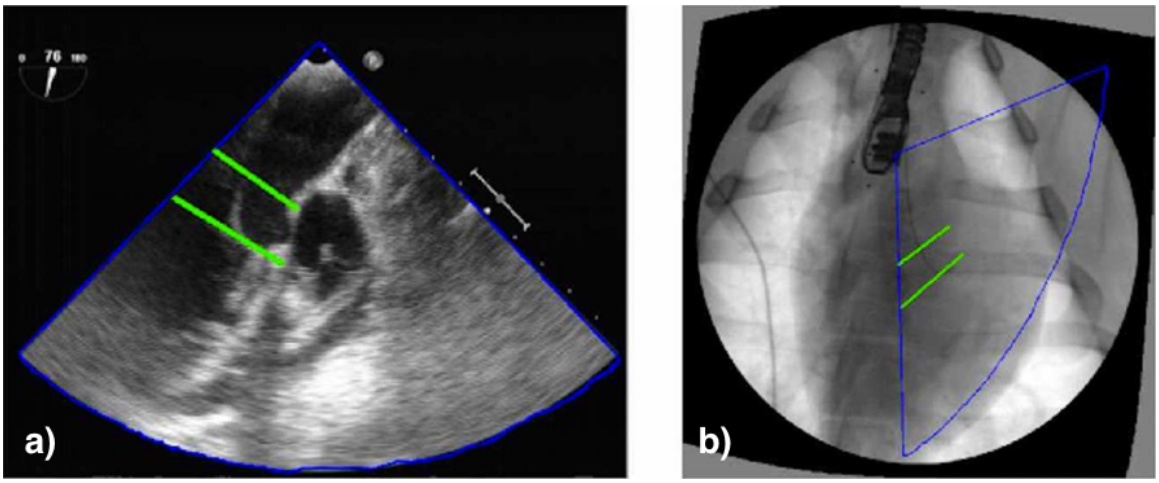

Fig. 4.20: (a) Ultrasound image of a porcine subject with the virtual basal ring plane and sinutubular junction plane marked (green). (b) Fluoroscopy image showing re-projection of the US plane (blue) and anatomical planes (green) corresponding to (a).

4.9 Proposed TAVI Workflow

The proposed TAVI workflow is shown in Figure 4.21. Contrast aortography can be used optionally to confirm placement before final deployment. The image calibration processes are designed to occur entirely pre-operatively, to minimize time costs associated with the augmented imaging system. Repeated TEE calibrations demonstrate stability in the calibration matrix over time, with the fluoroscopy fiducials being reasonably rigidly attached to the probe matrix. Fluoroscopy imaging views are selected based upon the pre-operative CT scan, and calibration parameters for the flat-panel detectors can be selected from a look-up table. Further study is warranted to examine the effects of interpolation and positioning precision of the C-arm, but initial results suggests minimal decreases in accuracy.

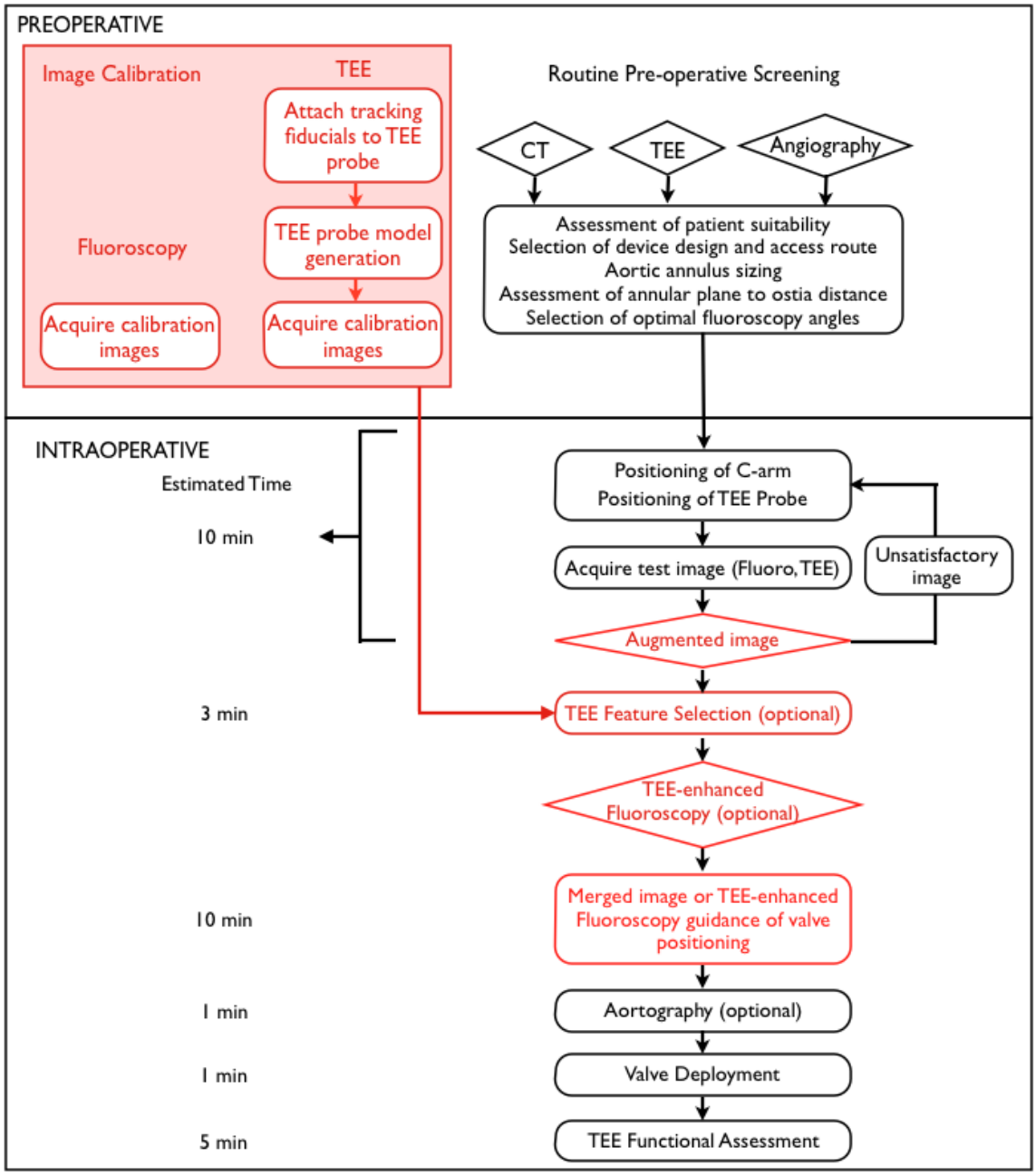

Fig. 4.21: Proposed TAVI workflow for providing visualization of registered TEE and Fluoroscopy images. Modifications to the regular workflow required to provide augmenting imaging are shown in red.

4.10 Discussion

The *in-vivo* overall registration accuracy studies include all sources of error, including TEE probe and patient motion, and demonstrate that TEE and fluoroscopy images can be successfully registered with an in-plane RMS error of 1.5 mm. This accuracy is a 50% improvement over the only 2 previous attempts to register TEE and fluoroscopy images using magnetic and biplane fluoroscopy tracking, which reported accuracies of 3-5 mm [13, 3]. This improvement in accuracy is clinically significant in the TAVI procedure, where the physician must position a stent across the valve without occluding the coronary ostia, which may be less than 10 mm away.

The TEE localization and tracking accuracy studies, and the point target study demonstrate that the 3D error is significantly greater than the 2D error, which is consistent with previous work [14]. Error in the out-of-plane direction is not clinically significant, as anatomical information taken from the US image is re-projected onto the 2D fluoroscopy image, and the motion of tools is constrained by the aortic root in the out-of-plane direction. In the guidance of TAVI procedures, we are primarily interested in the direction along the aortic root axis, as this helps clinicians guide placement of the valve in the appropriate proportions.

Registration accuracy is primarily affected by errors introduced in TEE probe tracking and in US calibration. A fiducial localization error of 2.33mm during US calibration suggests a relatively large contribution of error from this source. Many alternative techniques for calibration of a 2D US probe have been proposed in the last decade [15], but all demonstrate similar accuracy. Recent work has focused on the use of 3D volumes to calibrate TEE probes capable of 3D imaging, and these may demonstrate improved results [16].

This tracking technique demonstrated good robustness, with tracking failure uncommon. Sufficient fiducials are visible in the initial image for automatic point correspondence in the majority of cases (97%). Although tracking failure may occur, the algorithm can recover by discarded the failed frame 99% of the time, and the variance in registration error is small (<0.8mm). Unlike intensity-based implementations of image-based tracking, this algorithm will not converge to a local minima

solution as long as the fiducials are correctly identified. Convergence to local minima may cause unexpected peaks in error, and if undetected these could potentially be catastrophic in TAVI or other medical applications. Also, in contrast to the limited working volume of magnetic tracking systems [3], accuracy is not directly affected by spatial positioning of the TEE probe.

This system is capable of providing live real-time image registration and overlay at 20 frames per second. In this study, the images were processed from a file stream to simulate real-time capture and processing. Each frame requires only 0.05s to process entirely, which is less than the time between acquisition of fluoroscopy frames in this procedure (0.067s at 15Hz). Since the processing speed exceeds the image capture rate, there is no expected loss of accuracy in a live guidance system compared to our results. The next step in this work will be to implement this system with live streaming of fluoroscopy and ultrasound images. This system can be used both peri-operatively for procedure planning, and intra-procedurally to guide stent deployment.

4.11 Chapter Summary

In this chapter, a method for registering TEE and fluoroscopy images together using fiducial-based TEE probe pose estimation is presented. This system is suitable for clinical use, with a clinically acceptable (as defined in Chapter 2) 2D RMS accuracy of approximately 1.5 mm, good robustness allowing acquisitions of several minutes without tracking failure, fully automated TEE probe tracking initialization, a TAVI workflow that does not require any significant OR setup or additional intra-operative time, and the capability for real-time registration and display.

In addition to being an intermediate step in real-time CT-fluoroscopy registration, TEE-fluoroscopy registration can provide important anatomical information that can be used both peri-operatively and during stent deployment.

References

[1] Gobbi DG, Comeau RM, Peters TM. Ultrasound Probe Tracking for Real-Time Ultrasound/MRI Overlay and Visualization of Brain Shift. In: MICCAI; 1999. p. 920–927.

[2] Schonemann PH. A generalized solution of the orthogonal procrustes problem. Psychometrika. 1966;31(1):1–10.

[3] Jain A, Gutierrez L, Stanton D. 3D TEE Registration with X-Ray Fluoroscopy for Interventional Cardiac Applications. In: FIMH. vol. 5528; 2009. p. 321–329.

[4] Pagoulatos N, Haynor DR, Kim Y. A fast calibration method for 3-D tracking of ultrasound images using a spatial localizer. Ultrasound in Medicine and Biology. 2001;27(9):1219–1229.

[5] Hsu PW, Prager RW, Gee AH, Treece GM. Real-Time Freehand 3D Ultrasound Calibration. Ultrasound in Medicine and Biology. 2008;34(2):239–251.

[6] Pilu, Maurizio. Direct method for stereo correspondence based on singular value decomposition; 1997. p. 261–266.

[7] Sharp GS, Jiang SB, Shimizu S, Shirato H. Prediction of respiratory tumour motion for real-time image-guided radiotherapy. Physics in Medicine and Biology. 2004;49(3):425–440.

[8] Di Stefano L, Bulgarelli A. A simple and efficient connected components labeling algorithm. In: 10th International Conference on Image Analysis and Processing; 1999. .

[9] Kimme C, Ballard D, Sklansky J. Finding circles by an array of accumulators. Communications of the ACM. 1975;18(2):120–122.

[10] Wang MY, Maurer Jr CR, Fitzpatrick JM, Maciunas RJ. An automatic technique for finding and localizing externally attached markers in CT and MR volume im-

ages of the head. IEEE Transactions on Biomedical Engineering. 1996;43(6):627–637.

[11] Kempfert J, Rastan AJ, Noettling A, Blumenstein J, Linke A, Schule FW r G Mohr, et al. Perioperative DynaCT for Improved Imaging During Transapical Aortic Valve Implantation [AHA Meeting Abstract]. Circulation. 2010 Nov;122(21S).

[12] Karar ME, Gessat M, Walther T, Falk V, Burgert O. Towards a new image guidance system for assisting transapical minimally invasive aortic valve implantation. Conference proceedings :Annual International Conference of the IEEE Engineering in Medicine and Biology Society IEEE Engineering in Medicine and Biology Society Conference. 2009;2009:3645–3648.

[13] Gao G, Penney G, Gogin N, Cathier P, Arujuna A, Wright M, et al. Rapid Image Registration of Three-Dimensional Transesophageal Echocardiography and X-ray Fluoroscopy for the Guidance of Cardiac Interventions. In: Lecture Notes in Computer Science: Information Processing in Computer-Assisted Interventions. vol. 6135; 2010. p. 124–134.

[14] Habets DF, Pollmann SI, Yuan X, Peters TM, Holdsworth DW. Error analysis of marker-based object localization using a single-plane XRII. Medical Physics. 2009;36(1):190–200.

[15] Mercier L, Lang T, Lindseth F, Collins DL. A review of calibration techniques for freehand 3-D ultrasound systems. Ultrasound in Medicine and Biology. 2005 April;31(4):449–471.

[16] Huang X, Gutirrez LF, Stanton D, Kim PCW, Jain A. Image Registration Based 3D TEE-EM Calibration. Proceedings of ISBI: Biomedical Imaging: From Nano to Macro, 2010 IEEE International Symposium on. 2010;p. 1209–1212.

Chapter 5

Surface-based CT-TEE Registration

In this chapter, a method for registering TEE and CT together using a surface-based registration is presented. The use of different methods to select TEE surface points - including XPlane TEE images, tracked and reconstructed multiple TEE planes and 3D TEE surface extraction - are compared. A rapid initialization method is proposed and registration performance is assessed on *ex vivo* porcine and human images.

5.1 Registration Methodology

The aortic root is assumed to be a rigid body throughout the cardiac cycle, a reasonable assumption in this patient population, as the more fibrosed tissue and heavy calcification does not allow significant deformation between systole and diastole.

5.1.1 CT Surface Extraction

A surface mesh of the aortic root is generated from the pre-operative CT using edge-based snakes in the open source software ITK-SNAP (http://www.itksnap.org) [1] with simple thresholding pre-processing. The segmentation is initialized by two

operator-selected points defining an approximate central axis. One point is taken at the level of the sinutubular junction, and one point approximately 2cm above the sinutubular junction. The same points can be used for registration initialization (Section 5.1.3.1).

The resultant surface mesh (Figure 5.1a) is checked by the operator once segmentation is complete, and minor manual adjustments may be required to prevent 'leakage' through the aortic valve into the left ventricular outflow tract. This process takes approximately 5 to 10 minutes, and can be performed several days prior to surgery.

5.1.2 TEE Surface Extraction

A number of options exist for the selection of aortic root surface points from the TEE image:

1. **XPlane images (Figure 5.1b):** The Philips iE33 ultrasound machine is capable of acquiring two orthogonal planes simultaneously, providing points on two planes in a single image acquisition, without need for TEE probe tracking and cardiac gating. Since a very sparse set of points is acquired, outlining can be achieved relatively quickly. The outline does not need to be complete, and regions of the image containing artifact can be excluded.
2. **Multiple single plane images reconstructed (Figure 5.1c):** Multiple single planes images acquired with spatial tracking of the TEE probe can be reconstructed to create a larger set of points distributed in 3D space. However, error is introduced by the tracking and cardiac motion. In this chapter, the TEE pose estimation used in Chapter 4 is used for spatial tracking.
3. **Multiple planes extracted from a 3D TEE volume (Figure 5.1d):** Contours are extracted on slices 3mm apart taken from the 3D TEE image, creating a larger set of points evenly distributed in 3D while excluding areas of uncertainty or artifact on the TEE image. Due to the size and position of the aortic root, two stitched volumes were required to image the aortic root fully, a process that may introduce significant motion artifact into the volume. Since 5-6 slices

are used, the amount of user interaction required is approximately double that required for the XPlane images. Low resolution of the 3D TEE may also affect accuracy.

4. **A 3D TEE surface (Figure 5.1e):** A 3D surface can be segmented from the same 3D TEE images as Option 3. This option utilizes a much larger point set than is required in the previous options, and that is fully distributed across 3D space. Again, the low resolution of the 3D images makes it difficult to achieve an accurate segmentation, and areas significantly affected by artifact cannot be excluded unless they are specifically identified and cropped from the mesh (none of the meshes used in this study were cropped).

TEE surface options 1 and 2 are explored in Experiment 1 (Section 5.2), and options 1, 3 and 4 are explored in Experiment 2 (Section 5.3).

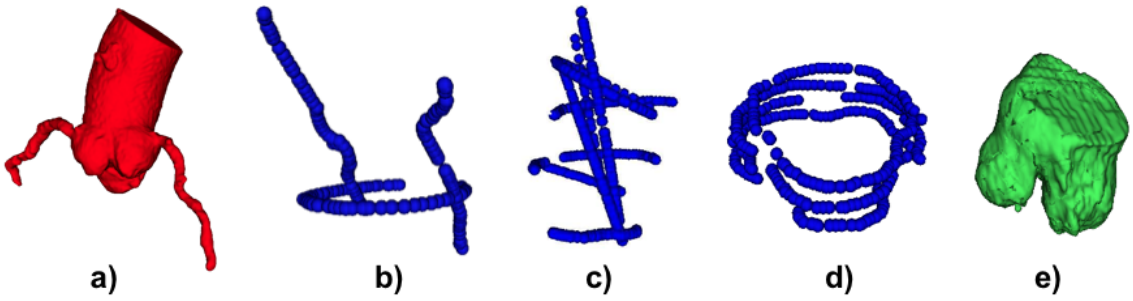

Fig. 5.1: Aortic root surfaces selected from (a) the CT, (b) XPlane TEE images, (c) multiple reconstructed single plane TEE images, (d) sparse set of planes from the 3D TEE and (e) 3D TEE surface.

5.1.3 Iterative Closest Point Registration

The iterative closes point (ICP) registration algorithm [2] was chosen to allow for real-time registration. The workflow of the algorithm is as follows:

1. Points are associated by nearest neighbour criteria;
2. Transformation parameters are estimated using a mean square cost function;
3. Points are transformed using the estimated parameters;

4. Steps 1-3 are iterated until convergence criteria are met.

5.1.3.1 Registration Initialization

A pose estimate is required to initialize the ICP registration. This estimate is determined by:

1. Alignment of the central axis of the aortic root (Figure 5.2 a,b)
    - **CT Axis** was selected manually pre-operatively during surface mesh generation by selecting a point at the coaptation point of the three leaflets, and a point 2-3cm above the coaptation point.
    - **TEE Axis** was assumed to be perpendicular to the short axis view, passing through the centroid of the short axis segmentation.
2. Alignment of the non-coronary cusp (NCC) direction to constrain rotation around the central axis (Figure 5.2 c)
    - **CT NCC** direction was selected manually pre-operatively during surface mesh generation.
    - **TEE NCC** direction was assumed to appear at roughly 270° in the short axis view (or directly below the centroid point).

This initialization process assumes that the patient is lying supine with the TEE transducer in the esophagus, and allows for all required TEE parameters to be determined automatically. When combined with automatic TEE contour selection (described in Chapter 6) this allows for a fully automated registration process.

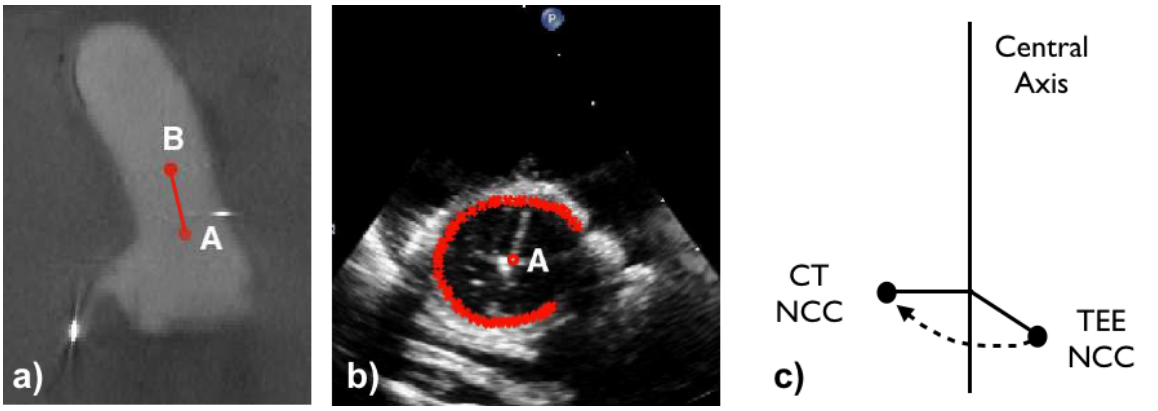

Fig. 5.2: ICP Initialization. (a) Selection of the central axis in CT. (b) Selection of the central axis in TEE. (c) Alignment of the non-coronary cusp measured in the CT image and the TEE image.

5.2 Experiment 1: CT Contour - CT Surface Registration

5.2.1 Introduction

The number of points and planes required to constrain an ICP registration of sparse data to a surface depends heavily on the object geometry. Using a sparse set of TEE planes provides advantages, such as a larger field of view, real-time imaging and a higher frame rate. However, sampling too few planes may not provide enough geometry to constrain the registration to the correct solution, particularly in objects that are highly symmetrical.

In this study, contours on sparse sets of planes were extracted from a CT surface of the aortic root, and registered back to the same CT surface. This registration represents a theoretical maximum achievable accuracy using a sparse set of planes for registration. Contour sets spanning one, two, three, or four planes were explored, and these results are later compared to the TEE-CT registration results for the same patient, obtained in the experiments described in Sections 5.3 and 5.4.

5.2.2 Methods and Materials

5.2.2.1 Contour Selection

A pre-operative CT image was collected from a patient undergoing a TAVI aortic valve replacement at Western University in a protocol approved by the Office of Research Ethics, Western University.

Fifteen short-axis and fifteen long-axis slices through the aortic root were manually selected by an expert, corresponding to image views reasonably obtained during TEE imaging, and covering a maximum range of imaging angles, as shown in Figure 5.3.

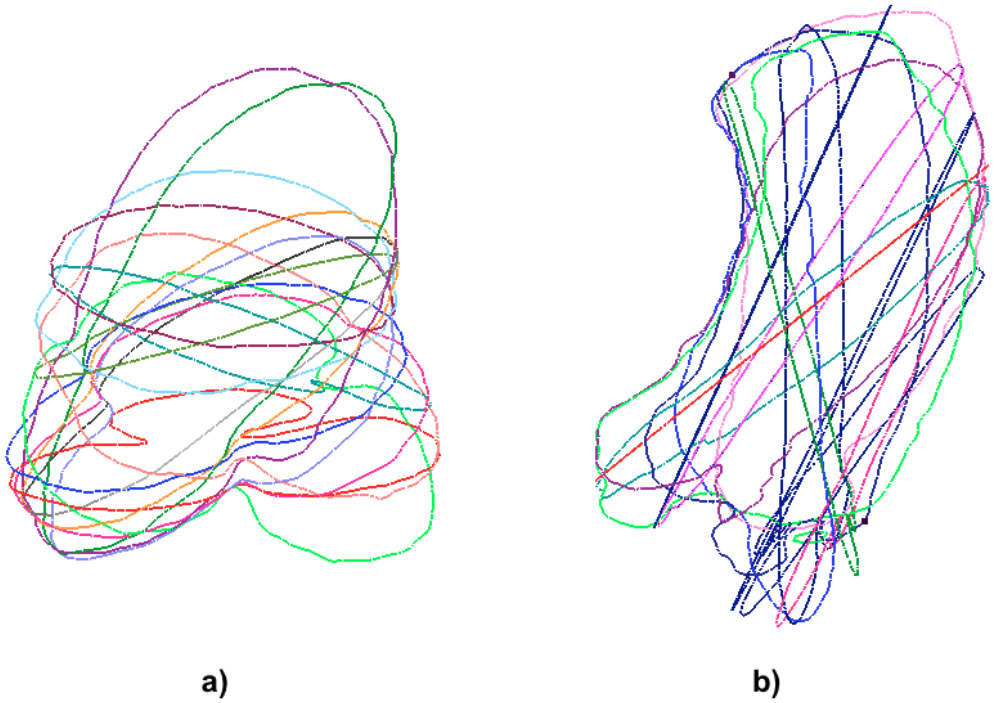

Fig. 5.3: Fifteen short-axis (a) and fifteen long-axis (b) contours were selected for use in this study.

Slices were randomly selected from the short-axis and long-axis sets in the following configurations:

1. **One plane:** *either* a short-axis *or* a long-axis contour
2. **Two planes:** one short-axis *and* one long-axis contour

3. **Three planes:** one short-axis and two long-axis contour *or* two short-axis and one long-axis contour
4. **Four planes:** two short-axis *and* two long-axis contours

5000 contour sets of each configuration were registered to the CT surface. Registration accuracy was assessed using a target registration error (TRE) measure [3]. The left and right coronary ostia, as identified on the CT image, were used as targets.

5.2.2.2 Initialization Registration

The ICP registration was initialized using a randomly selected initialization transformation generated using:

1. A rotation corresponding to a perturbation of up to 40° in any direction around the centre of mass of the contours
2. A translation of up to 5mm in each direction (maximum of 8.66 mm)

5.2.3 Results

Registration results are shown in Figures 5.4 – 5.7. A registration was deemed a 'success' if the resultant TRE was less than 5mm (corresponding to the 'clinically acceptable' error as described in Chapter 2).

The TRE demonstrated no correlation with the initialization position or the specific contours selected, but increased with larger initialization angle offsets. A marked decrease in TRE is demonstrated as additional planes are added. In addition, a capture range corresponding to a 95% registration success rate decreased as the number of planes used increased (Table 5.1, Figure 5.4, Figure 5.7).

A single plane contained insufficient geometry to constrain the registration regardless of initialization position. Two planes demonstrated a capture range of 22.3°, covering the majority of likely initialization positions based on the methodology in this study.

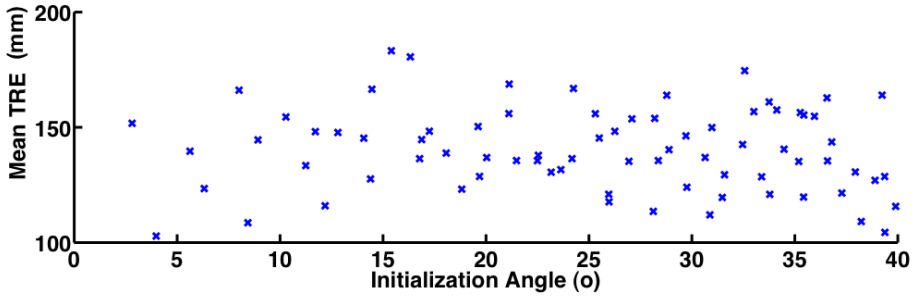

(a)

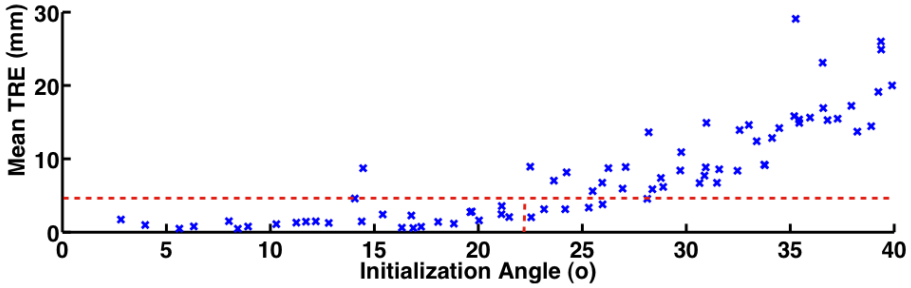

(b)

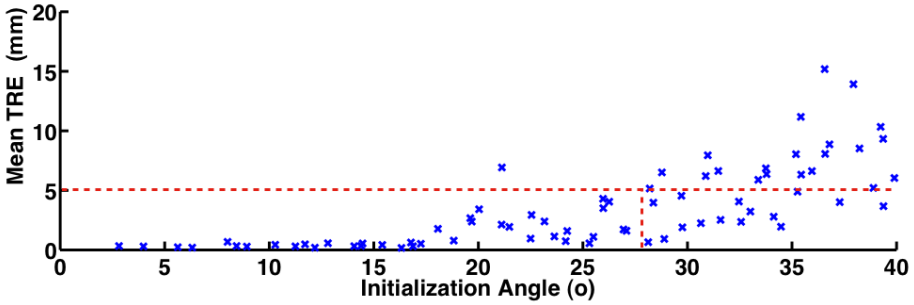

(c)

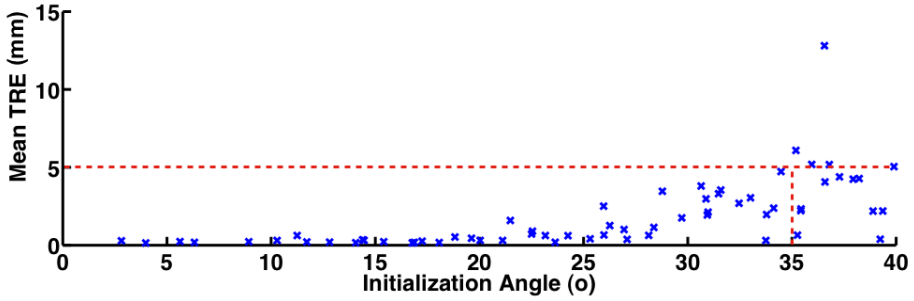

(d)

Fig. 5.4: TRE as a function of initialization angle. The clinically acceptable range of initialization angles is shown. The dashed red line denotes the initialization angle range corresponding to a registration success rate of 95%, where the registration is defined as clinically 'successful' if the TRE is 5mm or below. (a) Single plane. (b) Two planes. (c) Three planes. (d) Four planes.

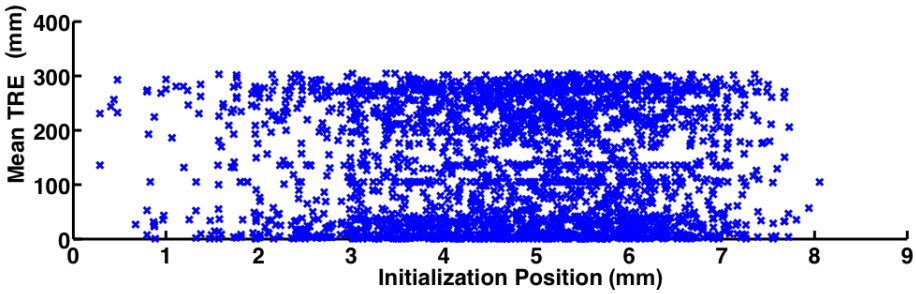

(a)

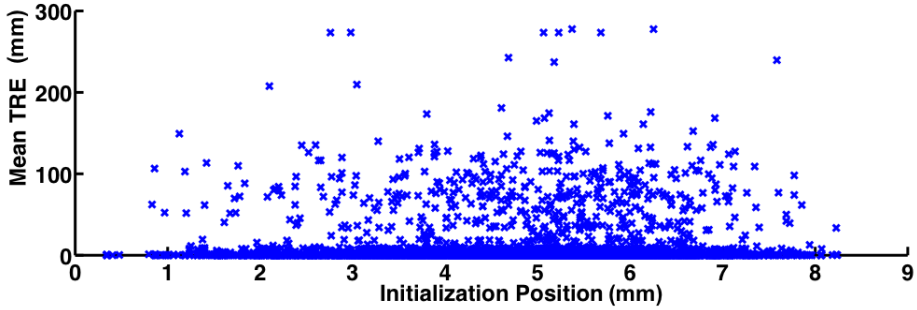

(b)

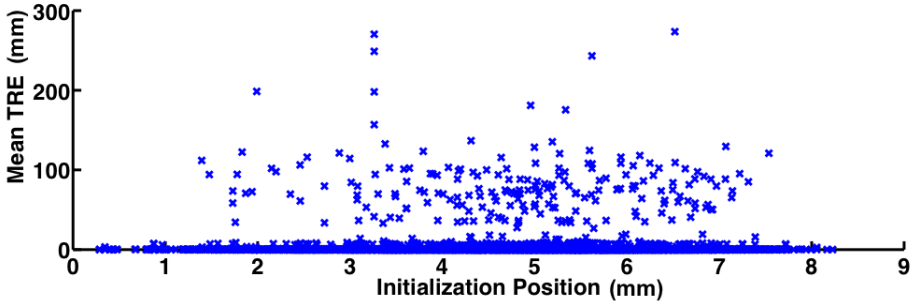

(c)

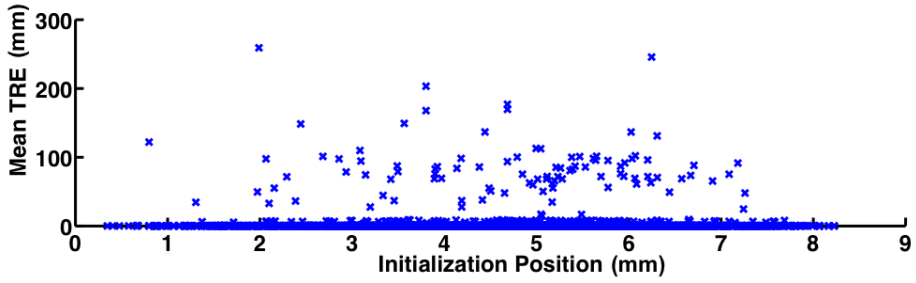

(d)

Fig. 5.5: TRE as a function of initialization position. (a) Single plane. (b) Two planes. (c) Three planes. (d) Four planes.

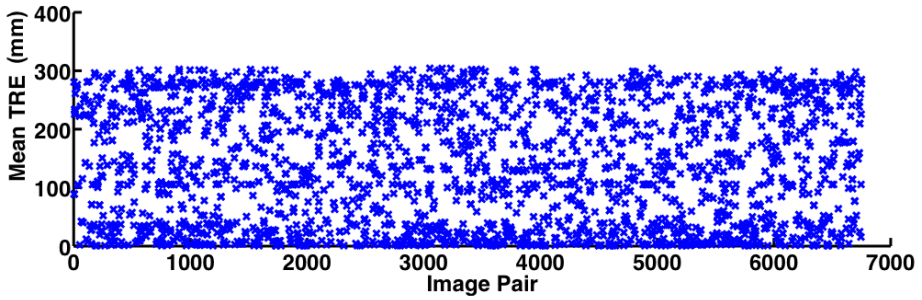

(a)

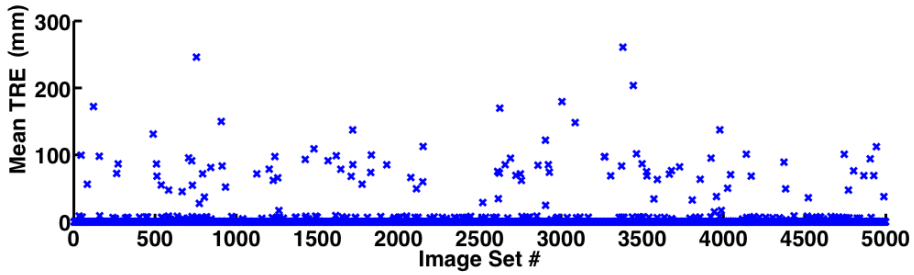

(b)

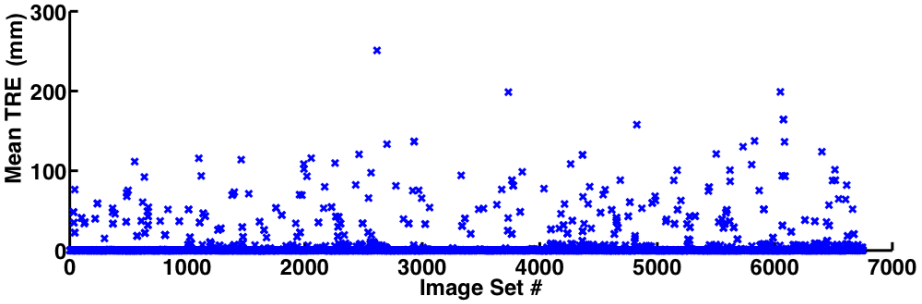

(c)

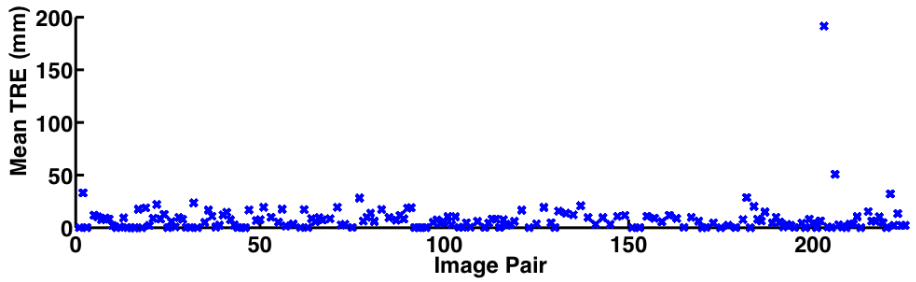

(d)

Fig. 5.6: TRE as a function of contour set. (a) Single plane. (b) Two planes. (c) Three planes. (d) Four planes.

Table 5.1: Capture ranges corresponding to a 95% registration success rate.

Number of planes used	Capture Range (degrees)
2	22.3
3	27.8
4	35.0

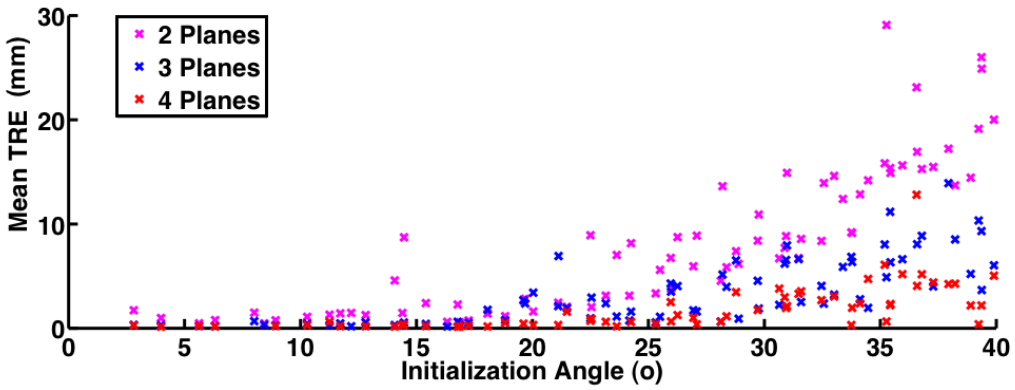

Fig. 5.7: TRE as a function of initialization angle, showing sets of two, three and four planes.

5.2.4 Discussion

This study demonstrates that the aortic root has sufficient geometry to allow very sparse contours to accurately constrain the registration, despite being highly symmetrical. While contours on a single plane fail to converge to a correct solution, contours on two planes demonstrate reasonable accuracy within the clinically acceptable range. However, results also demonstrate that a substantial amount of registration error (up to 5 mm) is present when using two planes, even under idealized conditions, and this error represents a theoretical minimum error associated with the geometry of the aortic root. Imaging artifacts, speed of sound distortions and limited lateral and axial resolution further reduce accuracy when registering to TEE images. Results suggest a trade-off between a lack of adequate geometry for registration when using XPlane

images and lower resolution and motion artifacts with 3D live volume imaging or reconstructed tracked images, and this is further explored in Sections 5.3 and 5.4.

The analysis in this study was performed using the CT model from a single patient, and results may vary from patient to patient depending on aortic root geometry. Further studies may consider repeating this analysis using multiple patients or an 'average' patient model.

5.3 Experiment 2: Assessment of registration performance on an *ex vivo* porcine subject

In this study, XPlane TEE images and reconstructed single plane TEE images of an *ex vivo* porcine heart were registered to a CT-derived surface of the aortic root. The results of the XPlane TEE to CT registration were combined with the TEE-fluoroscopy registration described in Chapter 4 to register the CT to fluoroscopy, with the transformations used shown in Figure 5.8, and registration accuracy was assessed.

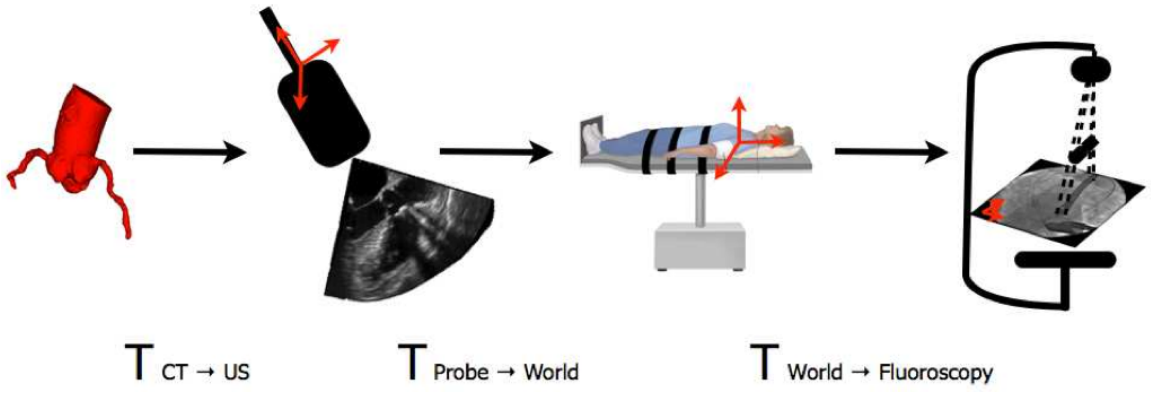

Fig. 5.8: Steps in the registration of a CT-derived surface to the fluoroscopy image.

5.3.1 Methods

5.3.1.1 Equipment and Materials

The *ex vivo* porcine heart containing 5 pin targets described in Section 4.6.1.4 was imaged using TEE, CT and fluoroscopy.

Fluoroscopy and CT images were acquired on a Medtronic O-arm Surgical Imaging System^{TM}. The cone-beam CT was acquired at a voxel spacing of $0.41mm \times 0.41mm \times 0.83mm$, dimensions of $512 \times 512 \times 192$ voxels, 120kVp, and 25mA. Fluoroscopy images were acquired with an isotropic pixel spacing of 0.39mm, at 58kVp and 23mA with a 4ms exposure. XPlane and single plane TEE images were acquired using a Philips iE33 US machine with an X7-2t probe (operating frequency of 7 to 2 MHz) at a frame rate of 36 or 52Hz and an imaging depth of 7-10cm.

XPlane Images

Five Xplane images showing both short-axis and long-axis views were acquired in different positions covering a spectrum of images likely to be acquired in a clinical scenario. These images were registered to the CT surface mesh. Two images that did not contain a clearly visible target were not used.

Reconstructed points from multiple single plane images

Eight single plane US images were acquired simultaneously with a fluoroscopy image (to provide spatial tracking information). Two images that did not contain a clearly visible target were not used. The tracking information was used to reconstruct manually identified points taken from multiple US images into a common coordinate system. These points were then registered to the CT surface mesh. Images that did not contain a clearly visible target were not used. Targets were identified manually on both CT and US.

Accuracy Assessment

Accuracy of the CT-TEE and CT-fluoroscopy registrations were assessed using:

1. A mean point-to-surface distance measured between the TEE contours and CT

surface after ICP registration *(CT-TEE registration only)*;

2. A target registration error (TRE) using five pins inserted into the aortic root as targets *(CT-TEE and CT-fluoroscopy registration)*.

5.3.2 Results

5.3.2.1 Target localization

Targets were manually identified on all images. The standard deviation of the measured locations (determined from 10 repeated measurements for each target) were 0.41 mm, 0.40 mm and 0.23 mm for the CT, TEE and fluoroscopy images respectively. This error contributes partially to the measured target registration error.

5.3.2.2 CT-TEE Registration

XPlane Images

The 165 US points identified on two planes were registered to the CT derived surface mesh, resulting in XPlane US to CT registration as shown in Figure 5.9a and b, which demonstrates good alignment of the US identified points with the segmented CT surface as shown in Figure 5.9a) and Figure 5.9b). Figure 5.9c) shows a slice through the CT mesh overlaid on its corresponding US image to visually highlight the registration error. The mean point-to-surface error and target registration error were 1.48 and 5.00mm respectively. The registrations took an average of 0.44 seconds to run on a 2.66GHz Intel Core 2 Duo processor with 4GB of memory.

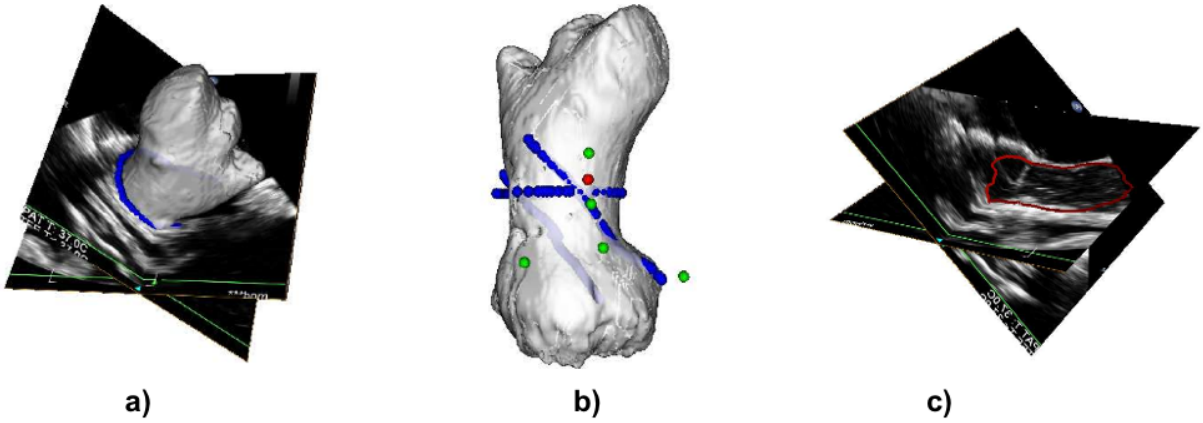

Fig. 5.9: (a) Registered CT surface mesh shown overlaid onto the reconstructed US image and manually identified US points (blue). (b) US Points (blue) registered to the CT surface mesh shown with CT (green) and US (red) identified targets. (c) US image shown with corresponding CT contour (red) after registration.

Reconstructed points from multiple single plane images

The 338 US points identified on 6 planes were registered to the CT model. Results of the reconstructed US to CT registration are shown in Figure 5.10 and Table 5.2. The target locations measured using tracked TEE have a standard deviation of 0.89mm, reflecting the error introduced in the manual target selection process combined with TEE probe tracking error (Figure 5.10). There is good alignment of targets identified in CT and US (Figure 5.10b), with an RMS TRE of 2.64mm. The registrations took 0.46 seconds to run on a 2.66GHz Intel Core 2 Duo processor with 4GB of memory.

Table 5.2: Reconstructed US to CT surface registration error

	Point to Surface Distance (mm) N = 338	TRE (mm) N = 6
Mean	2.12	2.48
Deviation	0.78	0.99
RMS	2.31	2.64

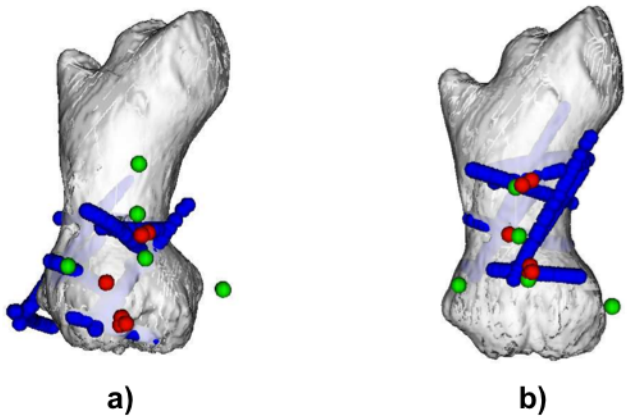

Fig. 5.10: (a) Pose at initialization (b) Registration output showing registered US points (blue) and CT mesh. Targets identified from CT (green), and US (red) are shown. The slight mis-alignment of the same target identified on multiple TEE images reflects manual segmentation and TEE tracking error.

5.3.2.3 CT-Fluoroscopy Registration

Targets identified on TEE were re-projected onto the fluoroscopy image and compared to the manual gold standard targets identified from fluoroscopy. Magnification correction was applied to the distance measurements to correct for perspective, using the height of the TEE probe (as measured using fiducial-based TEE pose estimation) as an estimate of the target distance from fluoroscopy detector. The targets demonstrated good correspondence as shown in Figure 5.11. The RMS target registration error was 5.50 mm.

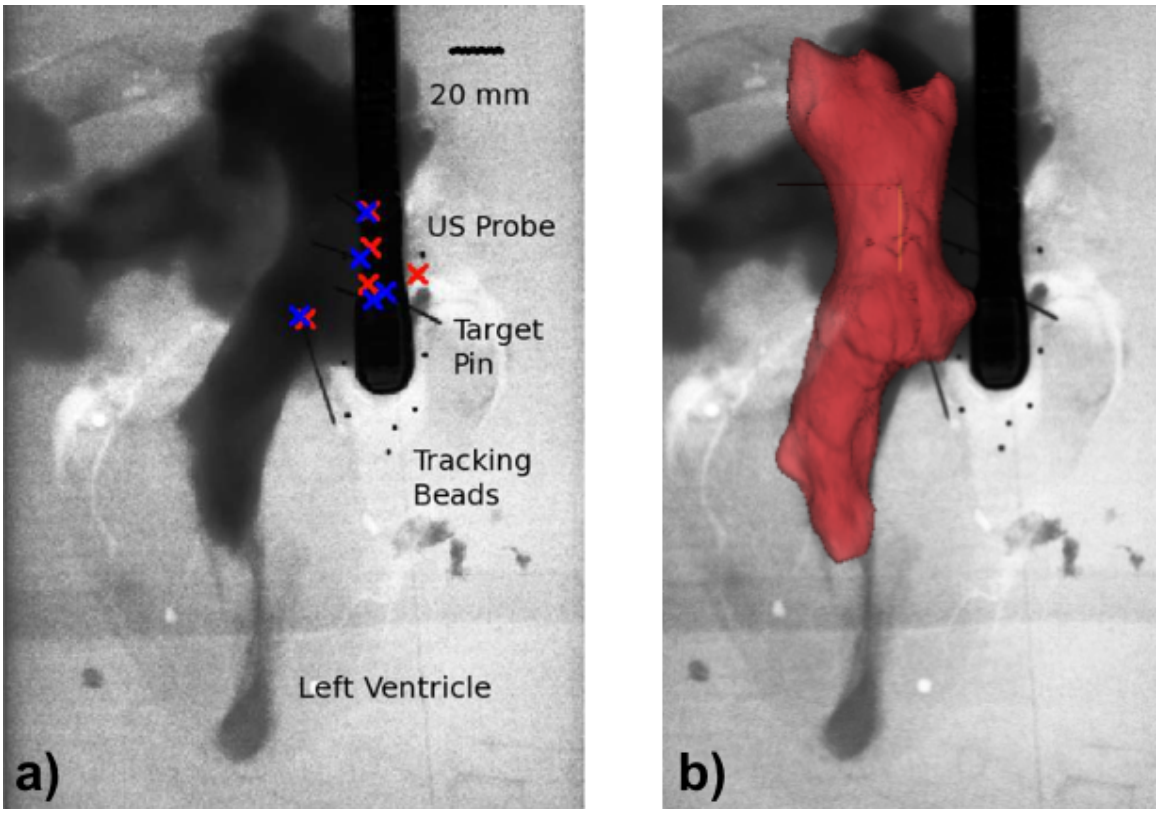

Fig. 5.11: (a) CT-Fluoroscopy registration results. Red - Pin targets identified manually in the fluoroscopy image. Blue - Pin targets identified in the CT image, reprojected onto the fluoroscopy image. (b) Overlay of CT surface (aortic root and left ventricular outflow tract) onto the fluoroscopy image.

5.3.3 Discussion

The results of this study represent the accuracy of a CT-TEE registration of an aortic root without shadow artifacts (healthy porcine subjects do not have calcified aortic roots) or motion error. Results demonstrated clinically acceptable TRE for both TEE-CT and CT-fluoroscopy registration.

Points reconstructed from multiple imaging planes demonstrate an accuracy 2X greater than XPlane imaging, which is consistent with results from Section 5.2. While additional planes help improve accuracy, the use of continuous TEE probe tracking complicates the procedure. Furthermore, time is required for multiple TEE images to

be acquired, which does not allow for real-time registration and visualization. Results suggest that in many cases, XPlane imaging alone may demonstrate sufficient clinical accuracy.

XPlane TEE images demonstrate a TRE approximately 2X greater than that measured using simulated XPlane CT contours in Section 5.2, indicating that both lack of an adequate number of contours and inaccuracies introduced in the TEE imaging process are equally responsible for resultant error.

Significant error was attributed with target localization in both CT (limited by CT resolution) and TEE images (limited by TEE resolution and the presence of reverberation artifacts). The registration error measured in this experiment was likely over-estimated due to the difficulty in localizing pin targets, and better results are expected with anatomical targets, as used in Section 5.4.

5.4 Experiment 3: Comparison of three methods of TEE surface point selection for TEE - CT registration

In this study, accuracy and initialization sensitivity of the methods described in Section 5.1 were assessed on clinical aortic root images. Three methods of selecting TEE surface points for TEE-CT registration (described in Section 5.1.2) were explored:

1. XPlane images
2. Multiple planes extracted from a 3D TEE volume
3. A 3D TEE surface (same 3D volume as option 2).

5.4.1 Methods

5.4.1.1 Equipment and Imaging

Images were collected from three patients undergoing conventional or TAVI aortic valve replacement at the Western University in a protocol approved by the Office of Research Ethics, Western University. For each patient, one XPlane TEE image sequence and one 3D TEE volume sequence lasting two seconds were collected. For each sequence, five images, evenly distributed across the cardiac cycle, were extracted and registered to the preoperative CT. The images in which anatomical targets are not visible were excluded from this study. Two stitched volumes were used in the acquisition of the 3D TEE, with varying frame rates and depths ranging from 7 - 13 cm.

All surface contours were manually selected for the XPlane and multiple plane surface options. For the multiple plane option outlines were selected on 5-6 slices taken 3mm apart. The 3D TEE surface was semi-automatically extracted using a snakes segmentation in the open source software ITK-SNAP (http://www.itksnap.org) [1] followed by manual corrections.

CT scans with voxel spacing 0.62mm x 0.62mm x 0.62mm were acquired on a LightSpeed VCT (GE Healthcare, Fairfield, CT) as part of the patients preoperative assessment. TEE images were acquired on an iE33 with an X7-2t probe (Philips Medical System, Amsterdam, The Netherlands) during the surgical procedure. All images were part of a normal clinical protocol.

5.4.1.2 Registration Assessment

The performance of the registration was assessed using three metrics:

1. Mean point to surface distance following the registration.
2. Target registration error (unsigned distance) of manually identified anatomical landmarks when visible (not all targets are visible on all images):
   (a) Left coronary ostia
   (b) Right coronary ostia

(c) Coaptation point of the three leaflets

3. Capture range analysis with the mean point/surface to surface error and the target registration error as a function of initialization position. 133 initialization positions corresponding to a 40° radius range were used; these positions represent potential variation in user selection of the central axis during initialization. Due to the intrinsic geometry of the aortic root, the registration is most poorly constrained for rotations around the central axis.

5.4.2 Results

Twelve XPlane, seven multiple plane and five surface registrations were performed. The results of the surface registrations are illustrated by Figures 5.12 and 5.13, and summarized quantitatively in Table 5.3 and Figures 5.14 and 5.15. The registration results demonstrate good visual alignment (Figures 5.12, 5.13), and the RMS target registration errors are 4.60, 6.14 and 10.15mm for the XPlane, multiple plane and surface methods respectively. Both the XPlane and multiple plane methods demonstrated significantly better accuracy than the surface method (one-way ANOVA, $p < 0.001$, Figure 5.15), and there was no significant difference in accuracy between the XPlane and multiple plane methods. The surface-based registration method failed in one patient with a previous mechanical valve, where the presence of a high US artifact level introduced by the metal components of the valve interfered with the extraction of an accurate surface.

Table 5.3: Summary of Registration Performance

	XPlane N = 12	Multiple Plane N = 7	Surface N = 5
Target Registration Error (mm)			
Mean	4.35	5.96	9.55
Deviation	1.55	1.71	4.21
RMS	4.60	6.14	10.15
Registration Failures	None	None	1
RMS Point to Surface Distance (mm)	1.41	1.66	2.82
Average Time for intra-op processing steps (s)	73.75	146.23	395.89

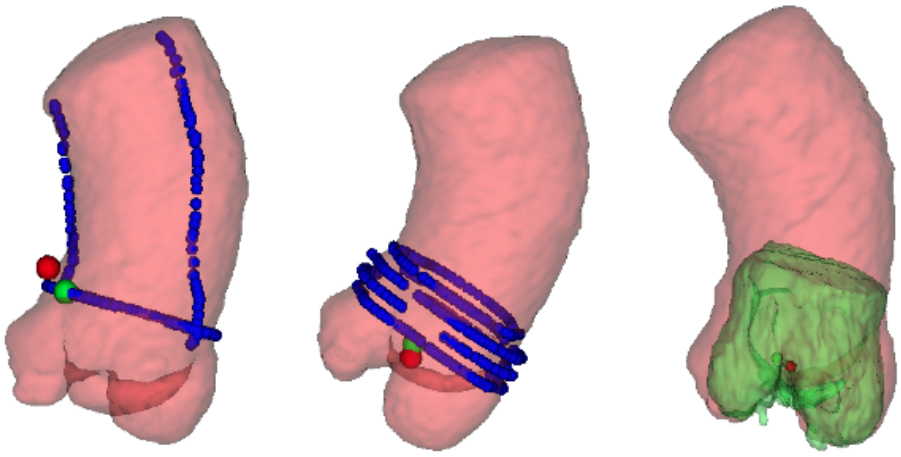

Fig. 5.12: Registration results of the same patient from three different methods. Red surface - extracted from CT. Green surface - extracted from 3D TEE. Blue points - surface points manually extracted from US. Red point - Target identified on CT. Green point - Target identified on US. (a) XPlane image method. A smaller number of points and planes was used, but the larger field of view in the images allows more of the aortic root to be used during the registration. (b) Multiple plane method. Points are distributed more evenly in space, but cover a smaller volume and are derived from a lower resolution image. (c) Surface method. Provides large number of points distributed in 3D, but has low image resolution and image artifacts result. There is poor correspondence between the ultrasound and CT surface.

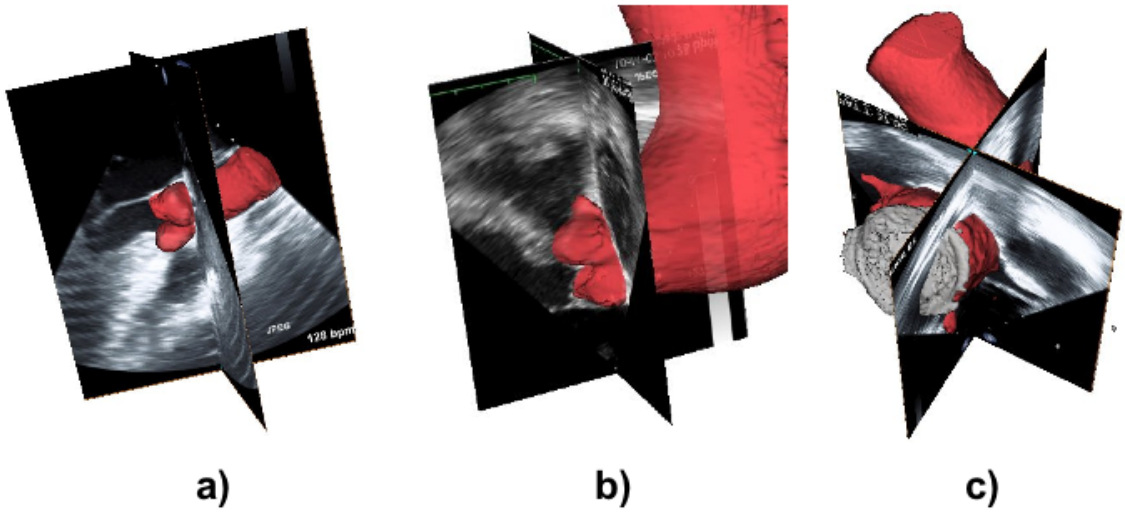

Fig. 5.13: XPlane registration results of three patients with differing valvular pathology. There is good correspondence between the US images and CT surface. (a) Calcified aortic valve. (b) Large aortic aneurysm. (c) Previous mechanical valve and dacron graft.

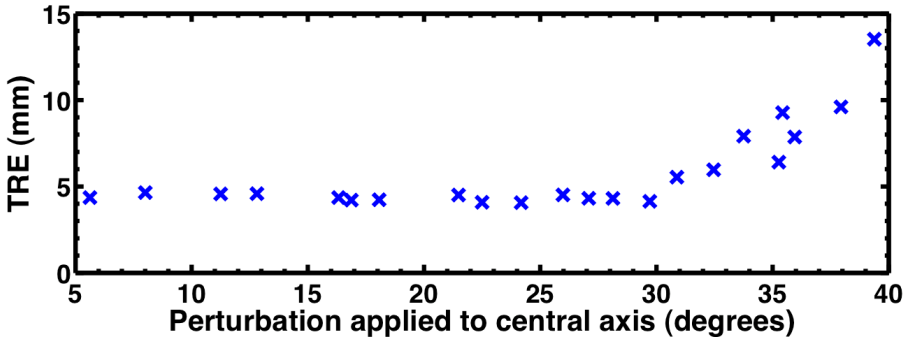

Fig. 5.14: Capture range analysis for XPlane registration showing target registration error as a function of initialization. The algorithm appears to converge close to the correct local minima until the initialization position is perturbed by more than thirty degrees, beyond which it converges incorrectly as illustrated by the rising target registration error.

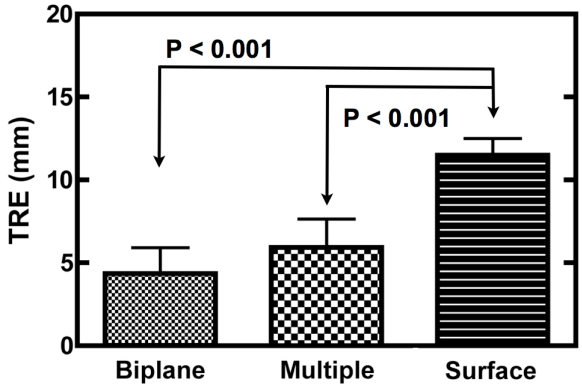

Fig. 5.15: Comparison of RMS target registration errors. Both the XPlane and multiple plane methods performed significantly better than the surface based method.

5.5 Discussion

This study assessed the performance of surface-based TEE-CT registration of the aortic root on clinical data, and demonstrates that a registration can be performed with a target registration error of less than 5mm. The XPlane method of selecting registration points demonstrated significantly better performance than the use of a full surface extracted from 3D TEE. Although theoretically a larger surface should better constrain the registration (as demonstrated in Section 5.2), in practice surfaces derived from 3D TEE are unsuitable due to errors introduced by poor resolution and significant motion artifacts. Furthermore, the XPlane method of selecting registration points required the least user interaction and processing time. With currently available 3D imaging capabilities XPlane contours demonstrate the greatest potential as a clinical tool, however the use of TEE surfaces may need to be re-visited as TEE imaging quality improves.

The error reported in this study overestimates the true registration error, due to the large variability present in manual coronary ostia and co-aptation point target selection.

Results of this study demonstrated good correspondence with the simulated XPlane

slices presented in Section 5.2 (Figure 5.16). This suggests that the measured error is contributed to equally by insufficient geometric constraints of the aortic root subject itself and errors introduced by the TEE imaging process (including artifacts and speed of sound distortions).

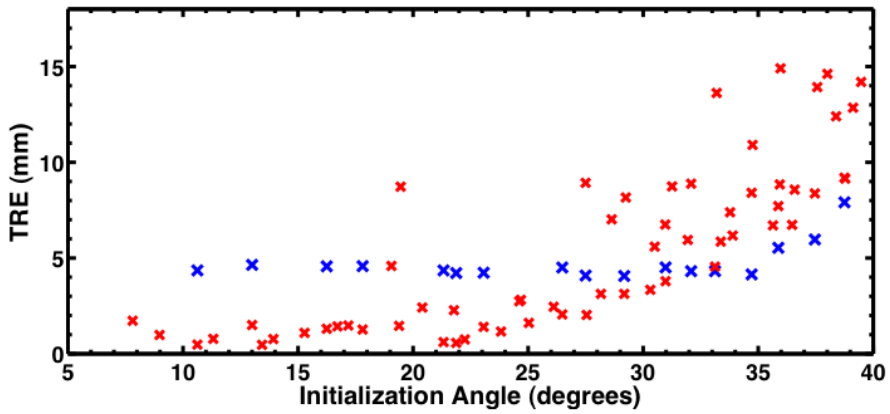

Fig. 5.16: Comparison of target registration errors using the simulated XPlane CT slice (red) and real TEE image (blue).

The registration method successfully handled patients of different pathology and geometry including one with a large ascending aneurysm and a patient with a mechanical valve and dacron graft, demonstrating the versatility of this tool. This is important since patients undergoing TAVI procedures have aortic root pathologies that introduce imaging artifacts and distort the normal anatomy.

A limitation to this study was the small number of data sets used. A more comprehensive accuracy study examining the registration of XPlane contours is provided in Chapter 6.

5.6 Chapter Summary

This chapter presents methodology to register a pre-operative CT image to intra-operatively acquired TEE images. This methodology is designed to allow for real-time registration and display, with minimal user interaction through an automated initialization process. The studies presented compare several methods for extraction of the TEE surface, ranging from sparse data sets consisting of contours on two or more planes to semi-automatically extracted full surfaces. Results suggest that as few as two contours on two planes are sufficient to constrain the registration with reasonable accuracy. While a more complete 3D surface theoretically demonstrates improvement in accuracy, in practice the loss of resolution and motion errors reduce performance.

References

[1] Yoo TS, Ackerman MJ, Lorensen WE, Schroeder W, Chalana V, Aylward S, et al. Engineering and Algorithm Design for an Image Processing API: A Technical Report on ITK - The Insight Toolkit. vol. 85 of Studies in Health Technology and Informatics (Proceedings of Medicine Meets Virtual Reality). IOS Press, Incorporated; 2002. p. 586–592.

[2] Besl PJ, McKay ND. A Method for Registration of 3-D Shapes. IEEE Transactions on Pattern Analysis and Machine Intelligence. 1992;14(2):239–256.

[3] Fitzpatrick JM, West JB, Maurer J C R. Predicting error in rigid-body point-based registration. Medical Imaging, IEEE Transactions on. 1998 oct;17(5):694 –702.

Chapter 6

Automatic TEE Contour Selection for CT-TEE Registration

Chapter 5 demonstrated that CT and XPlane TEE images can be successfully registered together using ICP registration. However, real-time registration and visualization requires TEE contours used in the registration to be automatically selected. This chapter presents an algorithm for selecting appropriate TEE XPlane contours that can be used in registration, and assesses the performance of this algorithm by comparing algorithm-selected contours those that have been identified manually.

6.1 Contour Selection Objectives and Challenges

The aortic root is a difficult structure to segment on TEE images, due to:

- the motion of the leaflets as the valve opens and closes,
- large shadowing artifacts from heavy calcification of the annulus and leaflets,
- large variation in the acquisition parameters used (including scale and image gain),
- wide variation in structure shape between patients and within the same patient over the course of the cardiac cycle (motion of the aortic root over the cardiac cycle causes the image plane to be located at varying positions and angles within the structure)

- intensity heterogeneity caused by the presence of calcium deposits and image speckle.

When the leaflets are closed, the short axis view may divide into several non-continuous segments, and when they are open, the long axis aortic root structure is continuous with the left ventricular outflow tract and left ventricle. In both these cases, the goal is to extract the outer surface of the structure, ignoring edges on the inside of the valve, and selecting points on the long axis view that correspond only to the aortic root above the level of the valve. Depending on the acquisition angle, the thin valve structure may not be visible at all in the long axis view. Example TEE acquisitions demonstrating a range of images is shown in Figure 6.1.

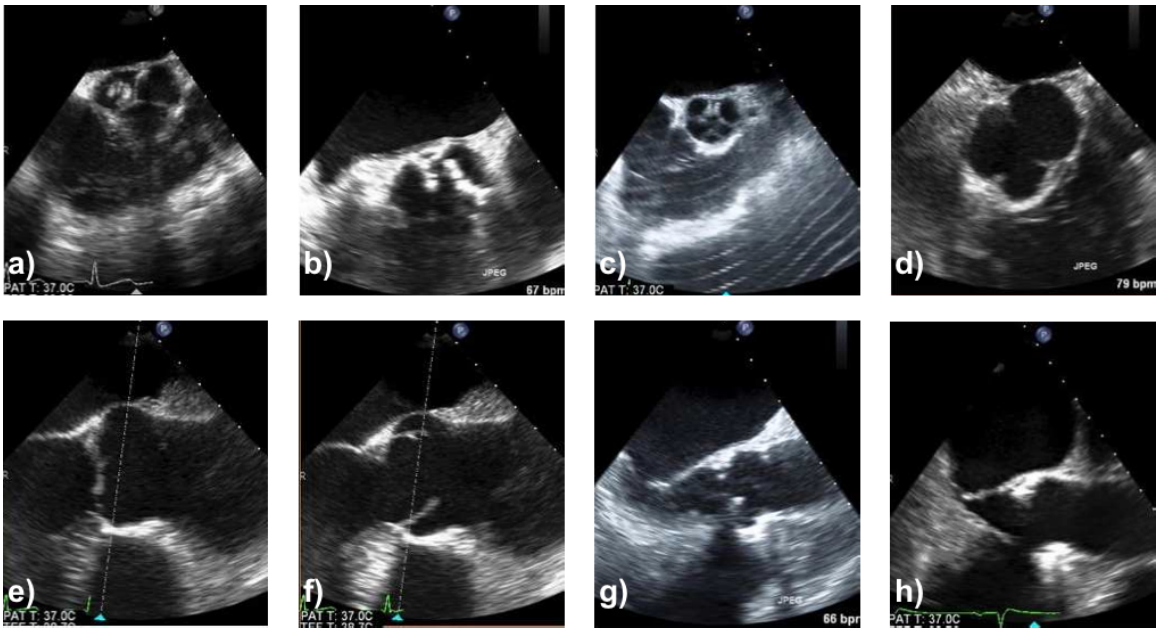

Fig. 6.1: Example short axis (a-d) and long axis (e-h) TEE acquisitions are shown, demonstrating a range of appearances that the segmentation algorithm may encounter. (a) Closed aortic valve with leaflet calcification. (b) Closed valve with shadowing from leaflet calcification. (c) Closed valve showing multiple valve segments and a small image scale. (d) Open valve. (e) Closed valve. (f) Open valve. (g) Closed valve with poor leaflet visibility due to calcification. (h) Open valve with poor leaflet visibility.

6.2 Methods

The image processing workflow used to select TEE contours is described in Figure 6.2. A graph-cut based image segmentation method [1] was used to select the aortic root foreground in each of the TEE views. Post-processing was then used to identify appropriate contours for registration. Since the aortic root is continuous with the left ventricular outflow tract when the valve is open in the long-axis view, curvature analysis is used to select only the parts of the contours that correspond to the aortic root.

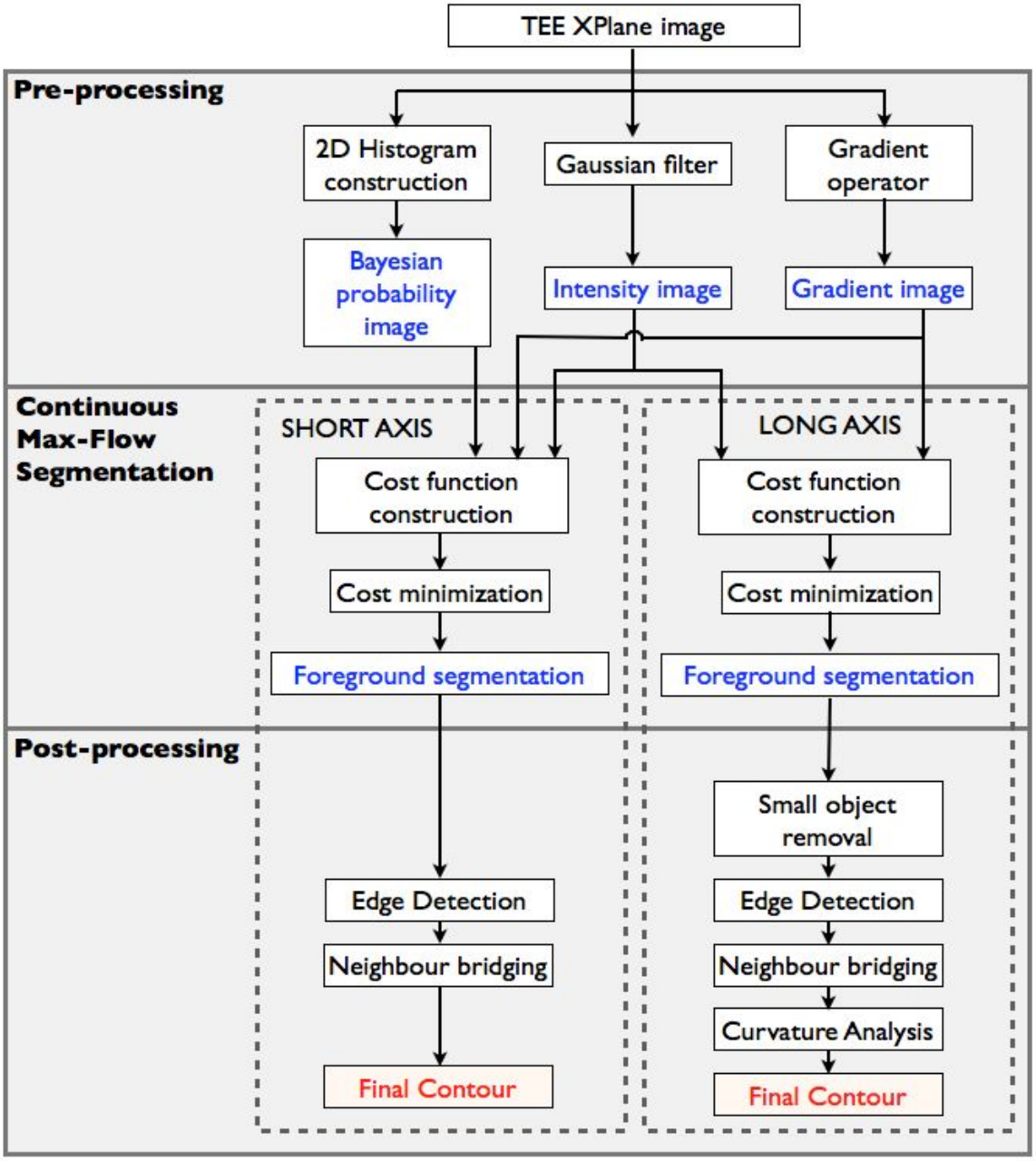

Fig. 6.2: Image processing steps used to select TEE contours on the short and long axis views.

6.2.1 Continuous Max-Flow Image Segmentation

A graph cut is the process of partitioning a directed or undirected graph into disjointed sets. A cost is associated with each possible cut, and the optimal partitioning solution can be found by minimizing the total cost required to partition the graph. Graph cuts are commonly applied to the process of image segmentation by partitioning an image into 'foreground' and 'background' [2]. A max-flow min-cut solution to the optimization problem is the most commonly used method [3]. However, a drawback to using this discrete approach is grid bias that penalizes some spatial directions more than others, leading to artifacts (metrification errors) in the final solution [1]. Yuan *et al.* [1] developed a continuous max-flow approach to solve the same optimization problem in continuous space, avoiding metrification errors. In this study, the continuous max-flow approach is used to solve the segmentation problem.

The image segmentation was performed as a minimization problem of the energy functional (Equation 6.1):

$$\arg \min_{\lambda(v)\in[0,1]} E(\lambda) = \int_{\Omega} \{C(v)_{tot}\lambda(v) + \alpha(v)\|\nabla\lambda(v)\|\}dv \tag{6.1}$$

where:

$\lambda(v) \in [0, 1]$ is a labelling function that labels each pixel as foreground or background,

$C(v)_{tot}$ is the regional penalty to assigning an image pixel as 'foreground', based on image properties,

$\alpha(v)\|\nabla\lambda(v)\|$ is the weighted total variation of the labelling function, and represents a smoothness constraint,

$\alpha(v)$ defines the relative weight of the image property ($C(v)$) and smoothness terms.

In this manuscript, each 2D image space (short axis and long axis) is referred to as Ω, and individual pixel locations as v, where each v has corresponding (x, y) coordinates. In this study, $C(v)_{tot} = C(v)_{fore}$ - $C(v)_{back}$, where $C(v)_{back}$= 1 - $C(v)_{fore}$. For brevity, $C(v)_{fore}$ shall be referred to as $C(v)$ in the remainder of this manuscript. The image properties used to construct the regional penalties are further described in Section 6.2.3.

6.2.2 Pre-processing

The low intensity region representing the left atrium (Figure 6.3) in both the short-axis and long-axis image was removed by thresholding the image and using region-growing to select the relevant region attached to the fan origin, as described in Algorithm 1. If the left atrium segment is not successfully identified by the algorithm, this step is omitted.

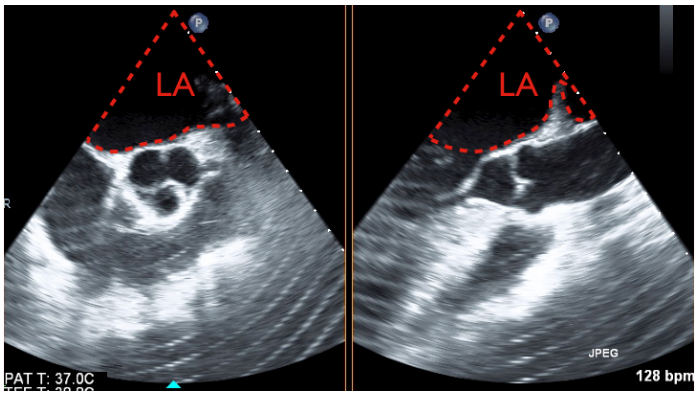

Fig. 6.3: Low-intensity left atrium region removed by pre-processing.

Algorithm 1 Remove left atrial segment

1: Define 'Test Region' as a circular region with radius = 10% of equivalent radius of previous segmentation result, centered at the centroid of the previous result
2: Threshold the image, using an initial threshold of 0.5
3: Using connected components labelling, select the region attached to the fan origin and label as 'Left Atrium'
4: **while** ('Left Atrium' overlaps 'Test Region') & (Threshold <1) **do**
5: Increase threshold by 0.05
6: Use connected components to find new 'Left Atrium' label
7: **end while**

6.2.3 Energy functional construction

In this study, two different energy functionals are used in the segmentation of the short-axis and long-axis images. These energy functionals differ in the regional penalty function ($C(v)$) used (described in Section 6.2.3.1 and Section 6.2.3.2), but employ a common smoothness constraint ($\alpha(v)\|\nabla\lambda(v)\|$). The function $\alpha(v)$ determines the relative weight of the smoothness constraint compared to the regional penalty function. In this study, $\alpha(v)$ is set to the image gradient strength:

$$\alpha(v) = G(v) = \nabla Int(v) * g(x) \tag{6.2}$$

where $g(x)$ is the Gaussian function with $\sigma = 5$, $Int(v)$ is the original image.

Application of Equation 6.2 allows the smoothness constraint to dominate the energy functional where there are weak edges in the image (usually a result of shadowing artifacts), and prevents adjacent blood pool structures (such as inside the aortic valve and the right ventricle) as being labelled as continuous structures. In addition, the gradient function ($G(v)$) is also used in the image penalty functions. Using the same function here reduces the number of required computations.

6.2.3.1 Short Axis

An image penalty term $C_1(v)$, defined in Equation 6.4, was constructed from several image properties, including image intensity ($I(v)$), image gradient strength ($G(v)$) and a probability estimate of the likelihood of each pixel belonging to the foreground ($P(v)$).

Probability Estimate

Many algorithms that have previously been used to segment ultrasound images have relied primarily on image gradients or differences in intensity distributions within the foreground and background [4, 5, 6]. However, due to the varying presence of aortic valve leaflets in the images, areas of high intensity and gradient corresponding to the valves frequently appear within the otherwise relatively homogeneous and

low-intensity blood pool. Furthermore, the motion of the leaflets is sufficiently rapid enough to go from completely open to completely closed within a single frame (25 - 35 Hz), making it difficult to enforce temporal continuity. To correctly label aortic root pixels as 'foreground', a distance constraint can be incorporated into the image penalty term, since pixels spatially close to the centroid of the previous segmentation are more likely to be foreground, irregardless of intensity. However, depending on the position and angle of the ultrasound plane, the aortic root may increase in area, and/or translate within the image from frame to frame. A hard distance constraint incorrectly penalizes the edges in these cases. To address this problem, a probability estimate function ($P(v)$) is constructed based on both intensity and distance, such that high intensity pixels near the centroid of the previous segmentation are identified as likely to be foreground (pixels corresponding to the leaflets), while high intensity pixels further away are labelled as background (correspond to the edge of the aortic root). This probability function was generated by calculating the conditional probability of each pixel being foreground based on its intensity and distance from a centerpoint, using the probability density function estimated from the previous three segmentations (Figure 6.4, Equation 6.3). The centerpoint used is the centroid from the previous segmentation. In the segmentation of the very first frame the probability function is omitted in the cost function, since a probability estimate cannot be created.

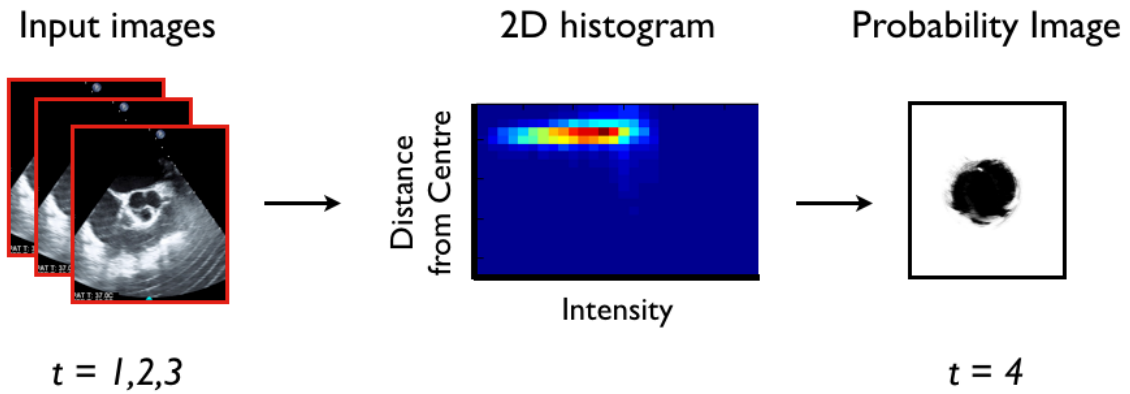

Fig. 6.4: The construction of the probability images. Input from three previous frames is used to construct a 2D histogram from which the probability image is calculated.

$$P(v) = P(F(v)|r(v), I(v)) = \frac{1}{n}\sum_{i=1}^{n}\frac{P(F_i|r(v_i), I(v_i))}{P(r(v_i), I(v_i))} \tag{6.3}$$

where:

$P(F_i))$	=	probability of a pixel belonging to the foreground object
$P(r(v_i), I(v_i))$	=	probability that a pixel occurs at a certain radius and intensity
n	=	number of image segmentations used to construct histogram

In this study, n was set to 3.

Penalty Function Definition

The penalty function $C_1(v)$ was defined as:

$$C_1(v) = \begin{cases} P(v) & \text{if } P(v) < I(v) \text{ and } M(v) = 1 \\ G(v) & \text{if } G(v) > I(v) \text{ and } M(v) = 1 \\ 0 & \text{if } M(v) = 0 \\ I(v) & \text{elsewhere} \end{cases} \tag{6.4}$$

where:

$I(v) = Int(v) * g(v)$

$G(v) = \nabla Int(v) * g(v)$

where $g(v)$ is the Gaussian function with $\sigma = 5$ and $Int(v)$ is the original image

$P(v) =$ Probability function described in Equation 6.3

$$M(v) = \begin{cases} 1 & \text{if pixel is inside the convex hull of the previous segmentation dilated} \\ & \text{by 20\% to account for temporal motion} \\ 0 & \text{elsewhere} \end{cases}$$

This construction uses the probability function near the the centre of the aortic root, where it is a good descriptor of the current image (although the edge location of the foreground segmentations may vary from frame to frame, the centre regions overlap), and the gradient function near the external edge of the aortic root to emphasize the external boundary. Examples of the component functions $I(v), G(v)$ and $P(v)$ are shown in Figure 6.5.

Penalty Function Modification

Due to translation and changes in aortic root size, the probability image used may erroneously include areas of low intensity blood pool close to the aortic root corresponding to the right ventricle and right ventricular outflow tract. Due to imaging artifacts, these areas may be partially continuous with the aortic root. These areas can be identified by dividing the image into radial segments, using the centroid from the previous segmentation as a centre point, and identifying the most external edge in

the gradient image in the masked region in each segment. The penalty function $C(v)$ was created by modifying $C_1(v)$ by additionally penalizing regions beyond the identified edge with a constant offset $\gamma = 0.3$ (Figure 6.5d). The use of segments to identify the edges in the gradient image allow for the partially continuous areas to be penalized appropriately. The algorithm used to modify the penalty function is described in Algorithm 2. An example of the final penalty function used for segmentation is shown in Figure 6.5e.

Algorithm 2 Penalize outer low intensity regions

```
Divide image into 24 radial segments, using the centroid of the previous segmentation as a centre point.
for each segment do
    Plot the average image gradient against distance from the centre
    Calculate GradAvg = image gradient value averaged over entire segment
    Identify peak values
    for each peak do
        Exclude peaks that are too low or too close to the average value (not a true peak):
        if peak value <average gradient OR | peak value - GradAvg | <ε1 then
            Exclude peak
        end if
        Merge peaks that are close together - these often represent the inner and outer edges of the tissue boundary
        if current peak position - last peak position <ε2 then
            Exclude peak
        end if
    end for
end for
```

ϵ_1 and ϵ_2 are constants. In this study, we use $\epsilon_1 = 2(MAD)$ where MAD is the median absolute deviation, and ϵ_2 = 1mm * image scale (corresponding to the maximum expected tissue thickness).

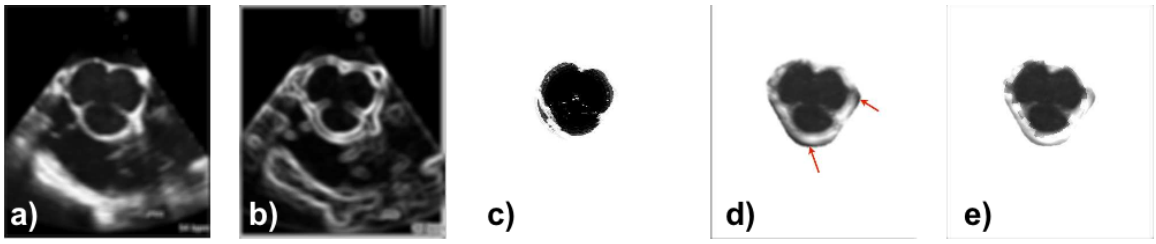

Fig. 6.5: (a) Intensity function (b) Gradient function (c) Probability function (d)Image penalty term before re-weighting, red arrow denotes low intensity areas corresponding to the right ventricle (e) Final image penalty term.

6.2.3.2 Long Axis

The first step of the long axis contour selection is to segment the blood pool corresponding to the aortic root and left ventricular outflow tract (these are continuous when the aortic valve is open). The penalty function $C(v)$ (Equation 6.5) used in this study incorporated three constraints based on the image intensity, the estimated centreline of the previous segmentation, and the horizontal location of the aortic valve plane (Figure 6.6a). In this study, this plane is assumed to be at the midpoint of the image which is a good approximation for all images acquired in this study. Depending on the preferences of the echocardiographer, an approximate location for this plane may be specified before or at the time of acquisition. An example of the resultant segmentation is shown in Figure 6.6c. In the first image, where no previous segmentation is present, the centreline is selected using a horizontal line at a depth determined by the imaging depth settings.

$$C(v) = \alpha I(v) + \beta D(v) + \gamma H(v) \tag{6.5}$$

where:

$I(v) = Int(v) * g(v)$

$D(v) =$ normalized distance function from a line specifying the centreline of the aortic root in the previous segmentation (Figure 6.6b)

$$H(v) = \begin{cases} x/x_{valve} & \text{where } x \leq x_{valve}, \text{ and } x_{valve} \text{ is the position of the valve plane} \\ 0 & \text{elsewhere} \end{cases}$$

α, β and γ are constants that were empirically selected to be 1, 1.5 and 2 respectively.

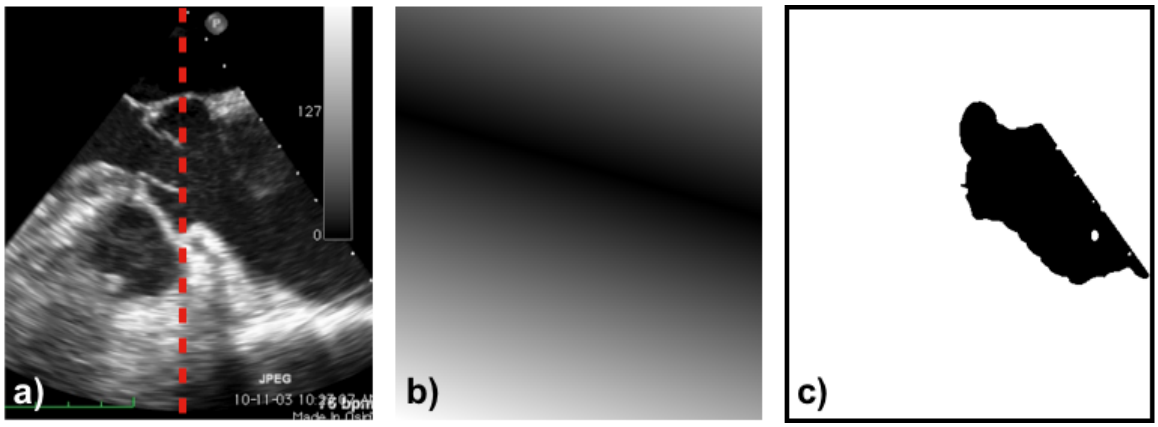

Fig. 6.6: (a) Vertical plane corresponding to the horizontal location of the valve plane on the long axis image. (b) Distance map used. (c) Segmentation result.

6.2.4 Post-processing - Contour selection

Several post-processing steps are required to extract the boundary contour from the continuous max-flow solution. A threshold ($\zeta = 0.95$) is used to divide the continuous solution into foreground and background components. In this study the threshold was empirically selected, although future studies should optimize this parameter on a training data set. A Sobel operator is used to find edge points, and any gaps (defined as a pixel between two edge-labelled pixels) are filled. Finally, a least-squares spline approximation is fit to the identified points as the final contour. In the short-axis view, only one foreground object is identified by the max-flow solution.

However, in the long-axis view, several additional 'noise' objects may be identified. These were removed by using connected components labelling to identify the largest object before edge detection.

6.2.4.1 Curvature Analysis

In the long-axis view, the sections of the surface that are used for registration must be separated from contours corresponding to the deformable valve and the left ventricular outflow tract. This is accomplished using a curvature analysis algorithm, based on the idea that the surface of the aortic root is relatively smooth and uniform, since areas of high curvature occur at the sinutubular junction, and at the aortic valve cusps. This observation can be used to divide the extracted aortic root surface into sections corresponding to above and below the hinge line of the valve. Only points above the hinge line are suitable for use in registration, since a rigid geometry is assumed.

The curvature analysis algorithm first identifies points of high curvature along the segmented edge (Figure 6.7b), using a threshold of 3.5 times the median absolute deviation (MAD) of the curvature value. Curvature at any given point may be sensitive to noise, so only relatively large groups of consecutively high curvature points are selected, using a threshold of 3.5 times the MAD of the group size. Groups of high curvature points corresponding to the right two thirds of the aortic root as it appears on the long axis image are excluded, using the *a priori* knowledge that long axis images are always acquired with the valve positioned on the left, and the tubular part of the aortic root on the right (Figure 6.7c). Finally, the high curvature points closest to the tubular part of the aortic root on the top and bottom are selected as 'cut-off' points. All points to the left of these cut-off points are included in the contours used for registration (Figure 6.7d). Further details are described in Algorithm 3.

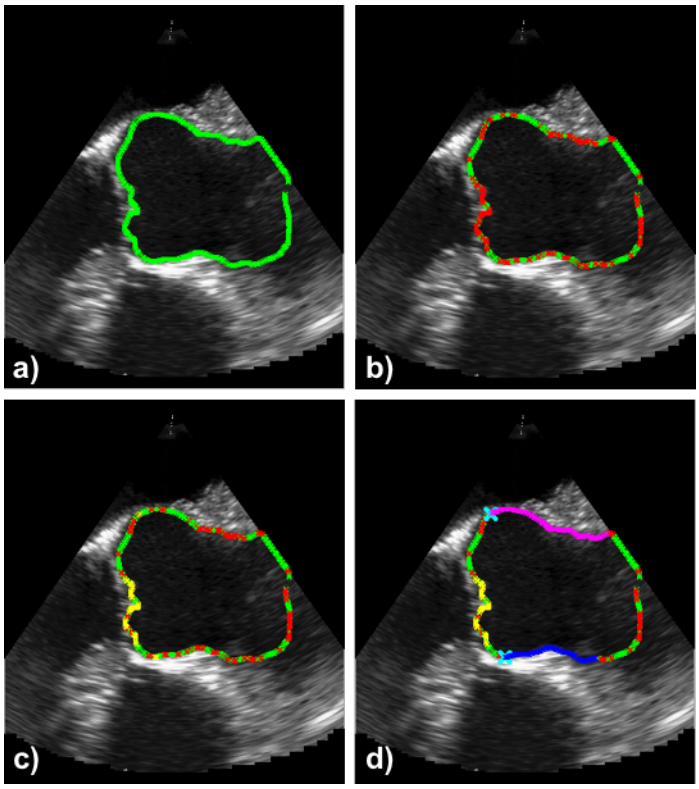

Fig. 6.7: (a) Segmented edge (b) Points of high curvature are shown in red (c) Large groups of high curvature points falling on the right 1/3 of the aortic root stucture are shown in yellow (d) The 'cut-off' points selected are shown in cyan, and the two groups of points selected for use in registration are shown in blue and magenta.

Algorithm 3 Curvature analysis

1: Exclude all points that fall along the fan edge boundaries
2: Find starting point (P_{first}): point closest to the right fan edge
3: Re-order pixels to form a continuous contour starting at P_{first}
4: Create list of high curvature using $K = \frac{|y''|}{(1+y'^2)^{3/2}}$
5: Calculate K_{MAD} = median absolute deviation of K
6: Calculate $Thresh_{curvature} = 3.5K_{MAD}$
7: Exclude all points that fall below $Thresh_{curvature}$.
8: Group remaining points into groups of consecutive pixels
9: Calculate $GroupSize_{MAD}$ = median absolute deviation of the number of pixels in each group
10: Calculate $Thresh_{GroupSize} = 3.5GroupSize_{MAD}$
11: Exclude all points that fall below $Thresh_{GroupSize}$.
12: Determine major and minor axis of the segmented foreground region
13: Define new coordinate system x'-y' along the major and minor axes respectively
14: Determine the x' bounds of the foreground object: x_{min}, x_{max}, and $x_{length} = x_{max} - x_{min}$
15: Exclude all points that fall between x_{max} and $x_{min} + (2/3)x_{length}$
16: Find the two groups of points remaining on the list closest to the first and last point on the contour, and identify these as 'cut-off' points for the top and bottom segments respectively
17: From the original contour, select all points from each 'cut-off' point to the first and last point, excluding points that fall on the fan edge

Note that the choice of $3.5MAD$ and $(2/3)x_{length}$ are empirically determined in this study, and should be optimized in future work.

6.3 Validation Study

6.3.1 Methods

The performance of the contour-selection methodology was evaluated using intra-operative TEE images. For each patient, XPlane images corresponding to one cardiac cycle were both manually and automatically segmented. If the patient had a clinical CT scan, both sets of contours were registered to the patient's CT-derived model using the methodology described in Chapter 5.

Performance was evaluated by:

- Comparing the location of automatically selected contours to the gold standard manually selected contours
- Comparing the target registration errors (TRE) obtained with automatically selected and manually selected contours.

6.3.1.1 Data and Imaging

The evaluation study included 8 patients who received clinical TEE XPlane imaging on a Philips iE33 ultrasound system with an X7-2t 3D TEE probe (Philips Healthcare, Andover, MA) five of whom also received clinical CT scans (GE Lightspeed VCT, GE Healthcare, Conneticut, US). The patients provided written informed consent, and the study protocol was approved by the Western University Board of Human Research Ethics. The XPlane view provides simultaneous imaging of two intersecting planes showing the short-axis and the long-axis. Imaging parameters, including image scale and gain are determined by the operator, and vary significantly between images and patients.

6.3.1.2 Evaluation Metrics

Segmentation Evaluation

Boundary measures are the most relevant in this study, since the intended application is surface extraction for ICP registration. The boundary measures used to assess

the segmentation include the mean boundary distance, and the maximum boundary difference in each image. Boundary measures are reported for both the short and long axis segmentations.

For completeness, the dice metric (DM = $\frac{2A_{overlap}}{A_{algorithm}+A_{manual}}$) was reported as an overlap measure for the short axis segmentation. The dice metric cannot be reported for the long axis segmentation since the segmented boundary does not form a closed loop.

The averages across all images and all subjects were computed for each metric to obtain an overall estimate for the entire data set.

Registration Evaluation

The registration performance is assessed by measuring the RMS point-to-surface distance and a target registration error (TRE) as described in Chapter 5. The right and left coronary ostia, when visible on the TEE images, are used as targets. Accuracy of the registration using the manually selected and automatically selected contours are compared.

In addition to the original ICP algorithm described by Besl *et. al.* [7], the performance of two modified ICP variants are evaluated:

1. **Worst Point Rejection**: In each iteration, a percentage of the points with the highest point-to-surface distance are excluded from the next iteration. This method attempts to reduce the influence of outliers. Removal of up to 5% of outliers (in increments of 1%) was evaluated.
2. **Multi-resolution Registration**: A series of 5 CT surfaces were generated by applying a varying number of iterations of a smoothing filter to the original CT mesh. The registration output of each surface is used to initialize a registration using the next CT surface, starting with the most smooth surface, ending with the original surface. The smoothed surfaces maintain the general underlying geometry of the aortic root, but remove fine details. The CT surfaces were generated using Scale Dependent Laplacian Smoothing, based on the Fujiwara extended umbrella operator in the software MeshLab (Visual Computing

Lab - ISTI-CNR, http://meshlab.sourceforge.net/). The number of smoothing steps used in each level were 0, 5, 10, 50, and 100, with smoothing parameters automatically selected by the software (Figure 6.8).

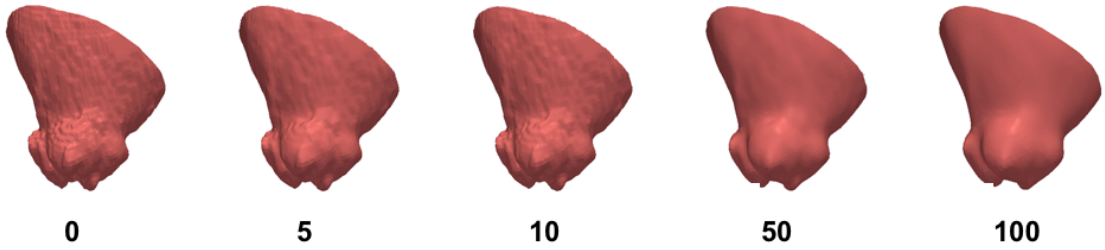

Fig. 6.8: CT meshes used with differing number of smoothing steps in multi-resolution registration.

6.3.2 Results

6.3.2.1 Segmentation Results

Assessment of intra-operator contour selection variability

Intra-operator variability of the manual gold standard was estimated by comparing the segmentations of 3 experts on 30 images evenly distributed across the cardiac cycle and taken from 3 different patients. Boundary distance and dice metric measures were calculated by measuring the deviation from the mean contour of each user. Results are summarized in Table 6.1.

Table 6.1: Summary of intra-operator variability. Distances are measured in mm, area measures reported as %. Max distance is the mean of the maximum boundary distance measured on each image. N = 30.

	Boundary Distance				Dice Metric		
	RMS	Mean	Std	Max	RMS	Mean	Std
Short Axis	0.80	0.78	0.17	3.29	0.96	0.96	0.01
Long Axis	1.25	1.14	0.522	5.66	N/A		

Automatic contour selection performance

Representative short-axis and long-axis segmentation results are shown in Figures 6.10 and Figure 6.11 respectively, and the overall performance of the algorithms over 8 patients and 122 images are summarized in Table 6.2. Results demonstrate good visual correspondence between the algorithm and manual contours. Furthermore, the difference between the algorithm and manual segmentations was less than 0.4mm greater than the measured intra-operator variability.

Table 6.2: Summary of segmentation results. Distances are measured in mm, area measures reported as %. Max distance is the mean of the maximum boundary distance measured on each image. N = 204

	Boundary Distance				Dice Metric			
	RMS	Mean	Std	Max	RMS	Mean	Std	Minimum
Short Axis	1.00	0.94	0.35	3.42	0.94	0.94	0.017	0.90
Long Axis	2.01	1.54	1.30	5.88	N/A			

For most image sequences, the performance of the segmentation algorithm varies substantially over the cardiac cycle, with peaks that are significantly higher than the mean (Figure 6.9). However, the location of error peaks within the cardiac cycle is not consistent from one patient to the next, likely reflecting the motion of the imaging plane with respect to the aortic root over the cardiac cycle. As the imaging plane moves, calcifications that cause shadowing and other artifacts move in and out of view, resulting in sudden increases in error where the segmentation is poorly constrained.

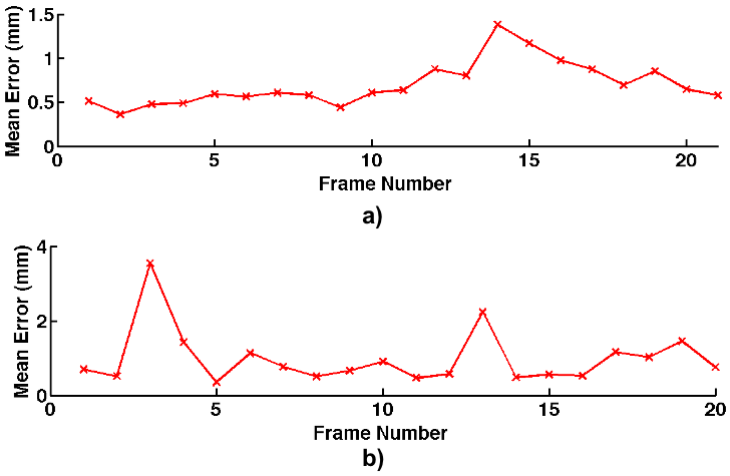

Fig. 6.9: Example of variation of segmentation error as a function of frame number within the cardiac cycle for one patient (a) Short Axis. (b) Long Axis.

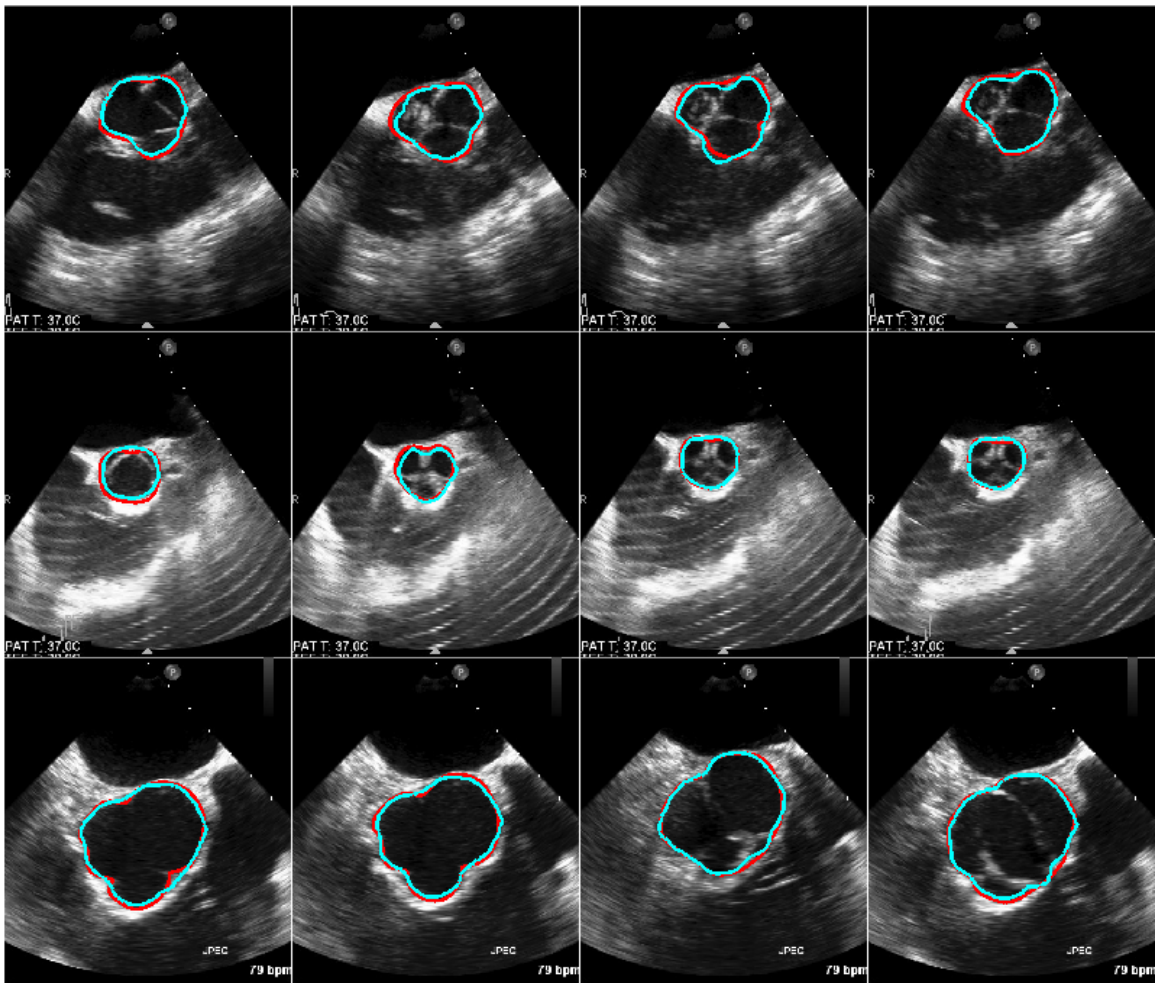

Fig. 6.10: Example short axis contour selection results showing images corresponding to four points in the cardiac cycle for three patients. Red - gold standard manual segmentation. Cyan - automatic segmentation selected by the algorithm.

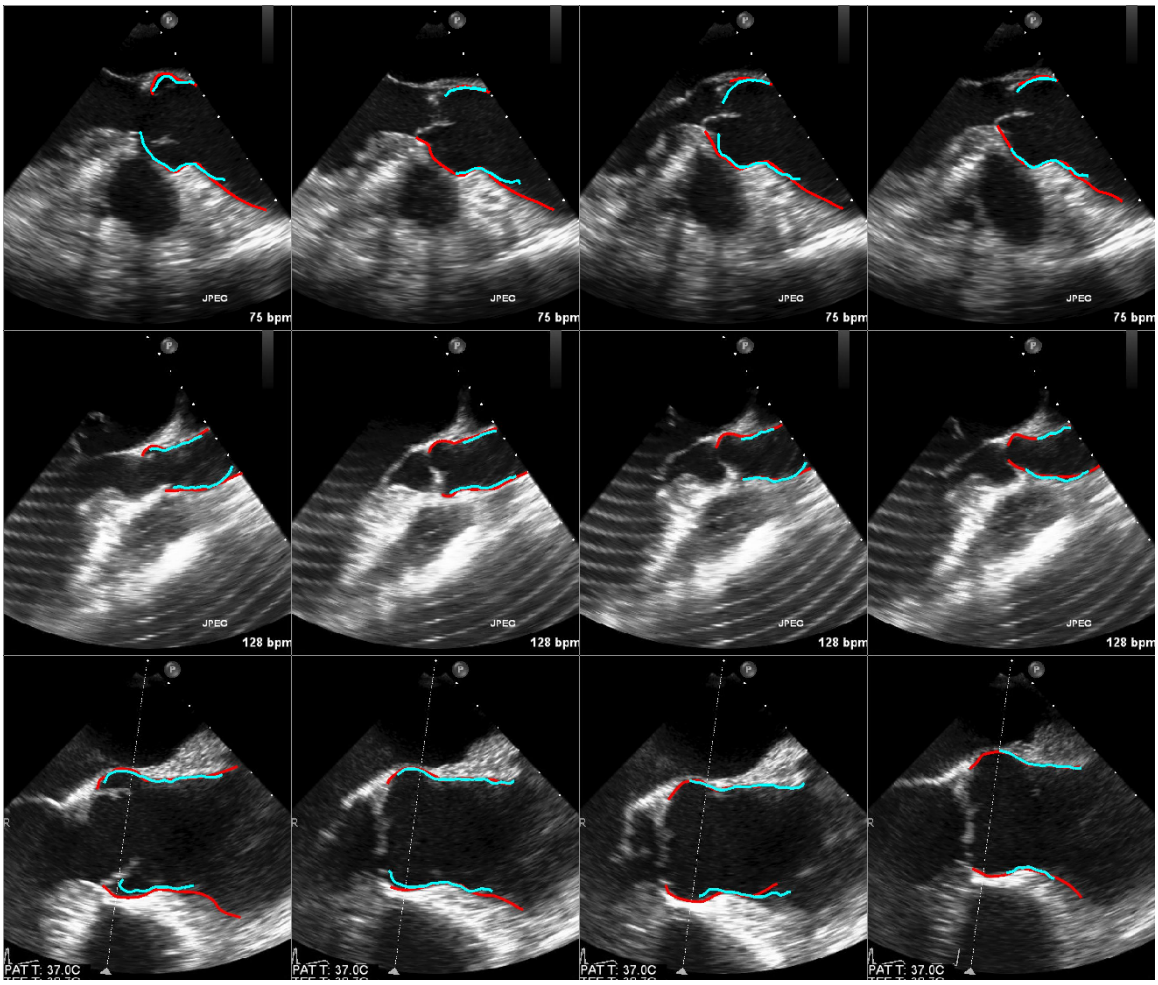

Fig. 6.11: Example long axis contour selection results showing images corresponding to four points in the cardiac cycle for three patients (patients correspond to those shown in Figure 6.10). Red - gold standard manual segmentation. Cyan - automatic segmentation selected by the algorithm.

6.3.2.2 Registration Results

Registration results of the 5 patients with CT images are summarized in Table 6.3. A paired Student's t-test was used to compare the registration accuracy of the manually and automatically selected contours. As expected, registration error was higher when using the automatically segmented contours ($p < 0.001$), likely due to the error introduced in the segmentation process. In addition, the standard deviation of the

automatically segmented contours was higher than the manually segmented contours, since poorly segmented frames were unable to converge to the correct local minima.

Registration accuracy depends on patient geometry and the presence of geometric features within the aortic root to constrain the registration. A one-way analysis of variance (ANOVA) was used to test for differences in the registration accuracy achieved between the different patients. There were significant differences between the TRE measured in different patients for both the manually-selected contours ($F(5, 70) = 5$, $p < 0.05$), and the automatically-selected contours ($F(5, 69) = 8.05$, $p < 0.05$).

Table 6.3: TRE results using manual and automatic contour selection

Method	mean TRE (mm)	standard deviation (mm)
Manual	4.54	1.75
Automatic	6.00	2.06

ICP Variants

Worst Point Rejection

The effect of rejecting a percentage of the worst-fitting points during the ICP process is shown in Figure 6.12. As the number of worst-fitting points rejected increased, mean registration accuracy using the manually-selected contours decreases, while the variance of the TRE increases. In contrast, mean registration accuracy using the automatically-selected contours increases, with the minimum TRE occurring with a rejection of 2% of the points during the ICP registration.

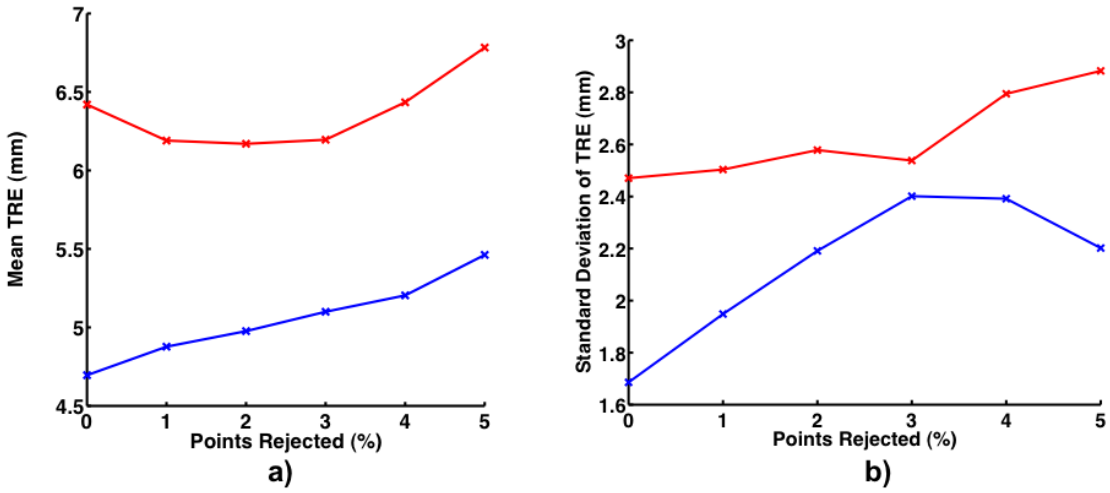

Fig. 6.12: TRE as a function of the percentage of worst-fitting points rejected from the ICP process. Red - Automatically selected contours. Blue - manually selected contours. (a) Mean TRE. (b) Standard Deviation of the TRE.

Multi-Resolution Registration

The effect of using a multi-resolution surface scheme is summarized in Table 6.4. Registration results obtained using a multi-resolution registration scheme were compared via a Student's t-test to registration results using the original ICP algorithm. The use of multi-resolution registration demonstrated worse performance with both the manually-selected contours and the automatically-selected contours ($p<0.05$).

Table 6.4: Mean TRE results using multi-resolution registration

Method	Original ICP	multi-resolution ICP
Manual	4.54	6.06
Automatic	6.00	8.52

6.3.3 Discussion

6.3.3.1 Automatic Contour Selection Performance

Results of this study demonstrate that contours of the aortic root can be automatically delineated on XPlane images, and registered to a pre-operative CT model with reasonable accuracy. Comparison between the manually and automatically selected contours demonstrated mean boundary differences of 1-2mm and an average dice metric of 0.94. The accuracy can be further improved by identifying poorly segmented frames by comparing each to the prior frame and excluding frames that do not demonstrate reasonable temporal continuity.

The reported results are consistent with the measured accuracy of similar ultrasound segmentation work. Rajchl *et. al.* [8] reported segmentation errors of 3.54±1.63 mm in the segmentation of 3D left heart volumes. With these data sets a slightly lower segmentation accuracy is expected, due to a large voxel spacing. Ukwatta *et. al* [9] report a dice metric of 0.95 and mean absolute distances of 0.3± 0.1mm in the segmentation of the lumen and media-adventitia boundaries using a semi-automated algorithm. Compared to the segmentation problem presented in this chapter, this study benefits from additional user input and greater consistency between frames in the images (no valve motion).

Although the short axis segmentation incorporates previously segmented frames into the creation of the probability function ($P(v)$), segmentation performance is not significantly affected by the segmentation performance of previous frames, and segmentation error does not increase over time during an image sequence. The algorithm is robust to several different patient anatomies and pathologies, and successfully handled images that had varying gain and image scales, were acquired at different positions along the aortic root, and acquired at varying time-points in the cardiac cycle.

6.3.3.2 Comparison of Registration Performance using Manually and Automatically Selected Contours

The mean target registration error using manually and automatically selected contours differs by less than 1.5mm. This registration performance is consistent with segmentation evaluation using region and boundary-based methods. There remains a significant difference between the accuracy achieved using the two types of contours, suggesting that there is some room for improvement in the development of better contour-selection algorithms.

The registration accuracy of manually selected contours was not improved by using worst point rejection in the ICP registration. Given the sparsity of the point set, the removal of points likely corresponds to a removal of important constraining information for the registration. Furthermore, the manually selected contour likely deviates minimally from the true blood-tissue boundary and is unlikely to contain a large number of outliers that may erroneously influence the registration. The standard deviation of the TRE also increases using worst point rejection, suggesting that the registration is more likely to converge to an incorrect local minima.

In comparison, the registration accuracy of automatically selected contours was improved by approximately 0.5mm by rejecting 1 or 2 % of the worst-fitting points during registration. Compared to manual outlining, automatically selected contours are more likely to contain erroneous outliers that may influence registration performance. Rejection of greater than 2 % of points corresponds to a decrease in registration accuracy, probably because enough points are removed that significant constraining features are lost.

The use of a multi-resolution registration scheme demonstrated worse performance than the original ICP algorithm. It is likely the Laplacian mesh smoothing algorithm significantly modifies the shape of the CT mesh, reducing accuracy. Furthermore, this result is consistent with studies in Chapter 5 that suggest inaccuracies in TEE contour selection contribute the majority of registration error. Better shape-preserving mesh smoothing algorithms could potentially demonstrate better results. It should also be noted that the use of multiple registrations does increase computational load.

6.3.3.3 Future Work

Optimization of empirical parameters

Several constants were used in the construction of the cost functionals. In this study, these values were empirically determined. Future work should aim to select these parameters using a large training data set covering different potential patient pathologies.

Enforcing temporal continuity

Temporal continuity is an important part of an echocardiographer's reading and interpretation of images, and contains valuable information used in the classification of anatomical structures. Currently some temporal information is indirectly incorporated into the segmentation process by initializing parameters and constructing probability images based on previous frames. Accuracy can potentially be improved by further enforcing temporal continuity in both the contour selection and registration steps of the process. For example, it may be possible to implement automatic detection of poorly segmented TEE images to exclude these frames from the registration. The TEE XPlane images are acquired at approximately 25 - 35 Hz, and excluding a small percentage of non-continuous frames is unlikely to change visualization performance. In addition the output of the ICP registration may benefit by being constrained to be temporally continuous.

GPU processing

In this chapter, all algorithm prototyping was done in Matlab, and the image processing took up to several seconds per frame. Graph-cut segmentations are amenable to GPU processing, and this technique has been used to accelerate many graph-cut based tasks by several orders of magnitude [8, 10, 11]. Due to the small image size (two 145 x 70 pixel images) it is expected that a GPU implementation should allow for the real-time processing necessary for intra-operative use.

6.4 Chapter Summary

This chapter presented a method for automated contour selection of aortic root images defined by XPlane. These contours can be used in the registration methodology presented in Chapter 5 to automatically register pre-operative CT models to intra-operative TEE. The clinical need for full automation, the large variation in image acquisition parameters and the presence of valve motion and artifacts makes this a particularly challenging problem. The contour selection method uses a continuous max-flow image segmentation, followed by curvature analysis. An energy functional was defined using the image intensity and geometric properties of the aortic root. Validation studies demonstrated good congruency between manually and automatically selected contours, and demonstrates that registration using automatically selected contours can be achieved with a target registration error of 6mm. This accuracy suggests that the methods presented may be suitable for future clinical use. However, there remains a 1.5mm difference in registration accuracy between manually and automatically selected contours, suggesting that there remains room for improvements in the segmentation process.

References

[1] Yuan J, Bae E, Tai X. A study on continuous max-flow and min-cut approaches. In: IEEE Conference on Computer Vision and Pattern Recognition; 2010. p. 2217–2224.

[2] Boykov YY, Jolly MP. Interactive graph cuts for optimal boundary & region segmentation of objects in N-D images. vol. 1; 2001. p. 105–112.

[3] Boykov Y, Kolmogorov V. An experimental comparison of min-cut/max- flow algorithms for energy minimization in vision. Pattern Analysis and Machine Intelligence, IEEE Transactions on. 2004 sept;26(9):1124 –1137.

[4] Schneider RJ, Perrin DP, Vasilyev NV, andP J Del Nido GRM, Howe RD. Mitral annulus segmentation from 3D ultrasound using graph cuts. IEEE Transactions on Medical Imaging. 2010;29(9):1676–1687.

[5] Noble JA, Boukerroui D. Ultrasound Image Segmentation: A Survey. IEEE Transactions on Medical Imaging. 2006;25:987–1009.

[6] Lang P, Rajchl M, Li F, Peters T. Towards model-enhanced real-time ultrasound guided cardiac interventions. In: Proceedings of IEEE ICBMI; 2011. .

[7] Besl PJ, McKay ND. A Method for Registration of 3-D Shapes. IEEE Transactions on Pattern Analysis and Machine Intelligence. 1992;14(2):239–256.

[8] Rajchl M, Yuan J, Peters TM. Real-time segmentation in 4D ultrasound with continuous max-flow. vol. 8314. SPIE; 2012. p. 83141F.

[9] Ukwatta E, Awad J, Ward AD, Samarabandu J, Krasinski A, Parraga G, et al. Segmentation of the lumen and media-adventitia boundaries of the common carotid artery from 3D ultrasound images. vol. 7963. SPIE; 2011. p. 79630G.

[10] Vineet V, Narayanan PJ. CUDA cuts: Fast graph cuts on the GPU. In: Computer Vision and Pattern Recognition Workshops, 2008. CVPRW '08. IEEE Computer Society Conference on; 2008. p. 1 –8.

[11] Gong M, Cheng L. Real-time foreground segmentation on GPUs using local online learning and global graph cut optimization. In: Pattern Recognition, 2008. ICPR 2008. 19th International Conference on; 2008. p. 1 –4.

Chapter 7

Conclusions

The objective of this thesis was to develop an augmented image-guidance system for the TAVI procedure. While there have been major advancements in valve design and access routes, TAVI still relies largely on single-plane fluoroscopy for intraoperative navigation and guidance, which provides only gross imaging of anatomical structures. Inadequate imaging, leading to suboptimal valve positioning contributes to many of the early complications experienced by TAVI patients, including valve embolism, coronary ostia obstruction, paravalvular leak, heart block and secondary nephrotoxicity from contrast use. An image-guidance system capable of combining anatomical landmarks from CT with intra-operative valve and stent motion visualized on TEE and fluoroscopy has the potential to significantly reduce complications in TAVI procedures, resulting in improvements in morbidity and mortality.

Chapter 2 describes the design objectives and constraints for an image-guidance system for TAVI, and introduces the overall system design. Available technologies and registration approaches relevant to this design problem were explored, and a two-part registration approach to bringing all three images into a common coordinate system is described, where the TEE image serves as an intermediate step for CT-fluoroscopy registration:

1. **TEE-fluoroscopy registration** using single-perspective TEE pose estimation
2. **CT-TEE registration** using surface matching.

Chapter 3 assesses the suitability of a fiducial-based and an image intensity-based method of single-perspective TEE pose estimation. The tracking accuracy of each method was assessed using a combination of theoretical and *ex vivo* studies, and the relative advantages and disadvantages of each method are explored. It was discovered that with current techniques the intensity-based method does not have sufficient accuracy for a TAVI guidance system, although future improvements incorporating greater *a priori* knowledge may increase its suitability. The only disadvantage to the use of the fiducial-based method was the need for external tracking fiducials on the TEE probe head, which requires only a minor modification to the TEE probe. In this thesis, a removeable silicone covering with embedded tantalum fiducials was used.

Chapter 4 develops a TEE-fluoroscopy registration system using the fiducial-based TEE probe tracking technique selected in Chapter 3. This system minimizes required intra-operative interaction, by using an automated initialization algorithm for fiducial detection and point correspondence, and by using calibration procedures that are entirely pre-operative. The accuracy and robustness of this system was evaluated on phantoms, *ex vivo*, and *in vivo* porcine models, and these studies demonstrated that the two imaging modalities can be registered together with an error of less than 1.5mm.

In Chapter 5, CT and TEE images are registered together using surface-based ICP registration. Due to the limitations of currently available ultrasound imaging techniques, there exists a pertinent trade-off between image resolution and the size of the imaged volume. While 3D TEE imaging covers a large volume and the entire aortic root surface, it suffers from low image resolution and the need for image stitching. In contrast, 2D XPlane images can provide high spatial and temporal resolution, but can provide only a sparse set of points derived from only two imaging planes. Through theoretical, *ex vivo* and *in vivo* studies, the performance of several TEE surface point selection options were explored. It was determined that with current imaging technology, contours derived from XPlane images resulted in the highest registration accuracy. However, the study in Section 5.2 demonstrated that this sparse contour set does suffer from a lack of constraining geometry, and while currently remains the best option, may not be the optimal solution if the quality of 3D imaging improves.

Since this registration is also intended to be used intra-operatively with real-time update and display, a rapid initialization procedure with minimal user interaction was developed. The robustness of this procedure was studied using capture range analysis, and demonstrated that a clinically acceptable error was achieved with perturbations in initialization of up to 35° (rotational) and 9mm (translational). This range of positions include any initialization position that may be generated by the proposed initialization procedure.

In Chapter 5, all surface points used in the registrations were selected either manually or semi-automatically. While this allows for the merged images to be used peri-operatively, in the operating room immediately before the procedure begins, it does not allow for real-time update during the procedure. In Chapter 6, a method of automatically selecting contours from XPlane images to be used in registration was developed. This approach relied on a graph-cut image segmentation based on probability estimates generated from image intensity and spatial position, followed by curvature analysis to select appropriate contour segments. Performance of the contour-selection method was assessed by comparing to manually selected contours. It was also discovered that registration performance of the automatically-selected contours can be further improved by using a modified ICP algorithm in which 1% of the worst-fitting points in each iteration is omitted from the registration. With these methods, the two modalities can be automatically registered together with a clinically acceptable average error of 5.5mm.

In this thesis, all of the necessary components to creating an integrated image-guidance environment have been developed and evaluated on phantom, animal, and human models. This image-guidance environment allows a pre-operative CT model and intra-operative TEE and fluoroscopy to be visualized together in any combination (Figure 7.1), and is designed for efficient and cost-effective intra-operative use. Thus far, all components have been developed and tested in the laboratory, by post-processing images using a simulated data stream. This system is now ready to be implemented in a prototype suitable for intra-operative use, with an integrated display interface allowing the surgeon to interact with the images and use the device in clinical trials.

7.1 Augmented Image Visualization Environment

Once the images have been registered into a common coordinate frame, they can be visualized in many different ways. Linte *et al* [1] have identified three fundamental factors that need to be considered when developing a surgical visualization and navigation environment: image fusion, 3D visualization and interaction, and navigation and hand-eye coordination.

7.1.1 Image Fusion

Image fusion involves integrating the multi-modality images for simultaneous visualization. Some potential image fusion options are shown in Figure 7.1. Although image integration creates a unified display that streamlines surgical workflow, excessive data fusion may have negative consequences, such as cognitive overload and loss of contrast [1]. Incorporating certain perceptual factors - known as preattentive features - into the visualization pipeline and avoiding unnecessary information and conflicting cues can greatly reduce the memory load. For example, reducing the detail in the aortic root surface and combining different modalities using translucency, outlines and shading can facilitate better perception.

Visualization of TEE and fluoroscopy together is particularly challenging since TEE is a 2D plane and fluoroscopy is a projection image. If the TEE image is close to parallel to the fluoroscopy projection direction, any attempts to project the TEE image onto the fluoroscopy image plane may distort the image and result in a loss of resolution. An example of this was shown in Figure 4.19 in Chapter 4. In Chapter 4 the idea of marking only the locations of specific anatomical features in a 'feature-enhanced' view was also explored (Figure 4.20). Such views may also result in a loss of important information, since the relevant anatomical features must be pre-defined. Furthermore, automated feature-detection requires significant effort and may result in a loss of accuracy. An easy and intuitive method of visualizing multiple modalities intra-operatively remains an open research question.

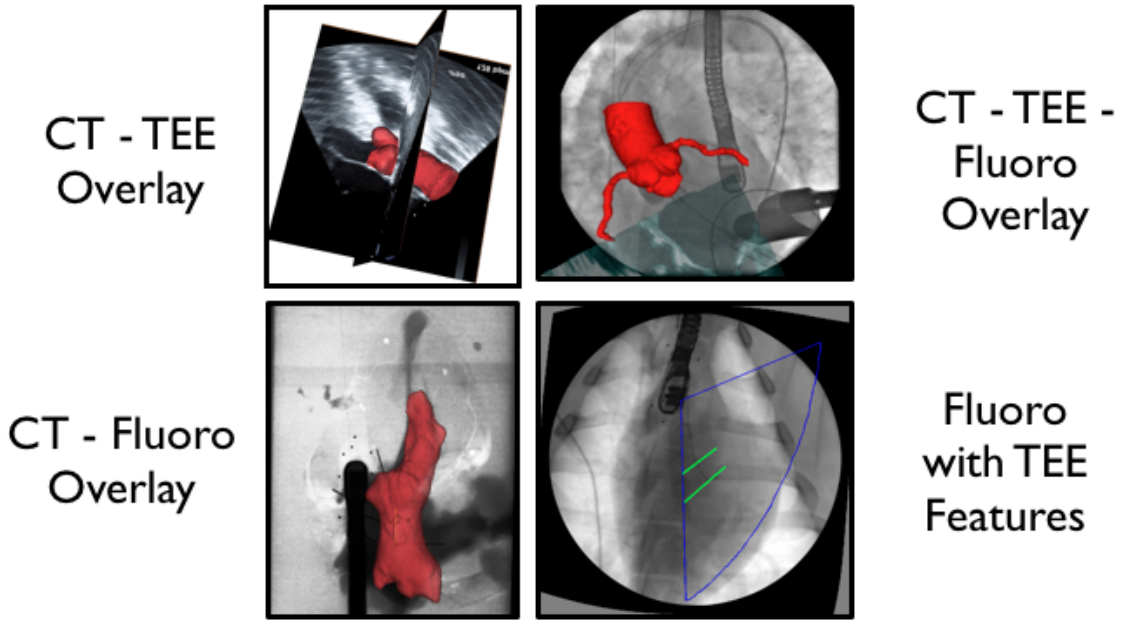

Fig. 7.1: Visualization Options

7.1.2 3D Visualization and Interaction

A surgeon may interact with 3D data in an augmented reality surgical environment in many ways, and a good surgeon-to-computer interface is required to optimize surgical performance. The typical means of displaying multi-modality images in the operating room consists of a standard 2D monitor and a technician at a remote station controlling the display of the virtual scene according to the surgeon's verbal commands [2]. This setup may introduce through difficulty in establishing orientation, insufficient depth perception and ambiguity in communicating view adjustments. Panning, rotating and zooming of the camera may lead to disorientation resulting in frustration and compromises in patient safety. Lo *et al.* [2] suggest the use of standardized medical view angles and two-handed tangible view control as potential solutions to these problems.

7.1.3 Navigation and eye-hand coordination

The performance of a surgeon in any manual dexterity task is affected by the relative position of surgeons, patients and the display. For example, it has been shown that in endoscopic procedures, performance can be improved by placing the image display at a level below the head, in front of the surgeons and close to the hands [3]. A similar approach should be used for the TAVI procedure. Other approaches that have been explored experimentally include the use of head-mounted displays and see-through screens which may further improve eye-hand coordination by *in situ* visualization of the medical data.

7.2 Proposed TAVI Workflow

The proposed image processing workflow for TAVI image-guidance is shown in Figure 7.2, and the proposed clinical workflow is shown in Figure 7.3. All of the image processing steps that require user interaction occur pre-operatively, minimizing additional time in the OR, and requiring minimal modification to the existing clinical procedure. Furthermore, no changes are required to the existing image acquisition process.

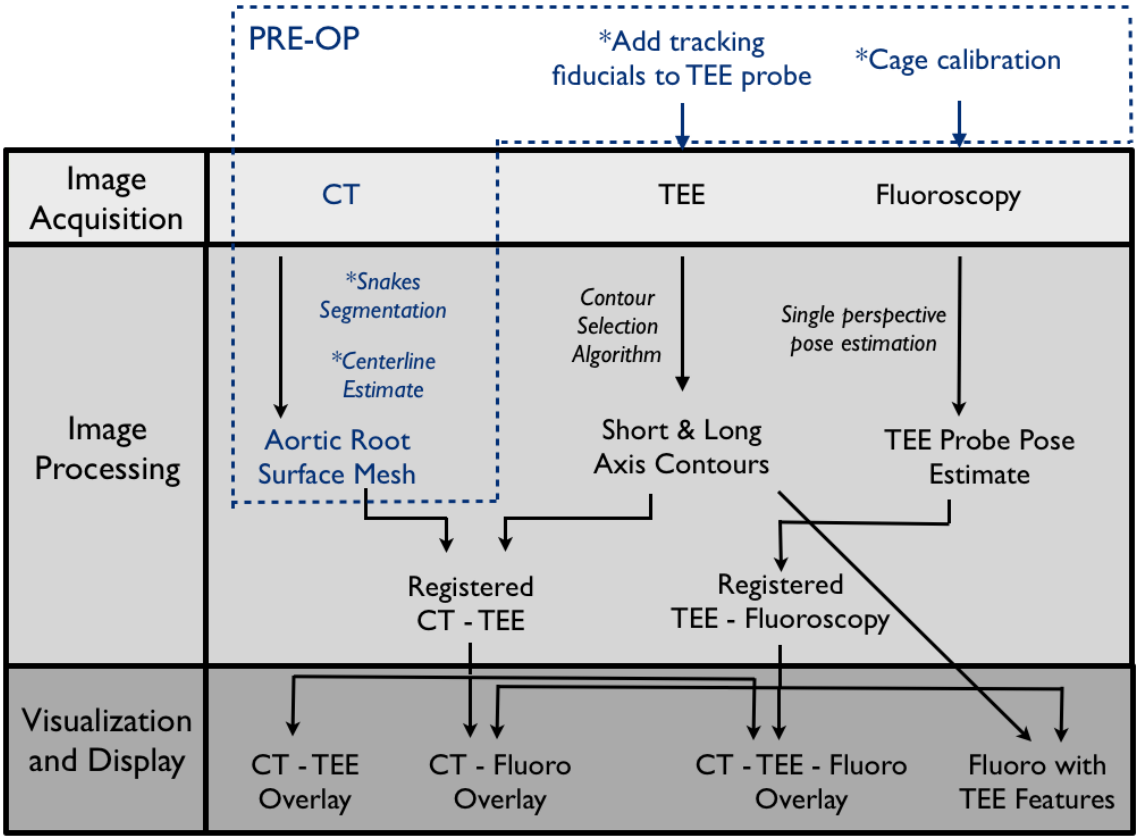

Fig. 7.2: Summary of the image processing workflow in the proposed image-guidance system. Steps denoted with a * require some user interaction. Steps shown in blue correspond to processing that occurs pre-operatively, and that can be carried out hours to days ahead of the clinical procedure.

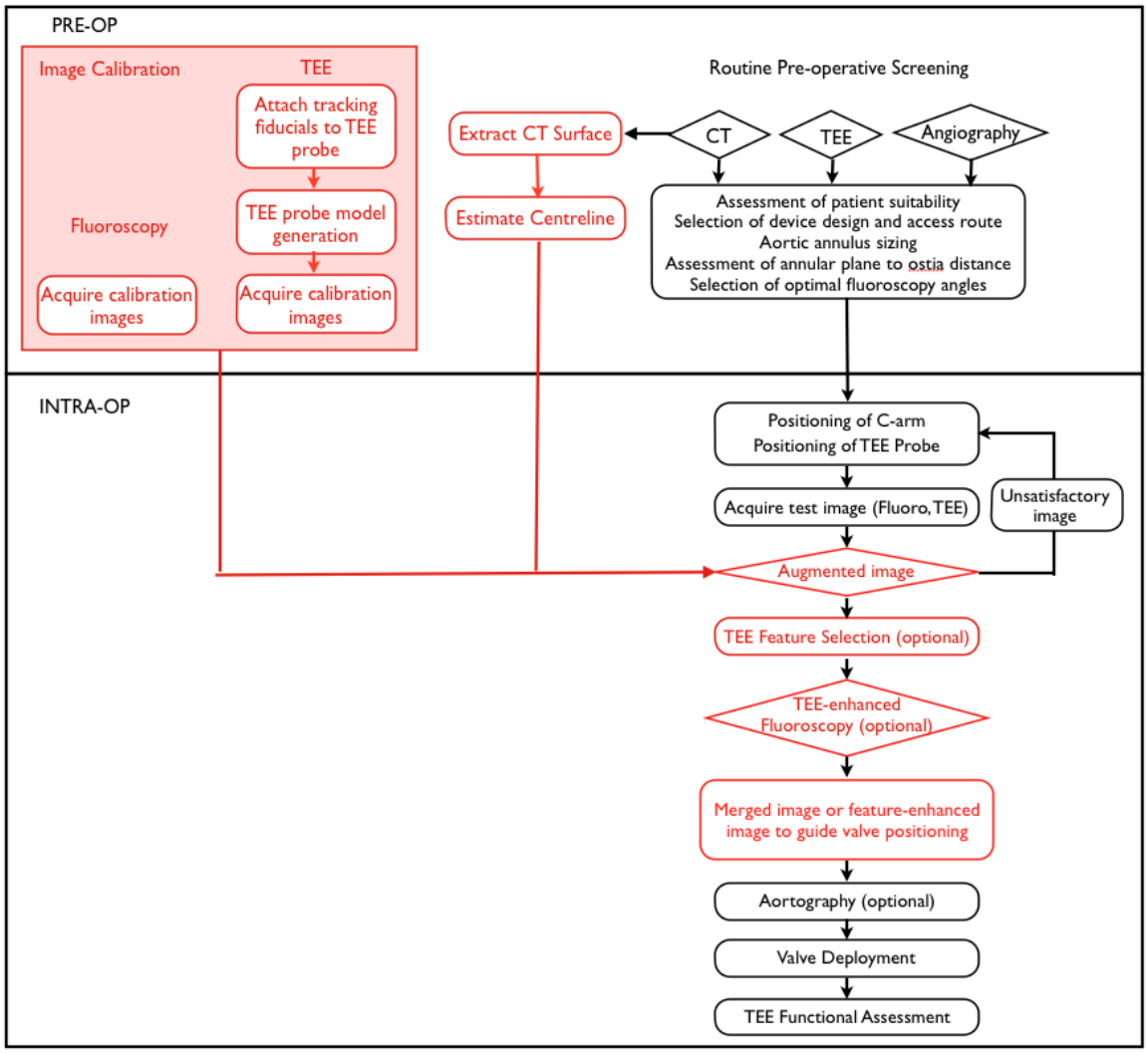

Fig. 7.3: Summary of the clinical workflow in the proposed image-guidance system. Steps shown in red are modifications to the standard clinical TAVI workflow. A similar image showing the workflow required for only TEE-fluoroscopy registration was shown in Figure 4.21 in Chapter 4.

7.3 Affordability and accessibility

A major advantage to the proposed augmented image-guidance system is that it does not introduce any additional hardware to the operating room. Other attempts at providing improved image-guidance require the addition of intra-operative

3D imaging, such as intra-operative CT or MRI [4, 5, 6]. These systems require significant infrastructure investments and operating expenses, and may require OR layouts specifically designed to accommodate this equipment. In contrast, the proposed system uses existing clinical images, and requires only a desktop computer for the image processing software. The cost of the TEE tracking attachment is trivial ($<$ 50 USD). If approved for clinical use, low cost and lack of specialized hardware would allow this technology immediate implementation in all cardiac centres that perform TAVI procedures.

7.4 Future Work

7.4.1 Improvements to Registration Accuracy and Robustness

As discussed in Section 6.3.3.3, there remains room for improvement in the accuracy of CT-TEE registration. The simulation studies in Section 5.2 demonstrate that the use of XPlane images is inherently limited in accuracy due to the lack of adequate constraining geometry in the aortic root anatomy. A potential way to improve accuracy is to combine the information using multiple tracked XPlane images, although this may introduce some tracking and aortic root motion error. The introduction of temporal constraints (discussed in Section 6.3.3.3) or patient-specific aortic root models [7] may also be computationally inexpensive methods of improving accuracy. Finally, a surface-based method may be combined with image intensity-based methods [8], although this may be more demanding computationally.

In this thesis, relatively simple energy functionals were used in the automatic contour selection process. These energy functionals were chosen because they were computationally inexpensive yet relatively robust. More sophisticated energy functionals could potentially improve contour selection accuracy. In addition, providing a standardized protocol for the echocardiographer acquiring the TEE images to increase consistency in the gain and scale settings may allow for better parameter optimization. Since these images are used for intra-operative guidance alone and not for diagnostic

purposes, such changes are easily implemented and have no potential to adversely impact patient care.

7.4.2 Clinical Testing

The next stage in the development of this technology is clinical testing. In this thesis all of the development and testing occurred in a laboratory setting. Implementation of a clinical prototype is required to allow intra-operative use, testing, and refinement. While laboratory testing allows the measurement of performance metrics such as accuracy, precision and robustness, clinical trials are required to determine if the use of this image-guidance system has any impact on patient outcomes:

1. Do physicians modify their choice of stent placement based on viewing the augmented images?
2. Does the use of augmented image-guidance reduce intra-operative and post-operative complications?
3. Does the use of augmented image-guidance reduce morbidity?
4. Is this technology most useful in certain patient populations (for example, patients at risk of acute kidney injury from radio-opaque contrast agents?)

7.4.3 Related Areas of Research

7.4.3.1 Calcium Fracture Patterns

The pattern of calcium fracture on the highly calcified native valve during TAVI is poorly understand and a current area of research [9]. Better understanding of fracture patterns would enable physicians to better select optimal deployment positions. Furthermore, the ability to image the calcium during the procedure would allow real-time modifications of position to prevent coronary occlusions and paravalvular leak.

7.4.3.2 Uncertainty Visualization

Augmented images may aid surgeons in determining the location of relevant anatomical structures, such as the basal root plane or the coronary ostia. However,

merged or feature-enhanced images may be misleading to physicians as the error in the measurement of these locations are not inherently obvious in the visualization interfaces discussed. The incorporation of some form of uncertainty visualization into the user interface may lead to improved results. A need for the development of intuitive and useful display of uncertainty information in surgical navigation exists [10].

7.4.4 Other Applications

While the methods developed in this thesis were designed specifically for the TAVI procedure, they have many other potential applications in the guidance of minimally invasive cardiac procedures. A real-time TEE-fluoroscopy or CT-fluoroscopy registration can be used in the guidance of cardiac ablations, minimally invasive atrial septal defect repair and mitral valve repairs. Several attempts at using statically registered images exist [11, 12, 13], but there remains a need for real-time update and display.

Recently, there has been significant growth of interest in the development of minimally invasive off-pump beating heart cardiac interventions. Since there is no direct visualization of the targets, these procedures rely heavily on intra-operative image guidance. The use of augmented image-guidance may allow the development of new surgical techniques and procedures.

References

[1] Linte CA, White J, Eagleson R, Guiraudon GM, Peters TM. Virtual and augmented medical imaging environments: Enabling technology for minimally invasive cardiac interventional guidance. IEEE Reviews in Biomedical Engineering. 2010;3:25–47.

[2] Lo J, Moore J, Wedlake C, Guiraudon G, Eagleson R, Peters T. Surgeon-controlled visualization techniques for virtual reality-guided cardiac surgery. In: Westwood J, Westwood S, Haluck R, Hoffman H, Mogel G, Phillips R, et al., editors. Medicine Meets Virtual Reality 17. IOS Press; 2009. p. 162–167.

[3] Hanna G, Shimi S, Cuschieri A. Task performance in endoscopic surgery is influenced by location of the image display. Ann Surg. 1998;227(4):481–484.

[4] Horvath KA, Mazilu D, Guttman M, Zetts A, Hunt T, Li M. Midterm results of transapical aortic valve replacement via real-time magnetic resonance imaging guidance. Journal of Thoracic and Cardiovascular Surgery. 2010;139(2):424–430.

[5] Kahlert P, Parohl N, Albert J, Schafer L, Reinhardt R, Kaiser GM, et al. Real-time magnetic resonance imaging-guided transarterial aortic valve implantation: In vivo evaluation in swine. Journal of the American College of Cardiology. 2012;59(2):192–193.

[6] Kempfert J, Falk V, Schuler G, Linke A, Merk D, Mohr FW, et al. Dyna-CT During Minimally Invasive Off-Pump Transapical Aortic Valve Implantation. The Annals of Thoracic Surgery. 2009;88(6):2041.

[7] Ionasec RI, Voigt I, Georgescu B, Wang Y, Houle H, Vega-Higuera F, et al. Patient-specific modeling and quantification of the aortic and mitral valves from 4-D cardiac CT and TEE. IEEE Transactions on Medical Imaging. 2010;29(9):1636–1651.

[8] Li F, Lang P, Rajchl M, Chen ECS, Guiraudon G, Peters TM. Towards real-time

3D US-CT registration on the beating heart for guidance of minimally invasive cardiac interventions. vol. 8316. SPIE; 2012. p. 831615.

[9] Bombien R, Humme T, Schunke M, Lutter G. Percutaneous aortic valve replacement: computed tomography scan after valved stent implantation in human cadaver hearts. European Journal of Cardio-thoracic Surgery. 2009;36:592–594.

[10] Simpson A. The Computation and Visualization of Uncertainty in Surgical Navigation. Queens University; 2010.

[11] Auricchio A, Sorgente A, Soubelet E, Regoli F, Spinucci G, Vaillant R, et al. Accuracy and usefulness of fusion imaging between three-dimensional coronary sinus and coronary veins computed tomographic images with projection images obtained using fluoroscopy. Europace. 2009;11(11):1483–1490.

[12] Knecht S, Skali H, O'Neill MD, Wright M, Matsuo S, Chaudhry GM, et al. Computed tomography-fluoroscopy overlay evaluation during catheter ablation of left atrial arrhythmia. Europace. 2008;10(8):931–938.

[13] Ector J, De Buck S, Huybrechts W, Nuyens D, Dymarkowski S, Bogaert J, et al. Biplane three-dimensional augmented fluoroscopy as single navigation tool for ablation of atrial fibrillation: Accuracy and clinical value. Heart Rhythm. 2008;5(7):957–964.

Appendix A

Fiducial-Based Tracking

The pose estimation implementation used was created by Petar Seslija, and further details are provided in [1].

A.1 Projection-Procrustes Registration

The image coordinates, (u_i, v_i) of a marker projection upon the image plane are related to the 3D position of the marker, $P_i(x_i, y_i, z_i)$ by the following relationship:

$$u_i = x_i * D/z_i \tag{A.1}$$

$$v_i = y_i * D/z_i \tag{A.2}$$

where D is the focal length of the radiography system.

Measurements of the coordinates u_i and v_i contains errors from image noise and geometric distortion.

The position of each tracking fiducial within the object coordinate system P_i' is related to the world coordinate system P_i by the transformation:

$$P_i = [R]^T P_i' + t \tag{A.3}$$

where $[R]$ is the rotation matrix and t is the translation. Due to measurement errors, an exact solution cannot be found, and the solution is optimized by minimizing the perpendicular distance between each marker and its projection line:

$$d_i = |P_i - Pr_i| \tag{A.4}$$

where Pr_i is the projection of the rigid body points P_i onto its projection line.

A.2 Fiducial Location Measurement

A.2.1 Fluoroscopy Image

Fiducial detection is accomplished using the following algorithm. An initial estimate of TEE probe height is used, and was determined empirically by OR table height over the C-arm source.

1. A search window of s x s pixels is defined, where s is 5 times the expected diameter of the fiducial.
2. The search window is convolved with an inverted Laplacian of a Gaussian (LoG) convolution kernal to perform edge enhancement and image smoothing.
3. The search window is binarized using a threshold calculated using the following equation:

   $$thresh = gl_{min} + \gamma(gl_{max} - gl_{min}) \tag{A.5}$$

   where gl_{max} and gl_{min} are the maximum and minimum gray levels in the search window, and γ is set empirically.
4. Foreground pixels are grouped using connected components labelling
5. The intensity-weighted centroid of each component is calculated
6. Area and shape criteria (eccentricity) are applied using empirically selected thresholds.
7. Remaining components are scored according to probability of being the actual marker projection, where the total rank of each component is calculated as a

sum of:

- Distance from the predicted location (component closes to predicted location receives highest rank)
- Mean intensity similarity
- Area similarity

References

[1] Seslija P. Dynamic Measurement of Three-Dimensional Motion from Single-Perspective Two-Dimensional Radiographic Projections. University of Western Ontario; 2009.

Appendix B

Intensity-Based Tracking Patterns

B.1 Hypothesis

Compared to the native TEE probe geometry, custom-designed 3D patterns of a similar size can provide greater pose estimation precision in the out-of-plane rotations and translation directions, without change in the precision of the in-plane translation and rotations.

B.2 Methods and Materials

Autocorrelation graphs were generated to assess the performance of custom-designed tracking attachment patterns using the methodology presented in Section 3.2.

3D models were generated using Solidworks^{TM}CAD software (Dassault Systèmes Solidworks Corp). The surface models were converted into representative CT volumes by assigning a constant attenuation coefficient to the voxels inside the volume. The size of the 3D models were constrained to fit inside the TEE probe casing. Two empirically designed patterns were evaluated with both ideal and noisy (2.5% gaussian) images. These patterns were selected to maximize information provided by edges and intensity differences when rotated and translated in the out-of-plane directions:

1. **Hatch pattern (Figure B.1a)** - flat stripes (0.45mm x 8.6mm x 0.151 mm)

arranged in two layers offset by 90°

2. **Concentric squares (Figure B.1b)** - dimensions as shown in Figure B.1b.

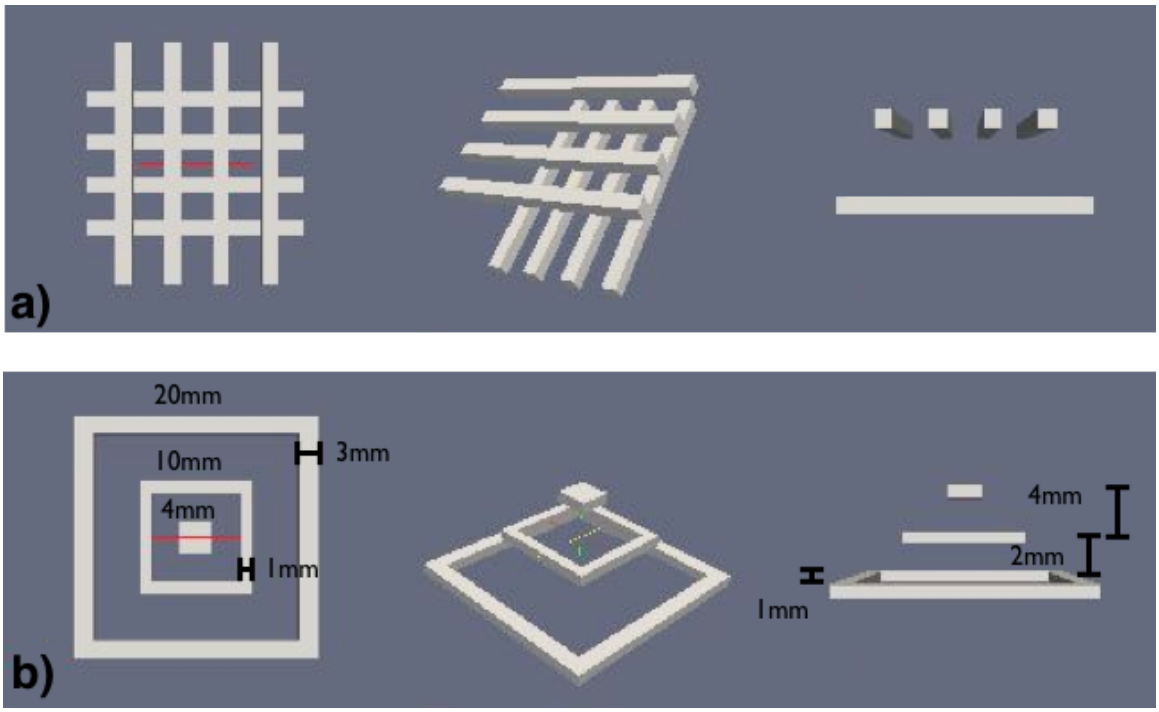

Fig. B.1: Tracking patterns tested. (a) Hatch pattern. (b) Concentric squares.

B.3 Results

Autocorrelation graphs for the hatch pattern and concentric ring pattern are shown in Figures B.2 and B.3 respectively. Under ideal circumstances, significantly narrower peaks can be achieved in the out-of-plane rotational directions with the use of multiple straight lines that reinforce each other. However, these peaks are widened with the addition of noise (Figures B.2 d-e, B.3d-e). The repetitive nature of these patterns also contribute to local maxima which may cause incorrect convergence of the algorithm if initialization is not adequately close (Figures B.2 a-d, Figure B.3 a-b).

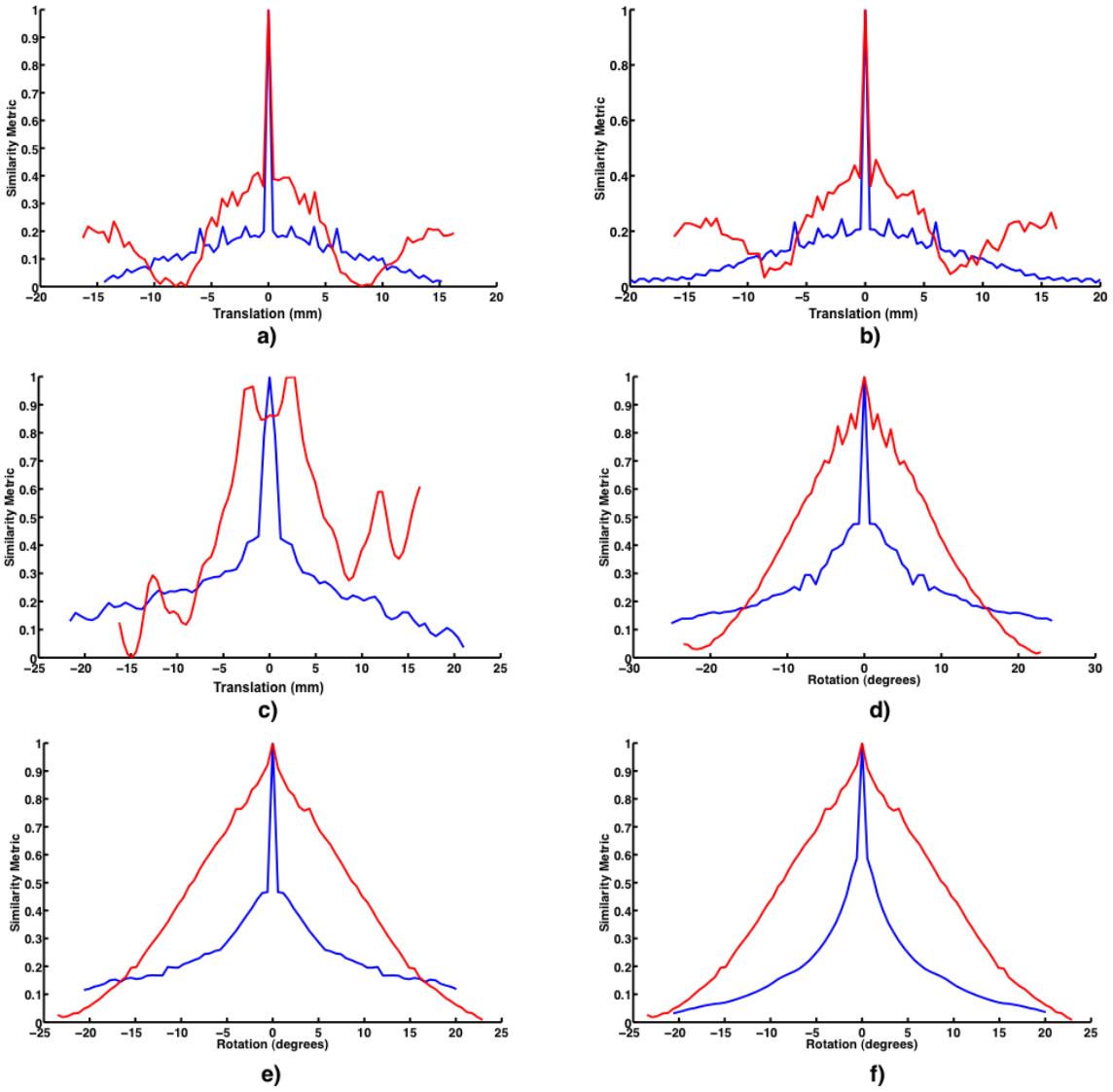

Fig. B.2: Autocorrelation graphs for the hatch pattern. (a) X Translation. (b) Y Translation (c) Z Translation. (d) X Rotation. (e) Y Rotation. (f) Z Rotation.

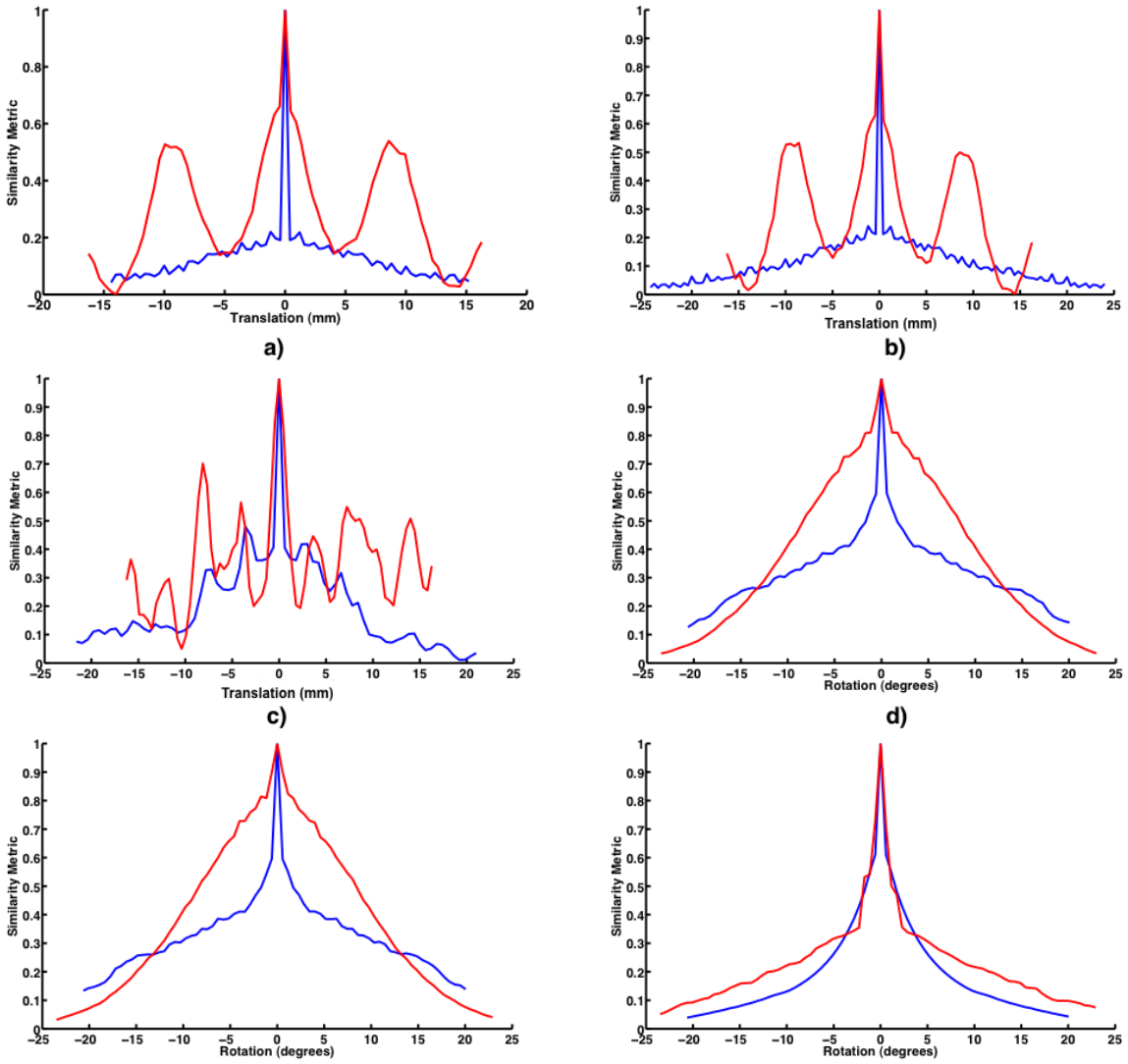

Fig. B.3: Autocorrelation graphs for the concentric ring pattern. (a) X Translation. (b) Y Translation (c) Z Translation. (d) X Rotation. (e) Y Rotation. (f) Z Rotation.

B.4 Discussion and Conclusions

The design and testing of further patterns was not pursued in this thesis, since fiducial-based pose estimation was selected as a more appropriate form of TEE tracking for the TAVI application. However, this initial study suggests that tool tracking using other geometrical patterns may be possible for other applications. Further work

is required to develop optimal geometric designs, particularly those on cylindrical or irregular surfaces. Patterns may be optimized preferentially for translations or rotations in specific directions depending on the tool type and usage. Development of an easy, onsite manufacturing process to affix these patterns to surgical tools is also required. Finally, these theoretical studies need to be followed up with empirical accuracy studies.

Appendix C

Fiducial Locations

Fiducial locations are described relative to the the centre of mass of the group of 7 fiducials.

Table C.1: Fiducial Locations for the tracking experiments described in Chapter 3.

	X (mm)	Y (mm)	Z (mm)
Marker 1	14.16	-24.4224	-18.3779
Marker 2	14.3	-23.8064	21.7851
Marker 3	8.772	31.2826	-18.9939
Marker 4	8.772	32.0516	21.6321
Marker 5	-8.463	-22.2694	-10.8379
Marker 6	-9.079	-21.6554	6.7051
Marker 7	-28.47	28.8196	-1.9129

Table C.2: Fiducial Locations for the phantom and *ex vivo* experiments described Chapter 4.

	X (mm)	Y (mm)	Z (mm)
Marker 1	-0.48	1.82	-15.69
Marker 2	-9.25	0.74	-8.15
Marker 3	7.67	2.44	-7.54
Marker 4	-0.94	-3.71	-7.23
Marker 5	-8.02	-3.86	7.69
Marker 6	6.28	6.13	8.77
Marker 7	-4.74	-3.56	22.15

Table C.3: Fiducial Locations for the *in vivo* experiments described Chapter 4.

	X (mm)	Y (mm)	Z (mm)
Marker 1	8.926285714	-7.551	5.797571429
Marker 2	-7.529714286	-10.8	-5.587428571
Marker 3	7.373285714	1.215	5.486571429
Marker 4	-5.840714286	0.286	7.216571429
Marker 5	-0.893714286	-1.54	-8.312428571
Marker 6	-7.758714286	9.611	5.227571429
Marker 7	5.723285714	8.779	-9.828428571

Appendix D

Relative Tracking Accuracy Protocol

X Translation	
Measurement Number	Relative Displacement(in)
1	0.25
2	0.25
3	0.25
4	0.25
5	0.25
6	0.25
7	0.25
8	0.25
9	0.25
10	0.25
11	0.25
12	0.25
13	0.5
14	0.5
15	0.5
16	0.5
17	0.5
18	0.5
19	1
20	1
21	1
22	1
23	1
24	1

Y Translation	
Measurement Number	Relative Displacement(in)
1	0.25
2	0.25
3	0.25
4	0.25
5	0.25
6	0.25
7	0.25
8	0.25
9	0.25
10	0.25
11	0.25
12	0.25
13	0.5
14	0.5
15	0.5
16	0.5
17	0.5
18	0.5
19	1
20	1
21	1
22	1
23	1
24	1

Z Translation	
Measurement Number	Relative Displacement(in)
1	0.5
2	0.5
3	0.5
4	0.5
5	0.5
6	0.5
7	1
8	1
9	1
10	1
11	1
12	2
13	2
14	2
15	2

X Rotation	
Measurement Number	Relative Displacement(°)
1	2
2	2
3	2
4	2
5	3
6	4
7	5
8	5
9	5
10	10
11	10

Y Rotation	
Measurement Number	Relative Displacement(°)
1	1
2	1
3	1
4	2
5	2
6	2
7	2
8	2
9	2
10	5
11	5
12	5
13	10
14	10
15	45

Z Rotation	
Measurement Number	Relative Displacement(°)
1	1
2	1
3	1
4	1
5	1
6	1
7	2
8	2
9	4
10	4
11	5
12	10
13	10

Appendix E

Ethics Approvals

For the chapters in this thesis that included experimental work using animal or human images, ethics approval was sought from the Board of Ethics at Western University. Below is a copy of the ethics approvals.

Research Western

Use of Human Participants - Ethics Approval Notice

Principal Investigator: Dr. Terry Peters
Review Number: 18069E
Review Level: Delegated
Approved Local Adult Participants: 100
Approved Local Minor Participants: 0
Protocol Title: Image-Guidance in Cardiac Interventions
Department & Institution: Medical Biophysics, Robarts Research Institute
Sponsor: Canadian Institutes of Health Research

Ethics Approval Date: June 16, 2011 **Expiry Date:** May 31, 2016
Documents Reviewed & Approved & Documents Received for Information:

Document Name	Comments	Version Date
UWO Protocol		
Letter of Information & Consent		2011/04/25

This is to notify you that The University of Western Ontario Research Ethics Board for Health Sciences Research Involving Human Subjects (HSREB) which is organized and operates according to the Tri-Council Policy Statement: Ethical Conduct of Research Involving Humans and the Health Canada/ICH Good Clinical Practice Practices: Consolidated Guidelines; and the applicable laws and regulations of Ontario has reviewed and granted approval to the above referenced revision(s) or amendment(s) on the approval date noted above. The membership of this REB also complies with the membership requirements for REB's as defined in Division 5 of the Food and Drug Regulations.

The ethics approval for this study shall remain valid until the expiry date noted above assuming timely and acceptable responses to the HSREB's periodic requests for surveillance and monitoring information. If you require an updated approval notice prior to that time you must request it using the UWO Updated Approval Request Form.

Members of the HSREB who are named as investigators in research studies, or declare a conflict of interest, do not participate in discussion related to, nor vote on, such studies when they are presented to the HSREB.

The Chair of the HSREB is Dr. Joseph Gilbert. The UWO HSREB is registered with the U.S. Department of Health & Human Services under the IRB registration number IRB 00000940.

S[redacted]

Ethics Officer to Contact for Further Information

Janice Sutherland	✓ Grace Kelly	Shantel Walcott
[redacted]	[redacted]	[redacted]

This is an official document. Please retain the original in your files.

Appendix F

Copyright Releases

For the chapters in this thesis that were adapted from published articles, permission was sought to reproduce them in this thesis. Below are a copy of the copyright agreements that explicitly allow for the creation of derivative works.

F.1 Releases for material in Chapter 3

SPRINGER LICENSE
TERMS AND CONDITIONS

May 20, 2012

This is a License Agreement between Pencilla Lang ("You") and Springer ("Springer") provided by Copyright Clearance Center ("CCC"). The license consists of your order details, the terms and conditions provided by Springer, and the payment terms and conditions.

All payments must be made in full to CCC. For payment instructions, please see information listed at the bottom of this form.

License Number	2913221491480
License date	May 20, 2012
Licensed content publisher	Springer
Licensed content publication	Springer eBook
Licensed content title	Three-Dimensional Ultrasound Probe Pose Estimation from Single-Perspective X-Rays for Image-Guided Interventions
Licensed content author	Pencilla Lang
Licensed content date	Sep 18, 2010
Type of Use	Thesis/Dissertation
Portion	Full text
Number of copies	1
Author of this Springer article	Yes and you are the sole author of the new work
Order reference number	
Title of your thesis / dissertation	Augmented Image-Guidance for Transcatheter Aortic Valve Implantation
Expected completion date	Aug 2012
Estimated size(pages)	200
Total	0.00 USD
Terms and Conditions	

Introduction
The publisher for this copyrighted material is Springer Science + Business Media. By clicking "accept" in connection with completing this licensing transaction, you agree that the following terms and conditions apply to this transaction (along with the Billing and Payment terms and conditions established by Copyright Clearance Center, Inc. ("CCC"), at the time that you opened your Rightslink account and that are available at any time at http://myaccount.copyright.com).

Limited License
With reference to your request to reprint in your thesis material on which Springer Science and Business Media control the copyright, permission is granted, free of charge, for the use indicated in your enquiry.

Licenses are for one-time use only with a maximum distribution equal to the number that you identified in the licensing process.

This License includes use in an electronic form, provided its password protected or on the university's intranet or repository, including UMI (according to the definition at the Sherpa website: http://www.sherpa.ac.uk/romeo/). For any other electronic use, please contact Springer at (permissions.dordrecht@springer.com or permissions.heidelberg@springer.com).

The material can only be used for the purpose of defending your thesis, and with a maximum of 100 extra copies in paper.

Although Springer holds copyright to the material and is entitled to negotiate on rights, this license is only valid, provided permission is also obtained from the (co) author (address is given with the article/chapter) and provided it concerns original material which does not carry references to other sources (if material in question appears with credit to another source, authorization from that source is required as well).

Permission free of charge on this occasion does not prejudice any rights we might have to charge for reproduction of our copyrighted material in the future.

Altering/Modifying Material: Not Permitted
You may not alter or modify the material in any manner. Abbreviations, additions, deletions and/or any other alterations shall be made only with prior written authorization of the author(s) and/or Springer Science + Business Media. (Please contact Springer at (permissions.dordrecht@springer.com or permissions.heidelberg@springer.com)

Reservation of Rights
Springer Science + Business Media reserves all rights not specifically granted in the combination of (i) the license details provided by you and accepted in the course of this licensing transaction, (ii) these terms and conditions and (iii) CCC's Billing and Payment terms and conditions.

Copyright Notice:Disclaimer
You must include the following copyright and permission notice in connection with any reproduction of the licensed material: "Springer and the original publisher /journal title, volume, year of publication, page, chapter/article title, name(s) of author(s), figure number(s), original copyright notice) is given to the publication in which the material was originally published, by adding; with kind permission from Springer Science and Business Media"

Warranties: None

Example 1: Springer Science + Business Media makes no representations or warranties with respect to the licensed material.

Example 2: Springer Science + Business Media makes no representations or warranties with respect to the licensed material and adopts on its own behalf the limitations and disclaimers established by CCC on its behalf in its Billing and Payment terms and conditions for this licensing transaction.

Indemnity
You hereby indemnify and agree to hold harmless Springer Science + Business Media and CCC, and their respective officers, directors, employees and agents, from and against any and

all claims arising out of your use of the licensed material other than as specifically authorized pursuant to this license.

No Transfer of License
This license is personal to you and may not be sublicensed, assigned, or transferred by you to any other person without Springer Science + Business Media's written permission.

No Amendment Except in Writing
This license may not be amended except in a writing signed by both parties (or, in the case of Springer Science + Business Media, by CCC on Springer Science + Business Media's behalf).

Objection to Contrary Terms
Springer Science + Business Media hereby objects to any terms contained in any purchase order, acknowledgment, check endorsement or other writing prepared by you, which terms are inconsistent with these terms and conditions or CCC's Billing and Payment terms and conditions. These terms and conditions, together with CCC's Billing and Payment terms and conditions (which are incorporated herein), comprise the entire agreement between you and Springer Science + Business Media (and CCC) concerning this licensing transaction. In the event of any conflict between your obligations established by these terms and conditions and those established by CCC's Billing and Payment terms and conditions, these terms and conditions shall control.

Jurisdiction
All disputes that may arise in connection with this present License, or the breach thereof, shall be settled exclusively by arbitration, to be held in The Netherlands, in accordance with Dutch law, and to be conducted under the Rules of the 'Netherlands Arbitrage Instituut' (Netherlands Institute of Arbitration).***OR:***

All disputes that may arise in connection with this present License, or the breach thereof, shall be settled exclusively by arbitration, to be held in the Federal Republic of Germany, in accordance with German law.

Other terms and conditions:

v1.3

If you would like to pay for this license now, please remit this license along with your payment made payable to "COPYRIGHT CLEARANCE CENTER" otherwise you will be invoiced within 48 hours of the license date. Payment should be in the form of a check or money order referencing your account number and this invoice number RLNK500782908.
Once you receive your invoice for this order, you may pay your invoice by credit card. Please follow instructions provided at that time.

Make Payment To:
Copyright Clearance Center
[redacted]

For suggestions or comments regarding this order, contact RightsLink Customer Support: [redacted]ll free in the US) or [redacted]

Gratis licenses (referencing $0 in the Total field) are free. Please retain this printable

F.2 Releases for material in Chapter 4

IEEE COPYRIGHT AND CONSENT FORM

To ensure uniformity of treatment among all contributors, other forms may not be substituted for this form, nor may any wording of the form be changed. This form is intended for original material submitted to the IEEE and must accompany any such material in order to be published by the IEEE.Please read the form carefully and keep a copy for your files.

TITLE OF PAPER/ARTICLE/REPORT, INCLUDING ALL CONTENT IN ANY FORM, FORMAT, OR MEDIA (hereinafter, "The Work"):**US-Fluoroscopy Registration for Transcatheter Aortic Valve Implantation**

COMPLETE LIST OF AUTHORS:**Lang, Pencilla; Seslija, Petar; Chu, Michael; Bainbridge, Daniel; Guiraudon, Gerard; Jones, Douglas; Peters, Terry**

IEEE PUBLICATION TITLE (Journal, Magazine, Conference, Book):**Transactions on Biomedical Engineering**

COPYRIGHT TRANSFER

1. The undersigned hereby assigns to The Institute of Electrical and Electronics Engineers,Incorporated (the "IEEE") all rights under copyright that may exist in and to: (a) the above Work,including any revised or expanded derivative works submitted to the IEEE by the undersigned based on the Work; and (b) any associated written or multimedia components or other enhancements accompanying the Work.

CONSENT AND RELEASE

2. In the event the undersigned makes a presentation based upon the Work at a conference hosted or sponsored in whole or in part by the IEEE, the undersigned, in consideration for his/her participation in the conference, hereby grants the IEEE the unlimited, worldwide, irrevocable permission to use, distribute, publish, license, exhibit, record, digitize, broadcast, reproduce and archive, in any format or medium, whether now known or hereafter developed: (a) his/her presentation and comments at the conference; (b) any written materials or multimedia files used in connection with his/her presentation; and (c) any recorded interviews of him/her (collectively, the "Presentation"). The permission granted includes the transcription and reproduction ofthe Presentation for inclusion in products sold or distributed by IEEE and live or recorded broadcast ofthe Presentation during or after the conference.

3. In connection with the permission granted in Section 2, the undersigned hereby grants IEEE the unlimited, worldwide, irrevocable right to use his/her name, picture, likeness, voice and biographical information as part of the advertisement, distribution and sale ofproducts incorporating the Work or Presentation, and releases IEEE from any claim based on right of privacy or publicity.

4. The undersigned hereby warrants that the Work and Presentation (collectively, the "Materials") are original and that he/she is the author of the Materials. To the extent the Materials incorporate text passages, figures, data or other material from the works of others, the undersigned has obtained any necessary permissions. Where necessary, the undersigned has obtained all third party permissions and consents to grant the license above and has provided copies of such permissions and consents to IEEE.

[ ] Please check this box ifyou do not wish to have video/audio recordings made ofyour conference presentation.

See below for Retained Rights/Terms and Conditions, and Author Responsibilities.

AUTHOR RESPONSIBILITIES

The IEEE distributes its technical publications throughout the world and wants to ensure that the material submitted to its publications is properly available to the readership of those publications. Authors must ensure that their Work meets the requirements as stated in section 8.2.1 of the IEEE

PSPB Operations Manual, including provisions covering originality, authorship, author responsibilities and author misconduct. More information on IEEEs publishing policies may be found at http://www.ieee.org/publications_standards/publications/rights/pub_tools_policies.html. Authors are advised especially of IEEE PSPB Operations Manual section 8.2.1.B12: "It is the responsibility of the authors, not the IEEE, to determine whether disclosure of their material requires the prior consent of other parties and, if so, to obtain it." Authors are also advised of IEEE PSPB Operations Manual section 8.1.1B: "Statements and opinions given in work published by the IEEE are the expression of the authors."

RETAINED RIGHTS/TERMS AND CONDITIONS

General

1. Authors/employers retain all proprietary rights in any process, procedure, or article of manufacture described in the Work.

2. Authors/employers may reproduce or authorize others to reproduce the Work, material extracted verbatim from the Work, or derivative works for the author's personal use or for company use, provided that the source and the IEEE copyright notice are indicated, the copies are not used in any way that implies IEEE endorsement of a product or service of any employer, and the copies themselves are not offered for sale.

3. In the case of a Work performed under a U.S. Government contract or grant, the IEEE recognizes that the U.S. Government has royalty-free permission to reproduce all or portions of the Work, and to authorize others to do so, for official U.S. Government purposes only, if the contract/grant so requires.

4. Although authors are permitted to re-use all or portions of the Work in other works, this does not include granting third-party requests for reprinting, republishing, or other types of re-use.The IEEE Intellectual Property Rights office must handle all such third-party requests.

5. Authors whose work was performed under a grant from a government funding agency are free to fulfill any deposit mandates from that funding agency.

Author Online Use

6. Personal Servers. Authors and/or their employers shall have the right to post the accepted version of IEEE-copyrighted articles on their own personal servers or the servers of their institutions or employers without permission from IEEE, provided that the posted version includes a prominently displayed IEEE copyright notice and, when published, a full citation to the original IEEE publication, including a link to the article abstract in IEEE Xplore.Authors shall not post the final, published versions of their papers.

7. Classroom or Internal Training Use. An author is expressly permitted to post any portion of the accepted version of his/her own IEEE-copyrighted articles on the authors personal web site or the servers of the authors institution or company in connection with the authors teaching, training, or work responsibilities, provided that the appropriate copyright, credit, and reuse notices appear prominently with the posted material. Examples of permitted uses are lecture materials, course packs, e-reserves, conference presentations, or in-house training courses.

8. Electronic Preprints. Before submitting an article to an IEEE publication, authors frequently post their manuscripts to their own web site, their employers site, or to another server that invites constructive comment from colleagues.Upon submission of an article to IEEE, an author is required to transfer copyright in the article to IEEE, and the author must update any previously posted version of the article with a prominently displayed IEEE copyright notice. Upon publication of an article by the IEEE, the author must replace any previously posted electronic versions of the article with either (1) the full citation to the IEEE work with a Digital Object Identifier (DOI) or link to the article abstract in IEEE Xplore, or (2) the accepted version only (not the IEEE-published version), including the IEEE copyright notice and full citation, with a link to the final, published article in IEEE Xplore.

INFORMATION FOR AUTHORS

IEEE Copyright Ownership

It is the formal policy of the IEEE to own the copyrights to all copyrightable material in its technical publications and to the individual contributions contained therein, in order to protect the interests of the IEEE, its authors and their employers, and, at the same time, to facilitate the appropriate re-use of this material by others.The IEEE distributes its technical publications throughout the world and does so by various means such as hard copy, microfiche, microfilm, and electronic media.It also abstracts and may translate its publications, and articles contained therein, for inclusion in various compendiums, collective works, databases and similar publications.

Author/Employer Rights

If you are employed and prepared the Work on a subject within the scope of your employment, the copyright in the Work belongs to your employer as a work-for-hire. In that case, the IEEE assumes that when you sign this Form, you are authorized to do so by your employer and that your employer has consented to the transfer of copyright, to the representation and warranty of publication rights, and to all other terms and conditions of this Form. If such authorization and consent has not been given to you, an authorized representative of your employer should sign this Form as the Author.

GENERAL TERMS

1. The undersigned represents that he/she has the power and authority to make and execute this form.
2. The undersigned agrees to identify and hold harmless the IEEE from any damage or expense that may arise in the event of a breach of any of the warranties set forth above.
3. In the event the above work is not accepted and published by the IEEE or is withdrawn by the author(s) before acceptance by the IEEE, the foregoing grant of rights shall become null and void and all materials embodying the Work submitted to the IEEE will be destroyed.
4. For jointly authored Works, all joint authors should sign, or one of the authors should sign as authorized agent for the others.

Pencilla Lang	**23-02-2012**
Author/Authorized Agent For Joint Authors	**Date(dd-mm-yy)**

THIS FORM MUST ACCOMPANY THE SUBMISSION OF THE AUTHOR'S MANUSCRIPT.
Questions about the submission of the form or manuscript must be sent to the publication's editor.Please direct all questions about IEEE copyright policy to:
IEEE Intellectual Property Rights Office, [redacted]

SPIE **TRANSFER OF COPYRIGHT TO SOCIETY OF PHOTO-OPTICAL INSTRUMENTATION ENGINEERS (SPIE)**

Title of Paper: Accuracy Assessment of Transesophageal Echocardiography Registration

SPIE Paper Number: (xxxx-xx) 7964-70

Author(s): P. Lang, P. Seslija, D. Bainbridge, G. Guiraudon, D. Jones, M. Chu, D. Holdsworth, T. Peters

This signed statement must be returned to SPIE prior to the scheduled publication of the Proceedings or Journal in which the Paper will be published. The intent of this Agreement is to protect the interests of both SPIE and authors/employers and to specify reasonable rights for both parties related to publication and reuse of the material.

The undersigned hereby assign(s) to Society of Photo-Optical Instrumentation Engineers (SPIE) copyright ownership in the above Paper, effective if and when the Paper is accepted for publication by SPIE and to the extent transferable under applicable national law. This assignment gives SPIE the right to register copyright to the Paper in its name as claimant and to publish the Paper in any print or electronic medium.

Authors, or their employers in the case of works made for hire, retain the following rights:

1. All proprietary rights other than copyright, including patent rights.
2. The right to make and distribute copies of the Paper for internal purposes.
3. The right to use the material for lecture or classroom purposes.
4. The right to prepare derivative publications based on the Paper, including books or book chapters, journal papers, and magazine articles, provided that publication of a derivative work occurs subsequent to the official date of publication by SPIE.
5. The right to post an author-prepared version or an official version (preferred version) of the published paper on an internal or external server controlled exclusively by the author/employer, provided that (a) such posting is noncommercial in nature and the paper is made available to users without charge; (b) a copyright notice and full citation appear with the paper, and (c) a link to SPIE's official online version of the abstract is provided using the DOI (Document Object Identifier) link.

   Citation format:
   Author(s), "Paper Title," Publication Title, Editors, Volume (Issue) Number, Article (or Page) Number, (Year).

   Copyright notice format:
   Copyright XXXX (year) Society of Photo-Optical Instrumentation Engineers. One print or electronic copy may be made for personal use only. Systematic reproduction and distribution, duplication of any material in this paper for a fee or for commercial purposes, or modification of the content of the paper are prohibited.

   DOI abstract link format:
   http://dx.doi.org/DOI# (*Note: The DOI can be found on the title page or online abstract page of any SPIE article.)*

If the work that forms the basis of this Paper was done under a contract with a governmental agency or other entity that retains certain rights, this Transfer of Copyright is subject to any rights that such governmental agency or other entity may have acquired.

By signing this Agreement, the authors warrant that (1) the Paper is original and has not previously been published elsewhere; (2) this work does not infringe on any copyright or other rights in any other work; (3) all necessary reproduction permissions, licenses, and clearances have been obtained; and (4) the authors own the copyright in the Paper, are authorized to transfer it, and have full power to enter into this Agreement with SPIE.

WHO SHOULD SIGN. This form must be signed by (1) at least one author who is not a U.S. Government employee and (2) the author's employer if the Paper was prepared within the scope of the author's employment or was commissioned by the employer. If not signed by all authors, the author(s) signing this Agreement represents that he/she is signing this Agreement as authorized agent for and on behalf of all the authors.

[redacted] PENCILLA LANG 02/11/2011

Author's signature | Print name | Date (mm/dd/yyyy)

Author's signature | Print name | Date (mm/dd/yyyy)

Authorized Employer signature | Print name | Title | Date (mm/dd/yyyy)

U.S. GOVERNMENT EMPLOYMENT CERTIFICATION

A work prepared by a U.S. Government employee as part of his or her official duties is not eligible for U.S. Copyright. If all authors were U.S. Government employees when this Paper was prepared, and the authors prepared this Paper as part of their official duties, at least one author should sign below. If at least one author was not a U.S. Government employee, the work is eligible for copyright and that author should sign the Transfer of Copyright form above.

Author's signature | Print name | Date

Director of Publications [redacted]

F.3 Releases for material in Chapter 5

SPIE

TRANSFER OF COPYRIGHT TO SOCIETY OF PHOTO-OPTICAL INSTRUMENTATION ENGINEERS (SPIE)

Title of Paper: Feature-based US to CT Registration of the Aortic Root

SPIE Paper Number: (xxxx-xx) 7964-51

Author(s): P. Lang, E. Chen, G. Guiraudon, D. Jones, D. Bainbridge, M. Chu, M. Drangova, N. Hata, A. Jain, T. Peters

This signed statement must be returned to SPIE prior to the scheduled publication of the Proceedings or Journal in which the Paper will be published. The intent of this Agreement is to protect the interests of both SPIE and authors/employers and to specify reasonable rights for both parties related to publication and reuse of the material.

The undersigned hereby assign(s) to Society of Photo-Optical Instrumentation Engineers (SPIE) copyright ownership in the above Paper, effective if and when the Paper is accepted for publication by SPIE and to the extent transferable under applicable national law. This assignment gives SPIE the right to register copyright to the Paper in its name as claimant and to publish the Paper in any print or electronic medium.

Authors, or their employers in the case of works made for hire, retain the following rights:

1. All proprietary rights other than copyright, including patent rights.
2. The right to make and distribute copies of the Paper for internal purposes.
3. The right to use the material for lecture or classroom purposes.
4. The right to prepare derivative publications based on the Paper, including books or book chapters, journal papers, and magazine articles, provided that publication of a derivative work occurs subsequent to the official date of publication by SPIE.
5. The right to post an author-prepared version or an official version (preferred version) of the published paper on an internal or external server controlled exclusively by the author/employer, provided that (a) such posting is noncommercial in nature and the paper is made available to users without charge; (b) a copyright notice and full citation appear with the paper, and (c) a link to SPIE's official online version of the abstract is provided using the DOI (Document Object Identifier) link.

   Citation format:
   Author(s), "Paper Title," Publication Title, Editors, Volume (Issue) Number, Article (or Page) Number, (Year).

   Copyright notice format:
   Copyright XXXX (year) Society of Photo-Optical Instrumentation Engineers. One print or electronic copy may be made for personal use only. Systematic reproduction and distribution, duplication of any material in this paper for a fee or for commercial purposes, or modification of the content of the paper are prohibited.

   DOI abstract link format:
   http://dx.doi.org/DOI# (*Note: The DOI can be found on the title page or online abstract page of any SPIE article.)*

If the work that forms the basis of this Paper was done under a contract with a governmental agency or other entity that retains certain rights, this Transfer of Copyright is subject to any rights that such governmental agency or other entity may have acquired.

By signing this Agreement, the authors warrant that (1) the Paper is original and has not previously been published elsewhere; (2) this work does not infringe on any copyright or other rights in any other work; (3) all necessary reproduction permissions, licenses, and clearances have been obtained; and (4) the authors own the copyright in the Paper, are authorized to transfer it, and have full power to enter into this Agreement with SPIE.

WHO SHOULD SIGN. This form must be signed by (1) at least one author who is not a U.S. Government employee and (2) the author's employer if the Paper was prepared within the scope of the author's employment or was commissioned by the employer. If not signed by all authors, the author(s) signing this Agreement represents that he/she is signing this Agreement as authorized agent for and on behalf of all the authors.

[redacted] PENCILLA LANG 02/11/2011

Author's signature | Print name | Date (mm/dd/yyyy)

Author's signature | Print name | Date (mm/dd/yyyy)

Authorized Employer signature | Print name | Title | Date (mm/dd/yyyy)

U.S. GOVERNMENT EMPLOYMENT CERTIFICATION

A work prepared by a U.S. Government employee as part of his or her official duties is not eligible for U.S. Copyright. If all authors were U.S. Government employees when this Paper was prepared, and the authors prepared this Paper as part of their official duties, at least one author should sign below. If at least one author was not a U.S. Government employee, the work is eligible for copyright and that author should sign the Transfer of Copyright form above.

Author's signature | Print name | Date

Director of Publications, SPIE, [redacted]

F.4 Releases for material in Chapter 6

SPIE **TRANSFER OF COPYRIGHT TO SOCIETY OF PHOTO-OPTICAL INSTRUMENTATION ENGINEERS (SPIE)**

Title of Paper: Feature Identification for Image-Guided Transcatheter Aortic Valve Implantation

SPIE Paper Number: (xxxx-xx) 8316-106 **Contact Author Email:** plang3@uwo.ca

Author(s): Pencilla Lang, Martin Rajchl, A. Jonathan McLeod, Michael W.A. Chu, Terry M. Peters

This signed statement must be returned to SPIE prior to the scheduled publication of the Proceedings or Journal in which the Paper will be published. The intent of this Agreement is to protect the interests of both SPIE and authors/employers and to specify reasonable rights for both parties related to publication and reuse of the material.

The undersigned hereby assign(s) to Society of Photo-Optical Instrumentation Engineers (SPIE) copyright ownership in the above Paper, effective if and when the Paper is accepted for publication by SPIE and to the extent transferable under applicable national law. This assignment gives SPIE the right to register copyright to the Paper in its name as claimant and to publish the Paper in any print or electronic medium.

Authors, or their employers in the case of works made for hire, retain the following rights:

1. All proprietary rights other than copyright, including patent rights.
2. The right to make and distribute copies of the Paper for internal purposes.
3. The right to use the material for lecture or classroom purposes.
4. The right to prepare derivative publications based on the Paper, including books or book chapters, journal papers, and magazine articles, provided that publication of a derivative work occurs subsequent to the official date of publication by SPIE.
5. The right to post an author-prepared version or an official version (preferred version) of the published paper on an internal or external server controlled exclusively by the author/employer, provided that (a) such posting is noncommercial in nature and the paper is made available to users without charge; (b) a copyright notice and full citation appear with the paper, and (c) a link to SPIE's official online version of the abstract is provided using the DOI (Document Object Identifier) link.

   Citation format:
   Author(s), "Paper Title," Publication Title, Editors, Volume (Issue) Number, Article (or Page) Number, (Year).

   Copyright notice format:
   Copyright XXXX (year) Society of Photo-Optical Instrumentation Engineers. One print or electronic copy may be made for personal use only. Systematic reproduction and distribution, duplication of any material in this paper for a fee or for commercial purposes, or modification of the content of the paper are prohibited.

   DOI abstract link format:
   http://dx.doi.org/DOI# *(Note: The DOI can be found on the title page or online abstract page of any SPIE article.)*

If the work that forms the basis of this Paper was done under a contract with a governmental agency or other entity that retains certain rights, this Transfer of Copyright is subject to any rights that such governmental agency or other entity may have acquired.

By signing this Agreement, the authors warrant that (1) the Paper is original and has not previously been published elsewhere; (2) this work does not infringe on any copyright or other rights in any other work; (3) all necessary reproduction permissions, licenses, and clearances have been obtained; and (4) the authors own the copyright in the Paper, are authorized to transfer it, and have full power to enter into this Agreement with SPIE.

WHO SHOULD SIGN. This form must be signed by (1) at least one author who is not a U.S. Government employee and (2) the author's employer if the Paper was prepared within the scope of the author's employment or was commissioned by the employer. If not signed by all authors, the author(s) signing this Agreement represents that he/she is signing this Agreement as authorized agent for and on behalf of all the authors.

[redacted]	PENCILLA LANG	02/03/2012
Author's signature	Print name	Date (mm/dd/yyyy)
Author's signature	Print name	Date (mm/dd/yyyy)
Authorized Employer signature	Print name Title	Date (mm/dd/yyyy)

U.S. GOVERNMENT EMPLOYMENT CERTIFICATION
A work prepared by a U.S. Government employee as part of his or her official duties is not eligible for U.S. Copyright. If all authors were U.S. Government employees when this Paper was prepared, and the authors prepared this Paper as part of their official duties, at least one author should sign below. If at least one author was not a U.S. Government employee, the work is eligible for copyright and that author should sign the Transfer of Copyright form above.

Author's signature	Print name	Date (mm/dd/yyyy)

Director of Publications, SPIE, P.O. Box 10, Bellingham, WA 98227-0010 USA
Phone: 360/676-3290 (Pacific Time) • Fax: 360/647-1445 • E-mail: authorhelp@spie.org • http://SPIE.org Revised 3 Feb 2012

Vita

Name:	Pencilla Lang
Place of Birth:	Kitchener, Ontario
Year of Birth:	1987
Post-secondary Education and Degrees:	B.Eng Western University 2008
Honours and Awards:	CIHR MD/PhD Scholarship, 2009- Dr. Jakob Michaltschenko Scholarhip, 2007 - Cum Laude Poster Award, SPIE Medical Imaging, 2012 Honourable Mention Poster Award, SPIE Medical Imaging, 2011 Overall Best Poster Award, ISMICS, 2011 First Place Poster Award, IMNO, 2011 First Place Oral Presentation, Western Research Forum, 2011 Poster Award, CITAC Meeting, 2010 Second Place Poster Award, IMNO, 2010 Rowntree Prize in Medical History, IMNO, 2008 Third Place, Best Student Paper, History of Medicine Days, 2008 PEO Gold Medal, UWO Engineering, 2008 Best Student Paper Nomination, CCECE, 2008 Best Departmental Article, UWO Medical Journal, 2008 Third Place Mechanical Engineering Design Days Competition, 2008 UWO President's Entrance Scholarship, 2004-2008 First Place, Communications, Canadian Engineering Competition, 2007 First Place, Communications, Ontario Engineering Competition, 2007 Second Place, Communications, Western Engineering Competition, 2007 Lynda Diane Shaw Memorial Award, 2007 NSERC Undergraduate Summer Research Scholarship, 2006 Dr. L. Stuart Lauchland Scholarship, 2006 Ontario Professional Engineers Scholarship, 2005 NSERC Undergraduate Summer Research Scholarship, 2005 Manning Foundation Young Innovator's Award, 2004 IEEE Oregon Award for Achievement in Engineering, 2004

Related Work Experience:

Teaching Assistant: Western University:
Introduction to Medical Imaging, MBP 4475/ MBP 9515/ BME 9515, 2009, 2010

Kinematics and Dynamics of Machines, MBE 3381
2009

Business for Engineers, Bus2299
2006, 2008, 2009, 2010

Journal Manuscripts:

Lang P, Chu MW, Bainbridge D, Guiraudon G, Jones DL, Peters TM. Surface-based CT-TEE Registration of the Aortic Root. Submitted.

Lang P, Rajchl M, McCleod AJ, Chu MWA, Peters TM. Automatic Contour Selection for CT-TEE Registration. Submitted.

Lang P Peters TM, Bainbridge D, Chu M. Real-Time Echocardiographic Augmented Fluoroscopic Imaging To Improve Transcatheter Aortic Valve Implantation Accuracy. Submitted.

Lang P, Peters TM, Kiaii B, Chu MWA. The critical role of imaging navigation and guidance in transcatheter aortic valve implantation. Journal of Thoracic and Cardiovascular Surgery. 2012;143(6):1241-3.

Lang P, Seslija P, Chu MWA, Bainbridge D, Guiraudon GM, Jones DL, et al. USFluoroscopy registration for transcatheter aortic valve implantation. Biomedical Engineering, IEEE Transactions on. 2012;59(5):1444-53.

Linte CA, **Lang P**, Rettmann ME, Cho DS, Holmes III DR, Robb RA, et al. Accuracy considerations in image-guided cardiac interventions: Experience and lessons learned. International Journal of Computer Assisted Radiology and Surgery. 2012;7(1):13-25.

Guiraudon GM, Jones DL, Bainbridge D, Linte C, Pace D, **Lang P**, et al. Augmented reality image guidance during off-pump mitral valve replacement through the guiraudon universal cardiac introducer. Innovations: Technology and Techniques in Cardiothoracic and Vascular Surgery. 2010;5(6):430-8.
Kedgley, AE, Takaki SE, **Lang P**, Dunning CE. The Effect of Cross-Sectional Stem

Shape on the Torsional Stability of Cemented Implant Components. Journal of Biomechanical Engineering. 2007;129(3):310-4

Conference Manuscripts:

Lang P, Chu MW, Bainbridge D, Chen ECS, Peters TM. CT-US Registration for Guidance of Transcatheter Aortic Valve Implantation. In: Proceedings of Augmented Environments and Computer Assisted Interventions 2011. Toronto, Canada. 2011;LNCS 7264:85-92.

Lang P, Rajchl M, McLeod AJ, Chu MW, Peters TM. Feature identification for image-guided transcatheter aortic valve implantation. In: Wong, KH Holmes DRIII, editors. Proceedings of SPIE, Medical Imaging 2012: Visualization, Image-Guided Procedures and Modeling, San Diego, California, USA. SPIE; 2012;8316(1): 83162X.

Li F, **Lang P**, Rajchl F, Chen ECS, Guiraudon G, Peters TM. Towards real-time 3D US-CT registration on the beating heart for guidance of minimally invasive cardiac interventions. In: Wong, KH Holmes DRIII, editors. Proceedings of SPIE, Medical Imaging 2012: Visualization, Image-Guided Procedures and Modeling, San Diego, California, USA. SPIE; 2012;8316(1): 831615.

McLeod AJ, Moore J, **Lang P**, Bainbridge D, Campbell G, Jones DL, Guiraudon GM, Peters TM. Evaluation of mitral valve replacement anchoring in a phantom. In: Wong, KH Holmes DRIII, editors. Proceedings of SPIE, Medical Imaging 2012: Visualization, Image-Guided Procedures and Modeling, San Diego, California, USA. SPIE; 2012;8316(1): 8316Q.

Lang P, Rajchl M, Li F, Peters TM. Towards model-enchanced real-time ultrasound guided cardiac interventions. Proceedings of the IEEE ICBMI. Dec. 2011; 89 - 92.

Lang P, Seslija P, Bainbridge D, Guiraudon GM, Jones DL, Chu MW, et al. Accuracy assessment of fluoroscopy-transesophageal echocardiography registration. In: Wong, KH Holmes DRIII, editors. Proceedings of SPIE, Medical Imaging 2011: Visualization, Image-Guided Procedures and Modeling, Lake Buena Vista, Florida, USA. SPIE; 2011; 7964:79641Y.

Lang P, Chen ECS, Guiraudon GM, Jones DL, Bainbridge D, Chu MW, et al. Feature-based US to CT registration of the aortic root. In: Wong, KH Holmes DRIII, editors. Proceedings of SPIE, Medical Imaging 2011: Visualization, Image-Guided Procedures and Modeling, Lake Buena Vista, Florida, USA. SPIE; 2011; 7964: 79641G.

Peters TM, Pace DF, **Lang P**, Guiraudon GM, Jones DL, Linte CA. Ultrasound image guidance of cardiac interventions. In: Dhooge J, Doyley MM, editors. Proceedings of SPIE, Medical Imaging 2011: Ultrasonic Imaging, Tomography and Therapy, Lake Buena Vista, Florida, USA. SPIE; 2011; 7968: 79680T.

Lang P, Seslija P, Habets DF, Chu MWA, Holdsworth DW, Peters TM. Three-dimensional ultrasound probe pose estimation from single-perspective x-rays for image-guided interventions. In: Liao H, Edwards E, Pan, X, Fan Y, Yang GZ, editors. Medical Imaging and Augmented Reality. 2010;6326 LNCS:344-52.

Lang P. Design and prototyping of a fiber optic tactile array. In: Proceedings of the Canadian Conference on Electrical and Computer Engineering 2008. 2008:373-376.

Other Conference Abstracts, Poster and Podium Presentations:

Lang P, Chen ECS, Chu MW, Bainbridge D, Jones DL, Guiraudon G, Peters TM. Integrated CT and Echocardiography for Intraoperative Transcatheter Aortic Valve Implantation. Presented at the American Society of Echocardiography Meeting. June 2011, Montreal, Canada.

Lang P, Chen ECS, Chu MW, Bainbridge D, Jones DL, Guiraudon G, Peters TM. Augmented Ultrasound Guidance for Transcatheter Aortic Valve Implantation. Presented at the Internationally Society for Minimally Invasive Cardiothoraic Surgery. June 2011,Washington USA, Canada.

Lang P, Chen ECS, Bainbridge D, Chu MW, Peters TM. US to CT Registration of the Aortic Root. Presented at the 6th Annual London Imaging Day. June 2011, London, Canada.

Lang P, Peters TM. Image-Guidance for Minimally Invasive Heart Valve Replacement. Presented at the Western Research Forum. Feb 2011, London, Canada.

Lang P, Chen ECS, Bainbridge D, Chu MW, Peters TM. US to CT Registration of the Aortic Root: A Human Validation Study. Presented at the Imaging Network of Ontario Meeting. Feb 2011, Toronto, Canada.

Lang P, Chen ECS, Bainbridge D, Chu MW, Peters TM. Registration of the Aortic Root. Presented Clinical Investigator Trainee Association of Canada Young Investigators Forum, September 2010. Clinic Invest Med. 2010;55(4S):9

Lang P, Seslija P, Habets D, Chu MW, Holdsworth DW, Peters TM. Three-dimensional US Probe Localization by Single Perspective Pose Estimation. Presented at the Annual Meeting of the Canadian Organization of Medical Physicists. June 2010, Ottawa, Canada.

Lang P, Chen ECS, Bainbridge D, Chu MW, Peters TM. Three-dimensional Tracking of Interventional Devices using Single - perspective Fluoroscopy for Image-Guided Interventions. Presented at the Imaging Network of Ontario Meeting. Feb 2010, Toronto, Canada.

Lang P, Moore J, Peters TM. Surgical Tool Design in Image-Guided Cardiovascular Surgery. Presented at the 4th Annual London Imaging Day. June 2009, London, Canada.